The University Of Sheffield.

Understanding the dynamics of the Indonesian Throughflow and its global significance, both today and in the Late Quaternary

Yiwei Zhang

A Thesis Submitted for the Degree of Doctor of Philosophy

The Department of Geography

University of Sheffield

November 2022

Acknowledgements

First and foremost I would like to thank my supervisor, Prof. Grant Bigg, for his advice and guidance during the entire journey. I am grateful for his delicate contribution to this project, being always accessible and helpful, especially after I moved back to China in the final year. Without his support and help, it is impossible for me to get this point.

I want to thank my beloved parents most heartfeltly. you have been absolutely best, trusting and supporting my far travelled adventure without any hesitation. It was not easy for all of us that be separated during the entire epidemic, your love made this happen.

Last but not least, I would like to thank my housemate, Jennifer Ross, for being with me every step of this process, and her kind family, for welcoming me to their house when I cannot be with my family, and creating such a special overboard experience for me.

Abstract

This study investigates the Indonesian Throughflow (ITF), the current connects the Pacific and Indian Ocean via the Indonesian Seas, in both the modern and palaeo climate background. In the contemporary part, the interannual variability of the ITF and the behaviour of the local flows is studied. Using reanalysis dataset, the average ITF volume transport is 12.76 ± 2.74 Sv (106 m^3s^{-1}) during 1980 to 2016. The ITF hydrological characteristics support the current understanding of the main water source of the ITF is constructed by the colder and fresher water from the North Pacific and warm and saltier water from the South Pacific. The ENSO affects the ITF transport by the strength and distribution of monsoon on the seasonal scale. A shift of vertical structure of the ITF horizontal transport was found and located at the Banda Sea during the 1990s. The box model results indicate that the water source of the Banda Sea is essential for the stratification: the increased water supply from the South China Sea into the Banda sea would change the stratification of horizontal transport with a prolonged effect and the reanalysis data agrees. The palaeo research focuses long-term, geographically distant influences of the insolation variation and the ITF connection on the global meridional overturning circulation during the deglacial process since the Last Glacial Maximum (LGM). To achieve this, a numerical model, FRUGAL, simulated the natural, insolation varied and closed ITF scenario with LGM boundary. The results suggest that the varying insolation strengthened the polar-tropical temperature and salinity gradient, and caused the strengthening of the Southern Hemisphere Overturning at ~8 ka BP. The variation of the Southern Ocean and sensitive areas is consistent with the insolation variation. The closure of the ITF highly reduced the Atlantic Overturning and weakened the Agulhas Current; the Drake Passage presents a significant response to the closure of ITF; the seasonal variation weakened in Pacific Overturning but strengthened in Southern Hemisphere Overturning.

Contents

List of Tables

List of Figures

Declaration

I, the author, confirm that the Thesis is my own work. I am aware of the University's Guidance on the Use of Unfair Means (www.sheffield.ac.uk/ssid/unfair-means). This work has not previously been presented for an award at this, or any other, university.

Chapter 1 the Introduction

The Indonesian Throughflow (ITF) plays an essential role in the global thermohaline circulation (Gordon, 1986), also as known as the global meridional overturning circulation nowadays. As the major tropical connection between the Pacific and the Indian Ocean, the ITF not only transports heat and salinity (Hirst and Godfrey, 1993), but also helps to sustain and feed the North Atlantic Deep Water (Gordon, 1986; fig 1.1). In addition, the ITF shows a close relationship with El Niño-Southern Oscillation (ENSO) that has a global scale impact (Miyama et al., 1995; Meyers, 1996).

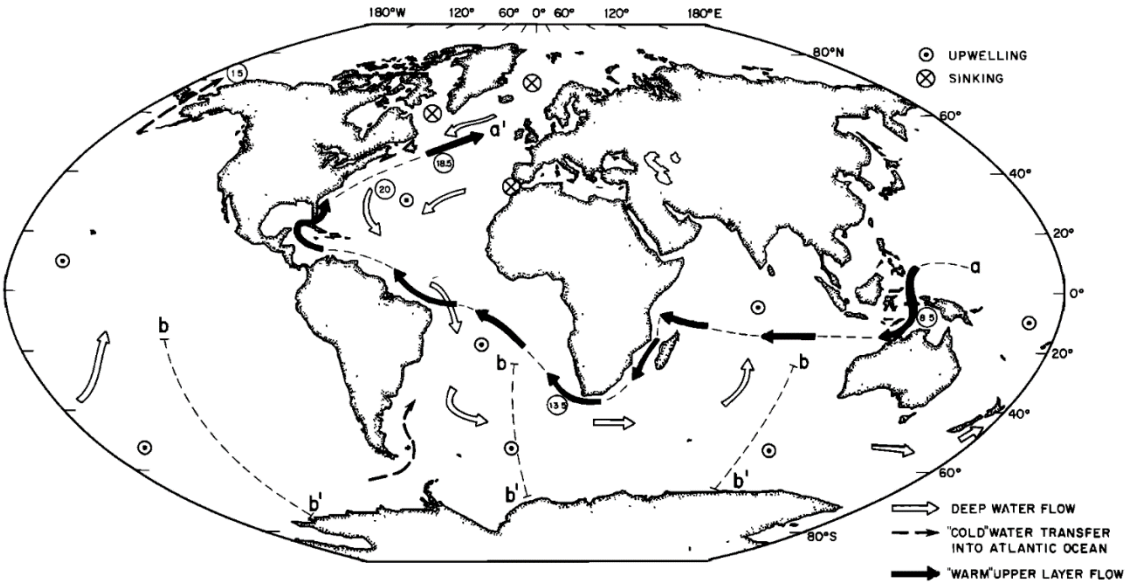

Figure 1.1 Global structure of the thermohaline circulation cell associated with NADW production (Gordon, 1986), the warm water route, shown by the solid arrows.

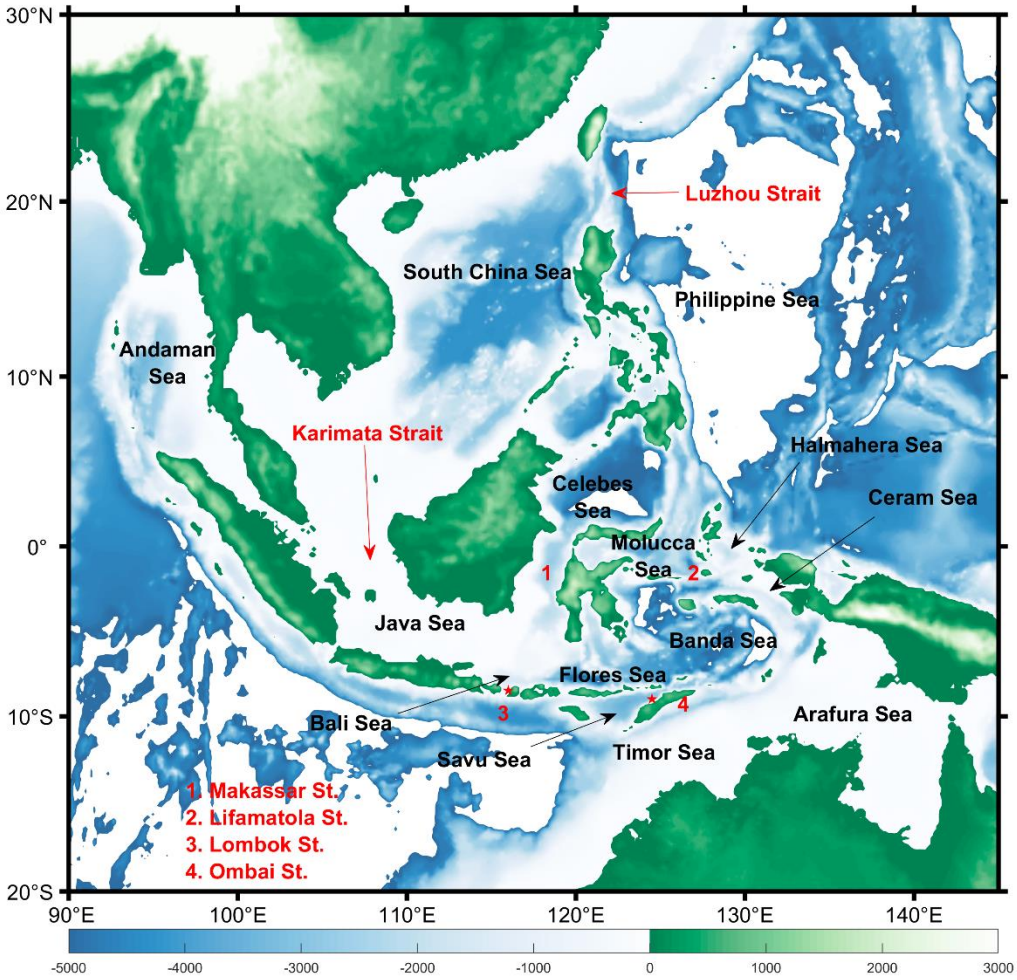

Figure 1.2 The topography in the ITF region, bathymetry and altitude are shown as contours (unit: metre). Data source: Terrain Base, Global 5 Arc-minute Ocean Depth and Land Elevation from the US National Geophysical Data Center (NGDC).

This research focuses on both the modern and palaeo-background. In the study of modern climate, the interannual variability of the ITF, the behaviour of the local flows, and the interannual relationship between the ITF and ENSO are investigated. To study the long-term teleconnection between the ITF and other ocean basins, at timescales beyond those possible from contemporary observations, the influence of the ITF on the global meridional overturning circulation is investigated in the palaeoclimate background. The main methodology is the numerical simulation for both sections, although including the study of

reanalysis datasets and mooring datasets. Combining with statistical analysis, the high temporal and spatial resolution modelling results and reanalysis datasets will be able to give a more comprehensive and detailed insight into the variation of the ITF and its influence on the global marine circulation than has been previously possible.

1.1 Indonesian Sea Region Geography and Climate Character

The Indonesian Sea, or seas, is usually considered an intersection sea area between the tropical Pacific Ocean and the tropical Indian Ocean; it is also called "the Indonesian Maritime Continent" (fig 1.2). This region is located in SE Asia, between 20ºS to 20ºN, 90º to 142ºE. As a semi-enclosed sea, the Indonesian Sea is geographically separated by the Indonesia Archipelago, Peninsular Malaysia and the Philippine Islands. In addition, it is composed of 14 subsidiary seas, including the Andaman Sea, the Arafura Sea, the Bali Sea, the Banda Sea, the Celebes Sea, the Ceram Sea, the Flores Sea, the Halmahera Sea, the Java Sea, the Molucca Sea, the Philippine Sea, the Savu Sea, the South China Sea and the Timor Sea. The Indonesian Sea has a typical tropical oceanic monsoon climate. Based on meteorological observation, the Indonesian Sea is controlled by the southeast wind during May to September and northwest wind during November to March (Murray and Arief, 1988). The annual variation of local weather and the monsoon is highly influenced by the ENSO states (Hamada et al., 2002). The wind field plays an important role in determining the ocean current state, which will be explained in the following section.

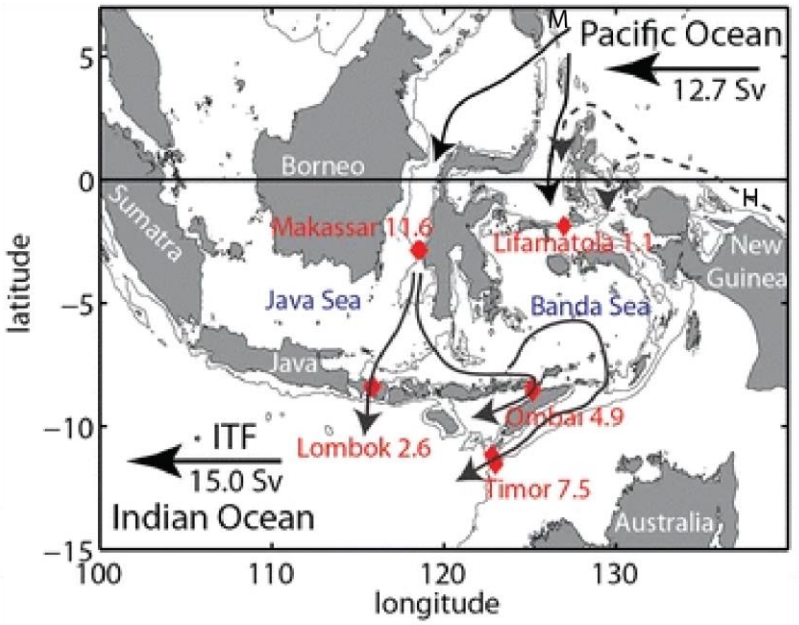

Figure 1.3 Transport of the currents contributing to the Indonesian Throughflow via different passages (Feng et. al., 2018). The additional flow contributing to the ITF beyond what is shown in the fig 1.3 derives from weak flows through the South China Sea and probably either side of New Guinea. M: Mindanao Retroflection, H: Halmahera Retroflection.

1.2 Indonesian Throughflow

The Indonesian Throughflow (ITF) is an ocean current within the Indonesian Sea (the black line arrow in fig 1.3). ITF transports warm, low-salinity water from the west tropical Pacific to the east tropical Indian Ocean, which leads to heat and freshwater transport. The Pacific feeds fresher and colder water from the North Pacific via the Mindanao Retroflection (M in fig 1.3), and saltier and warmer water from the South Pacific via the Halmahera Retroflection (H in fig 1.3). The Pacific water is modified by air-sea interaction, monsoon-driven vertical transport and enormously strong tidal movement in the Indonesian Seas. Thus, the ITF water is traceable in the Indian Ocean, and forms a low-salinity core across the entire Indian Ocean (Sprintall et al., 2014). The ITF is under the atmospheric deep convection

centre and the ascending branch of the Walker Circulation. Therefore, the ITF is highly involved in the tropical atmosphere-ocean interactions.

Based on observations, modelling and conjecture, the annual ITF transport has been estimated to vary from 0 to 30 Sv (1 Sv = 10^6 m^3s^{-1}) (table 1.1). The ITF transport has significant seasonal variation, being a maximum in boreal summer and minimum in winter (Miyama et al., 1995), and inter-annual variation (ENSO-related) also. The variation of ITF volume transport on different time scales will be discussed further in chapter 2. The heat transport via the ITF is significant. Based on the mooring data at the Makassar Strait, the annual heat transport via the upper 700m layer of the Makassar Strait is 0.55 petawatts (Vranes et al., 2002). Numerical simulation suggests this heat transport is possibly higher, reaching 0.63 petawatts for the whole ITF current, which is 1/3 of the total heat input to the equatorial Pacific area (Hirst and Godfrey, 1993). But it should be noticed that all the heat transport results depend on a 'reference temperature', which is the temperature used in temperature to energy conversion. This 'reference temperature' varies in different studies and is far lower than the endpoint, the Indian Ocean, water temperature. Therefore, although the heat transport via the ITF is very large, current results could be overestimated. Alongside interest in the ITF horizontal transport, the vertical structure of the ITF transport has attracted more attention recently. Modelling results show that the Banda Sea presents a clear three-layer structure, with each layer having different water sources (Liang et al., 2019). In this thesis, a similar result is found from the reanalysis dataset and a shift of this vertical structure is detected during 1990s for the very first time. More detail and a potential cause analysis are discussed in chapters 2 and 3.

Table 1.1 Estimates of Indonesian Throughflow Transport.

Reference	Transport (Sv)	Comment	Method
Wyrtki (1961)	1-3	In upper 200m layer	Dynamic height
Godfrey and Golding (1981)	10-20	In upper 400m layer	Sverdrup relation mass transport function
Piola and Gordon (1984)	14	At 33.6‰ salinity	Mass and freshwater balance
Wunsch et al. (1983)	negligible		Inverse in Pacific Ocean
Fine (1985)	5	In upper 300m layer	Tritium data
Fu (1986)	6.6	Minimum oxygen level is 1500m	Inverse in south Indian Ocean
Murry and Arief (1988)	10-15		Estimate from 1.7 in Lombok Strait observation
Godfrey (1989)	12		Sverdrup model output
Toole and Warren (1993)	6.7		With mean salinity of 34.5 psu and density of 1.023 g cm^{-3}
Hirst and Godfrey (1993)	17		GCM model
Molcard et al. (1994)	14 ± 6	In upper 500m layer	Estimate from 2.5 in Timor Passage
Miyama et al. (1995)	20 ± 3		Robust diagnostic model
Shriver and Hurlburt (1997)	15.1		Modelling result
Gordon et al.(1999)	9.3 ± 2.5		Moorings at the Makassar Strait during Dec 1996 to Jul 1998
Molcard et al. (2001)	11.2		Summing from Lombok Strait 1.7, Timor Passage 4.5 ± 1.5, Ombai Strait, 5 ± 1
Song et al. (2007)	11.7		GFDL coupled climate model
Sprintall et al (2009)	15		INSTANT mooring project during Jan 2004 to Nov 2006
Santoso et al. (2011)	21		CSIRO-GCM coupled model
Van Sebille et al. (2014)	14.3		Ocean model
Feng et al. (2018)	15		Estimate from IX1 XBT data

Gordon (1986) pointed out that as the only "warm water path" in the tropical region, the ITF is not only responsible for the Pacific and Indian Ocean heat exchange, but also plays

an essential role in sustaining and feeding North Atlantic Deep Water (NADW) and thermohaline circulation, or the meridional overturning circulation, at a global scale. As fig.1.1 and fig 1.4 show, the "warm water path" starts with the North Pacific Central Water, the thermocline in the Pacific, and then passes through the Indonesian Archipelago to the Indian Ocean. There, the Pacific water crosses the Indian Ocean in the 10-20˚S belt and after mixing with Indian Ocean water, goes south through the Mozambique Channel. Then that water separates into two main flows: the larger part is the Agulhas water, which enters the Agulhas Retroflection into the South Indian Ocean, and the rest flows into the Atlantic. At the western boundary of the Indian Ocean, the northward and southward boundary currents close the tropical and subtropical gyre (Hughes et al., 1992) and those gyres pump water into the circumpolar current and South Atlantic sub-tropical gyre that is able to feed the NADW (Toole and Warren, 1993). The ITF enhances the meridional steric height gradient and, therefore, affects the gyre's strength. This suggests that besides the capacity of adjusting the thermal and saline balance between the Pacific and the Indian Ocean, the ITF may also be able to disturb the physical condition of the distant Atlantic.

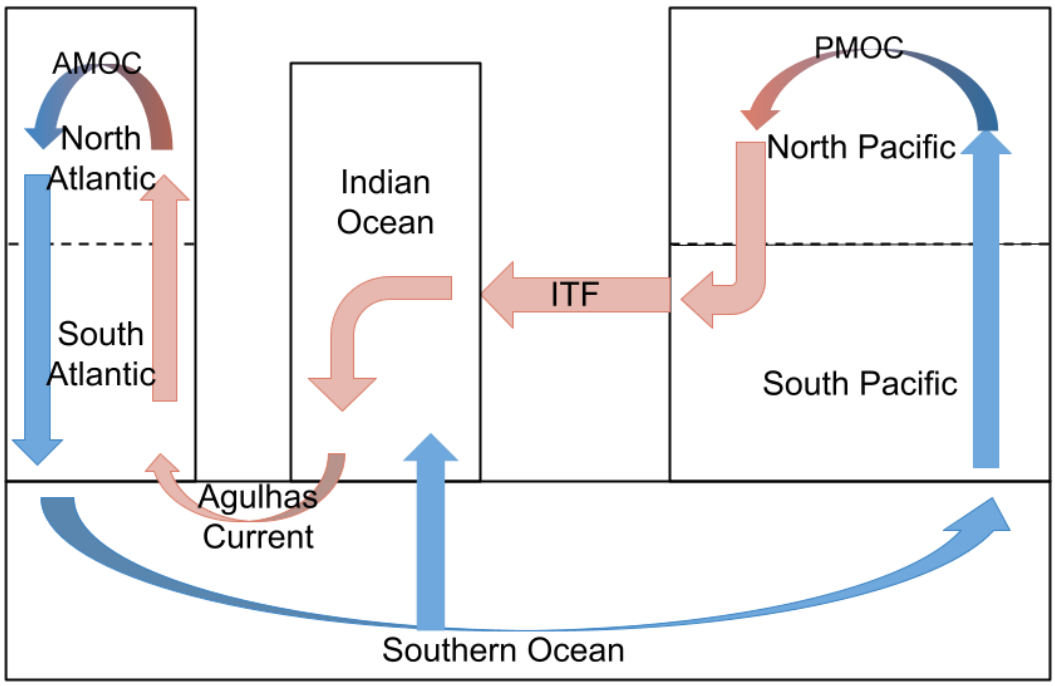

Figure 1.4 The diagram of the global meridional circulation. The red arrows indicate the warm path, and blue for the cold path. AMOC: Atlantic Meridional Overturning Current; PMOC: Pacific Meridional Overturning Current.

1.3 The Climate Effect of Indonesian Throughflow.

The unique location of the ITF is at the western end of the Pacific warm pool and the eastern end of the Indian Ocean Dipole (IOD). Consequently, the water properties of those two adjacent ocean basins are extremely affected by the ITF. Numerical simulation results suggested that the closed ITF makes the sea surface temperature (SST) warmer and cooler in the tropical Pacific and the southern Indian Ocean, as well as changing the thermocline depth in the tropical Pacific and the entire Indian Ocean (Godfrey, 1989; Santoso et al., 2011; Jin, 1997). Further, the ITF is able to affect more remote regions and currents, such as the Agulhas Current, the Atlantic and the Southern Ocean (Sprintall et al., 2014).

The ITF shows a very significant relationship with ENSO with the maximum transport volume during La Niña events and the minimum in El Niño events (Meyers, 1996). This relationship is not a one-way effect. The ITF contributes to the establishment, maintenance and collapse of an El Niño event and the El Niño weakens the ITF transport (Nicholls, 1984). On the other hand, the energy transport of the ITF plays a key role in balancing the Pacific warm pool, which suggests that there is an interaction between the ITF and ENSO. As well as the ITF, the Asian Monsoon responds to the ENSO sensitively too. As a response of the solar radiation annual cycle, the global monsoon system is not only controlled by the heating gradient and ocean-land-air interaction (Webster et al., 1998; Zhang, 2017), but also is essential for driving upper level ocean currents. By remote ocean-land or inter-basin interaction, the thermal condition in the Indian Ocean affects the Indian monsoon (Zhang, 2017) and the East Asian monsoon (Wang and Wu, 2012). Numerical

simulation results show that the combination of local and remote action of the monsoonal winds over the tropical Indian Ocean and the Pacific forms the seasonal transport variation at the Lombok Strait (Masumoto and Yamagata, 1993). The surface current in the Makassar Strait follows the seasonal wind direction (Gordon et al., 2003; Qu et al., 2005). However, the thermohaline current in the Makassar Strait shows an opposite direction to the local monsoonal wind in boreal winter, which means it is not fully controlled by the local monsoon (Miyama et al., 1995). The variation of physical parameters, such as SST, sea surface pressure, wind stress and thermocline depth, between an open and closed ITF were simulated by modelling, but the temporal order of those changes still is unclear (Santoso et al., 2011). Therefore, there is an interaction between the ENSO, ITF and Asian monsoon. This interaction will be investigated in chapter 2.

1.4 The Indonesian Throughflow at the Palaeo Scale

In the ITF palaeocean research field, the prevailing approach is the reconstruction of sea temperature and salinity from ocean core data and numerical modelling. The discussion has focused on the variability of the ITF itself over different timescales (Hendrizan et al., 2017; Zhang et al., 2018; Schröder et al., 2016), the relationship with the Indian Ocean and the Pacific (Xu et al., 2017; Rippert et al., 2015; Linsley et al., 2017), and teleconnection with the Atlantic and the Antarctic (De Vleeschouwer et al., 2018; Sarnthein et al., 2018). All these analyses focused on reproducing the hydrological situation in different periods from the Pliocene to Quaternary. In this thesis, the palaeoceanography study will focus on the deglacial process of the Last Glacial Maximum (LGM, approximately 21 ka BP).

At the LGM, the Sunda shelf, the Gulf of Thailand, the South China Sea and the Java Sea, and Sahul shelf, connecting the north coast of Australia and New Guinea, were exposed due to the sea level being 120 m lower than present (fig 1.5). This means the ITF path was

narrowed to only the Makassar Strait and the Timor Channel. By changing the ITF bathymetry in this way, previous modelling results suggest that the ITF volume transport is only reduced by 1.5 Sv because of the change of the Indonesian Sea's sea level (Di Nezio et al., 2016). However, other numerical simulation and reconstructed proxy results suggest that the ITF was strongly reduced at LGM (Müller and Opdyke, 2000; Chikamoto et al., 2012; Muller et al., 2012). Ocean core proxy studies (Ding et al., 2013; Kuhnt et al., 2004) suggest that at the LGM, unlike today, the ITF transport is dominated by saltier surface water because the monsoon increased steric height between the West Pacific and East Indian Ocean, but the overall transport is weaker than present.

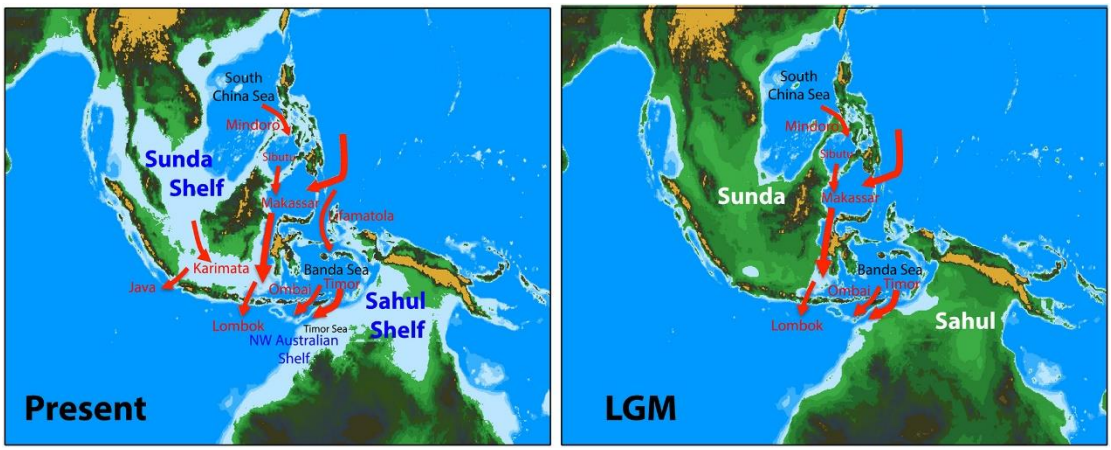

Figure 1.5 The present (left) and LGM (right) topography and bathymetry of the ITF region (Di Nezio et al., 2016).

The palaeo-modelling research carried out in this thesis will emphasise how the components of the ITF affected by past conditions, instead of just examining the influence of the ITF in sensitivity simulations. Therefore, in this research it will be simulate global ocean coupling with a simple atmosphere at a relatively high spatial resolution (detail see 4.2). Besides reconstructing high resolution hydrologic properties since the LGM, the main objective will emphasise the long term and remote influence of the ITF on the global meridional overturning circulation.

Therefore, for the contemporary study, the key tasks are:

1. How does the ENSO affect the ITF transport.

2. The finding of the shift of vertical structure of horizontal transport at the Banda Sea during the 1990s and the analysis of its potential cause.

For the palaeo study, the main aims are:

1. The effects of insolation variation on global ocean circulation during the deglacial progress since the LGM.

2. The contribution and influence of the ITF connection on the global ocean circulation during the deglacial progress since the LGM.

In this thesis, firstly the contemporary basic hydrological character of the ITF is introduced, the relationship between the ITF and ENSO, and the vertical structure of the ITF horizontal transport in chapter 2. Chapter 3 focuses on the change of the vertical structure of the modern ITF horizontal transport by using box model. In chapter 4, the palaeo-model, FRUGAL, and the simulation design are introduced, and the control simulation is analysed. The chapter 5 and 6 present the discussion of varying insolation and fully closed ITF simulations. The last chapter summaries the entire thesis.

Chapter 2 the Long-Term and Seasonal Variation Characteristics of the ITF

In this chapter, the main research subject is the basic climatological characteristics of the Indonesian Throughflow (ITF) from 1980 to 2016. The databases to be utilized in this chapter will be introduced in part 2.1, while part 2.2 will consider the relationship between ENSO and the ITF, and the long-term and seasonal variation characteristics of the ITF water properties is studied with the wind field in part 2.3.

2.1 Databases

2.1.1 SODA Reanalysis Database

The Simple Ocean Data assimilation ocean/sea ice reanalysis（SODA）is a gridded reanalysis dataset of global ocean climate. The latest SODA3 data is generated by the ocean component of the NOAA/Geophysical Fluid Dynamics Laboratory CM2.5 coupled model with 0.25° resolution, which was forced by the World Ocean Database of historical hydrographic profiles and in situ and remotely sensed SST (Carton et al., 2018; https://www.atmos.umd.edu/~ocean/). Comparing with earlier version, SODA 2, the changes include the ocean model, the addition of active sea ice, new forcing datasets, and modifications to the data assimilation scheme. Therefore, the systematic errors are reduced in SODA 3, and the performance in high latitude is improved (Carton et al., 2018). The monthly average SODA3.7.2 dataset is used here; the spatial resolution is 0.5˚, the number of vertical layers is 50 and the period covered is 1980 to 2016.

2.1.2 INSTANT Dataset

The International Nusantara Stratification and Transport (INSTANT) program aimed to directly measure the water transport from the western equatorial Pacific to the Indian

Ocean via the ITF. The observations include in situ velocity, temperature and salinity data from sea floor to surface during the period 2004 to 2006 (Sprintall et al., 2009; http://www.marine.csiro.au/~cow074/index.htm). There were two sites for the inflow current, at the south Makassar Strait and the Lifamatola Passage (between the Molucca Sea and the Banda Sea), and three for the outflow, at the Lombok Strait, the Ombai Strait and the Timor Strait (fig. 2.1).

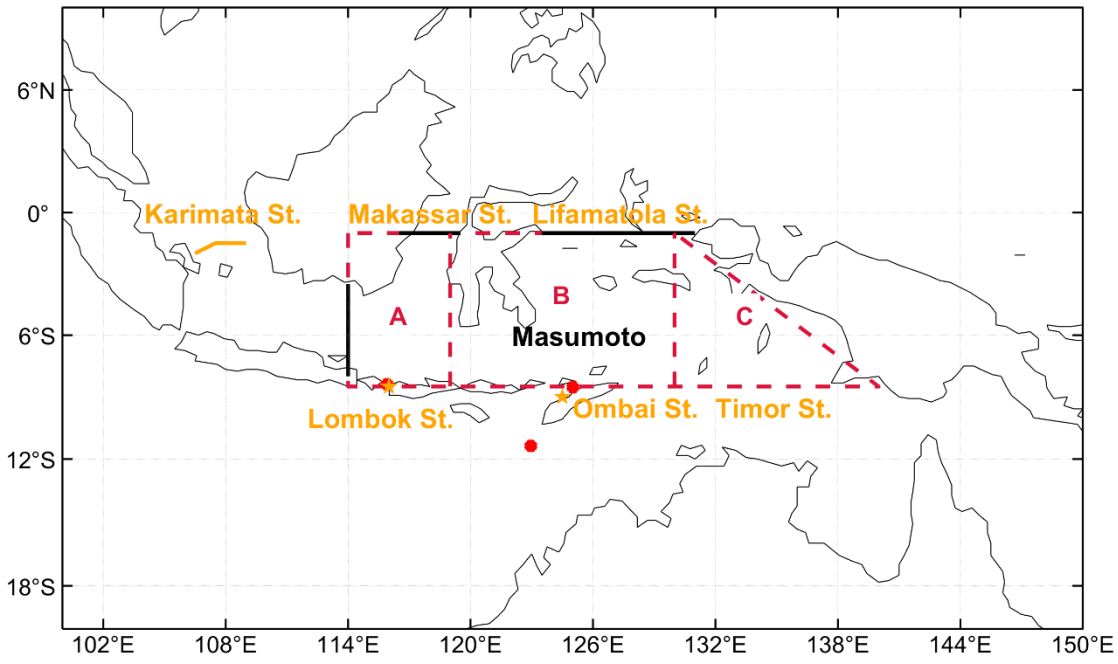

Figure 2.1 The ITF transport is integrated along the black lines. The black lines are the inflow gates based on the Masumoto and Yamagata (1993). The red dashed line box and its sub regions are utilized to study the vertical profile of transport (as Fig 2.5). The red spots are INSTANT observation sites. Key straits are shown in orange.

2.1.3 Nino 3.4 and Indian Ocean Dipole Mode Indices

The Nino 3.4 index is defined as the mean of sea surface temperature anomalies (SSTA) over the area 5˚N to 5˚S, 150˚W to 90˚W. The Indian Ocean Dipole (IOD) mode index is defined as the difference between the west (10°S to 10°N, 50°E to 70°E) and east

(10°S to 0, 90°E to 110°E) tropical Indian Ocean SSTA (fig. 2.2). When the Nino 3.4 or IOD mode index is continuously greater (less) than or equal to ±0.4℃ over 6 months, this year would be identified as El Niño (La Niña) events or positive (negative) IOD events (NCAR, https://climatedataguide.ucar.edu/climate-data/nino-sst-indices-nino-12-3-34-4-oni-and-tni?qt-climatedatasetmaintabs=1#qt-climatedatasetmaintabs). In this research, the Nino 3.4 and IODMI are provided by the National Oceanic and Atmospheric Administration (NOAA, https://www.esrl.noaa.gov/psd/data/correlation/nina34.data; https://psl.noaa.gov/gcos_wgsp/Timeseries/DMI/). Comparing with other ENSO indices, the target region of Nino 3.4 is closer to the central Pacific (fig. 2.2), which better reflects the ENSO signal in the study period.

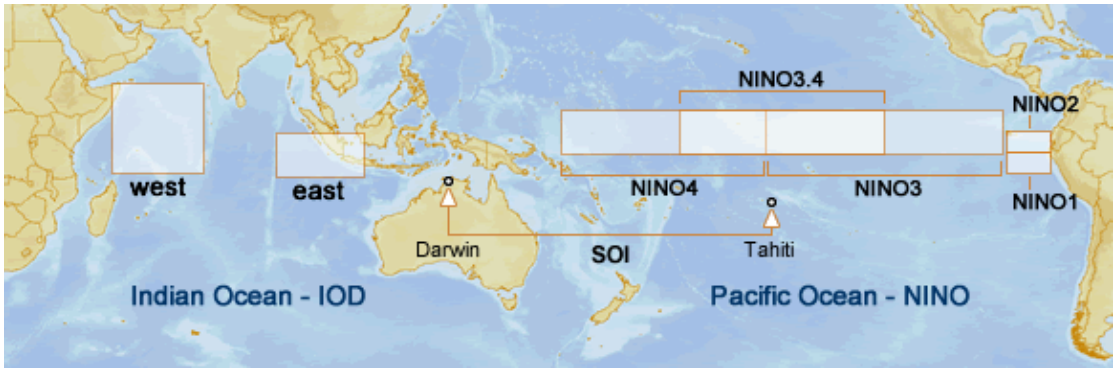

Figure 2. 2 Regions used to monitor ENSO and IOD. The NINO regions are used to monitor ENSO, with NINO3 and NINO3.4 typically used to identify El Niño and La Niña events. The IOD index (or Dipole Mode Index, DMI) is used to identify IOD events, by taking the difference between the west and east poles. (Australian Bureau of Meteorology; http://www.bom.gov.au/climate/influences/images/map-indices.png)

2.1.4 ERA5 Reanalysis Dataset

The ERA5 dataset is published by the European Centre for Medium-Range Weather Forecasts (C3S, 2017; https://www.ecmwf.int/en/research/climate-reanalysis) at 2020. Currently, this dataset covers the period from January 1950, with 1950 to 1978 as a

preliminary version. Here, the monthly reanalysis wind U and V component dataset, of 0.25° spatial resolution, is used for the same time period as the oceanic dataset, namely, 1980 to 2016.

2.1.5 The ITF Calculation Region

Because of the complex topography of the ITF area, the target research region varies a lot across the literature (see table 2.1). In this research, the target region is used as shown in figure 2.1, after Masumoto and Yamagata (1993), and compared with the INSTANT data (Sprintall et al., 2009). The INSTANT mooring observation sites are marked in red in fig 2.1. As fig.2.3 shows, the transport value calculated from the SODA data over the Masumoto region is relatively higher than the INSTANT calculation. To measure the volume transport of the whole ITF, the volume transport through the longitude ($\overrightarrow{q_u}$) and latitude ($\overrightarrow{q_v}$) side of each grid cube is calculated first, by:

$$\overrightarrow{q_u} = \vec{u} \times \Delta lat \times \Delta z; \quad (2.1)$$

$$\overrightarrow{q_v} = \vec{v} \times \Delta lon \times \Delta z; \quad (2.2)$$

The $\vec{u}$ and $\vec{v}$ are the U and V component of the current velocity; the Δlon and Δlat are the step of the longitude and latitude. In here, as the spatial resolution is 0.5°, the Δlat is computed by resolution multiplied by the radius of the earth r; and with the cube longitudinal length are calculated as,

$$\Delta lat = 0.5 \cdot \pi r/180; \quad (2.3)$$

$$\Delta lon = \Delta lat \cdot \cos(lat); \quad (2.4)$$

The Δz is the length of the depth step. The ITF transport is the sum of $\overrightarrow{q_u}$ of the Java Sea (114°E, 3.5°-8°S, Fig 2.1), and $\overrightarrow{q_v}$ of the Makassar Strait (116.5°-119.5°E, 1°S) and the Lifamatola Strait (123.5°-131°E, 1°S). To unify the sign with current direction, the $\overrightarrow{q_u}$ of the

Java Sea is multiply by -1. Therefore the negative value suggests water flow into the ITF, and the positive means flow out. Then after vertical integrating, the ITF volume transport series would be:

$$\overrightarrow{Q_{ITF}} = \sum_{z=1}^{Z}(-\overrightarrow{q_{u_{Java}}} + \overrightarrow{q_{v_{Makassar}}} + \overrightarrow{q_{v_{Lifamatola}}}); \quad (2.5)$$

For the vertical distribution of volume transport over the Indonesian Seas in fig 2.1.The volume transport of each cube (q) in the region would be,

$$q_{i,j,z} = \sqrt{\overrightarrow{q_u}^2 + \overrightarrow{q_v}^2}; \quad (2.6)$$

For measuring the transport direction easier, the velocity direction of $\vec{v}$ multiplied the volume transport, $q_{i,j,z}$. Here the i and j indicate the grid number in longitude and latitude, and the z means the number of vertical levels. The new transport with zonal direction in each cube is symbolized as $\overrightarrow{q_{i,j,z}}$.Therefore, the volume transport of the ITF, $\vec{Q}$ is decided as,

$$\vec{Q} = \sum_{z=1}^{Z} area\_ave(\overrightarrow{q_{i,j,z}}); \quad (2.7)$$

The $area\_ave()$ is the area averaged value over the ITF calculation region shown in figure 2.2. Z is the total number of levels in the vertical. The averaged value of the ITF, along the solid black lines in fig 2.1 and calculated from the SODA dataset, is -12.76±2.74 Sv during 1980 to 2016 (figure 2.3). On the other hand, the INSTANT mean ITF is -15.07±2.79 Sv during the program period, Jan 2003 to Dec 2006; the mean of the SODA calculated transport is -12.82±0.52 Sv during the same period. The INSTANT transport is simply calculated by the summation of three outflow channels' transport (Lombok, Ombai and Timor Straits; Sprintall et al., 2009). Thus, the difference between ITF volume transport by the SODA dataset and the INSTANT dataset is acceptable.

2.2 The Relationship Between ENSO and ITF

From the earlier studies, the regional monsoon is capable of affecting the surface to subsurface transport significantly (Masumoto and Yamagata, 1993; Gordon et al., 2003; Qu et al., 2005; Ahmad et al., 2019). On the other hand, the ENSO as the most important and powerful global climatological event, not only impacts on the Asian-Australian monsoon annual variation magnificently (Webster and Yang, 1992), but directly manages the water properties at the Equatorial Pacific. Therefore, to investigate the relationship between ITF and ENSO, composite El Niño and La Niña years were selected if the Nino 3.4 index deviation was greater(smaller) than 0.4 (-0.4) over at least 6 months, or if the index was somewhat variable, if all months in the same year are positive (negative). By this requirement, during 1980 to 2016, the composite El Niño years are: 1982, 1987, 1992, 1997, 2002, 2015, and the La Niña years are: 1984, 1985, 1988, 1999, 2000, 2008, and 2011 (see figure 2.3).

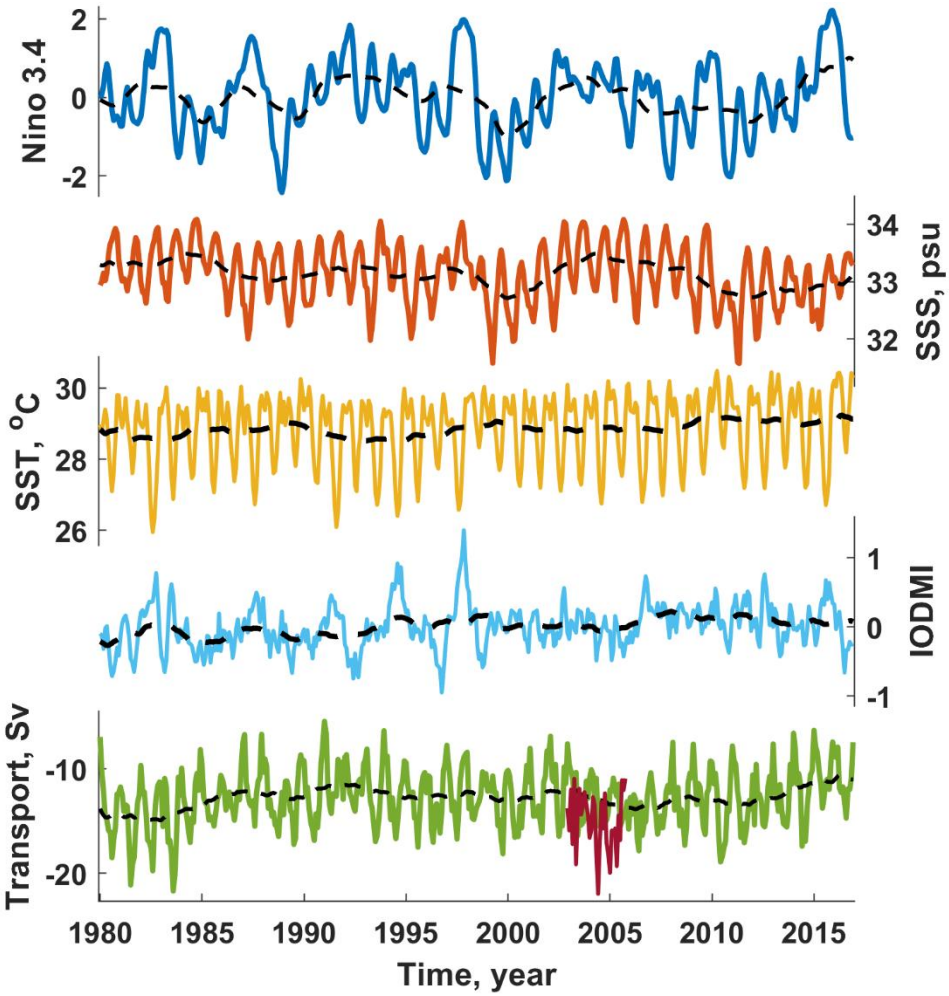

Figure 2.3 The monthly variation of the Nino 3.4 index (navy; provided by NOAA), the ITF area averaged (fig 2.1 dashed box area) sea surface salinity (SSS, orange, unit: psu; data: SODA), the ITF area averaged sea surface temperature (SST, yellow, unit: ℃; data: SODA), the Indian Ocean Dipole mode index (blue; provided by NOAA), the calculated ITF transport from SODA dataset (green, unit: Sv) during 1980 to 2016 and transport from the INSTANT (red, unit: Sv; provided by INSTANT project) during Jan 2003 to Dec 2006. The dashed lines indicate the 3 years moving averaged result.

The difference of the SSS, SST and layer 1 transport between El Niño and La Niña composites have been plotted for the four seasons (fig 2.4). For spring, the near ground wind field suggests that compared to La Niña, in the El Niño years:

i) the South Indonesian Seas have a north wind bias, which helps ITF water flow into the Indian Ocean;

ii) the north Makassar Strait to the New Guinea area has a strong west wind anomaly, which restrains the NGCC supplying the ITF;

iii) the south wind bias over the Philippine Trench would decreases the MC;

iv) the perturbed south wind over the SCS restricts water passing the Karimata Strait.

The spring sea surface salinity anomaly (SSSA) distribution (fig 2.4.(1)) fits the wind deviation field well. The Makassar Strait, the Philippine Trench and the east of the Arafura Sea are fresher in El Niño years than La Niña years; the Banda and the Java Sea is saltier. The sea surface temperature anomaly (SSTA) distribution (fig 2.4.(2)) is characterised as having a strong warm bias in the west Equatorial Pacific, but being cooler over the rest of the ocean area in El Niño years. The most significant fresh bias centre at the Makassar Strait matches with the warm bias centre. The west wind anomaly above the NGCC, makes the current retroflect back to the Pacific as fig 2.4.(3) shows. Generally, the perturbed wind field restrains the warm and salty South Pacific water from entering the ITF and helps water flow into the Indian Ocean, therefore the SSTA over the Banda Sea is different than in the NGCC but compatible with outflow in the Indian Ocean, especial as seen in the SSSA distribution.

In summer, the El Niño west wind anomaly in the equatorial region increased further and is located further south. The strong southwest wind bias dominates the whole Banda Sea. The SSSA field (fig 2.4.(4)) suggest that compared with La Niña years, during El Niño the NGCC feeds less water to the ITF or even receives water from the Banda Sea in such years. The fresher centre at the Makassar Strait is milder in summer compared to spring; the saltier bias not only appears at the Banda Sea but also in the Java Sea. In SSTA distribution (fig 2.4.(5)), the whole Indonesian Sea and the west Equatorial Pacific present a cooler El Niño

anomaly, with only the north of Australia having warmer conditions. The weak south wind anomaly over the Karimata Strait during El Niño creates a weak northward transport bias (fig 2.4.(6)); as with spring, the strong west wind deviation above the NGCC, makes it retroflect more in El Niño years; the mild north wind bias over the MC, helps make the latter stronger, but the strong southwest wind bias make the Makassar Strait and the Celebes Sea transport less water from the Pacific in El Niño than La Niña years.

In the autumn SSSA field, figure 2.4.(7), the northwest Pacific, the Sulu Sea and SCS are fresher, and the Java and Banda Sea are saltier, in El Niño than La Niña years. The strongest fresher and saltier centres are found in the Sulu and north Banda Seas. The SSTA field (fig 2.4.(8)) shows a colder bias over the whole Indonesian Seas and the west Pacific. The coldest bias centre of the Indonesian Seas is located in the east SCS, across to the Sulu Sea. The perturbed wind distribution suggests a weaker MC and NGCC water supply, and less transport via the Makassar Strait but more transport from the Banda Sea. The transport anomaly field (fig 2.4.(9)) presents a similar anomaly feature with the wind field, except that the Banda Sea maintains an indistinguishable outflow between El Niño and La Niña years.

For winter, in figure 2.4.(10), besides the south Banda Sea and Flores Sea, the rest of the Indonesian Seas is fresher in El Niño years. The powerful fresher bias centre occupies most of the northwest Pacific, the Philippine Trench and the Makassar Strait. The SSTA (Fig 2.4.(12)) shows a strong warmer centre at the Equatorial Pacific, NGCC area, the Celebes Sea and the Makassar Strait; a cooler anomaly is found in most of the Indonesian Seas. The wind anomaly field suggests that including the East Asia and the South Indonesian Seas, the winter monsoon is stronger in El Niño than La Niña years, which matches present study results (He and Wang, 2013). Consequently, the transport anomaly distribution (2.4.(12)) matches the wind anomaly. There is more water flow from the SCS via the Karimata Strait but less

transport via the Makassar Strait. The NGCC provides less water into the ITF in El Niño years.

El Niño events usually develop during the upcoming winter season, but the development of La Niña is more irregular. On the other hand, the seasonal variation of the Indonesian Seas is extremely strong. Therefore, although the composite seasonal distribution between El Niño and La Niña is limited by the asynchronous developing process, it can still characterises the relationship between the ENSO and ITF. The composite analysis of the positive and negative phase of the IOD did not present a significant difference. Therefore, the result is not shown here.

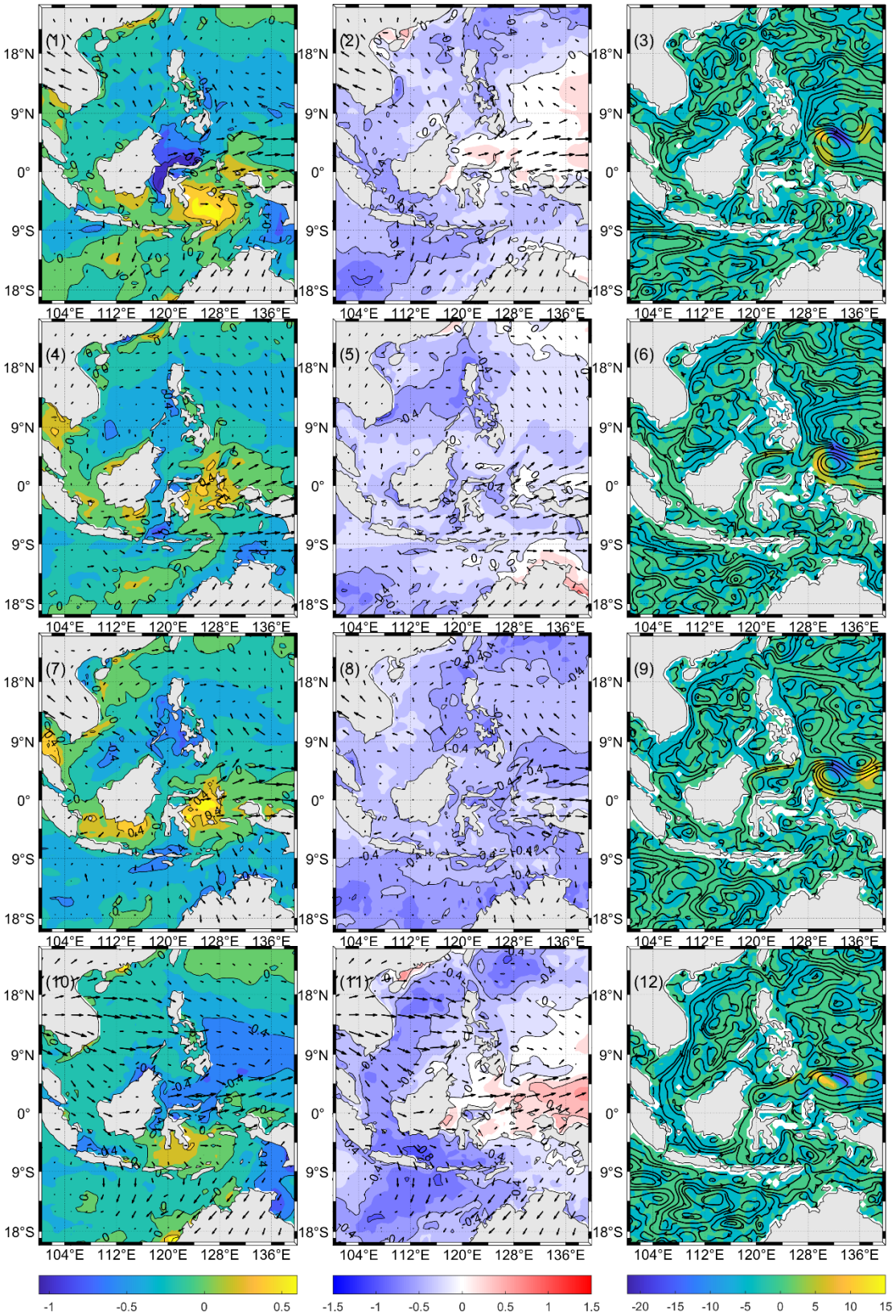

Figure 2. 4 The deviation field of the SSS(1st column; data: SODA), SST(2nd column; data: SODA) and transport over layer 1(3rd column; calculated from SODA) between El Niño and La Niña years at boreal spring(1st row), summer(2nd row),

autumn(3rd row) and winter(4th row), units are psu, ℃ and Sv. The quiver field is wind deviation field at 1000 hPa, data source: ERA5; the streamline indicates the current deviation.

2.3 The Decadal and Seasonal Variation Characteristics of the ITF under Modern Climatology

2.3.1 The Decadal Variation Characteristics of the ITF during 1980 to 2016

Long term variation of the water properties and the transport of the ITF in the modern climate benefits from a better understanding of the decadal variability. Here, the monthly averaged sea surface salinity (SSS), sea surface temperature (SST) and transport of the ITF between 1980 to 2016 are presented in figure 2.3. The ITF region is the same as for Masumoto and Yamagata (1993). The standard deviation of the ITF SSS is 0.52 psu. The maximum of the SSS is 34.08 psu and appeared in September of 2005; the minimum is 31.57 psu during May 2011. The SSS showed a similar inter-decadal variation to the Nino 3.4 Index (compare the dashed lines). The three year moving averaged Nino 3.4 and SSS have a very strong positive correlation (0.304, significant at the 0.01 level). The standard deviation of SST during 1980 to 2016 is 0.98℃. The peak temperature was 30.48℃, which occurred in April of 2010; the lowest temperature was 25.95℃ in August 1982. The variation of the SST is more stable than the SSS. Nevertheless, using the 3 year moving mean, the correlation coefficient between SST and Nino 3.4 index is 0.31, which also passed the 0.01 significance level. Note that the SST and SSS shown an extreme significant positive correlation (0.6), which suggests that combinations of warm and saltier water or cold and fresher water affect the ITF region at the same time. This result matches variation in the characteristics of the principal ITF water source: the Mindanao Retroflection along the Philippine Trench, sends fresh and cool water from the North Pacific to the ITF; the Halmahera Retroflection

following the northern New Guinea coastline, feeds the ITF with warm and salty South Pacific water.

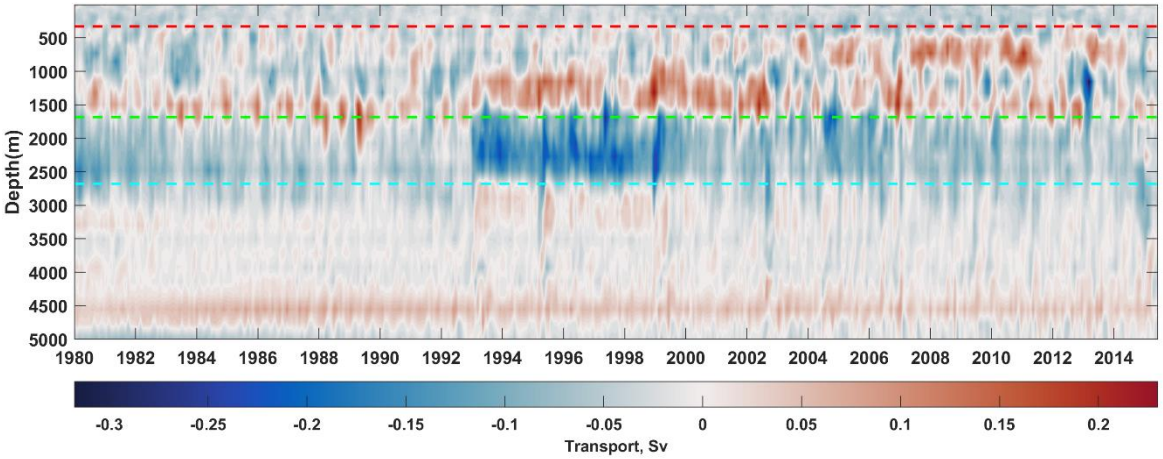

Figure 2.5 The vertical distribution of the monthly averaged ITF perturbed horizontal transport during 1980 to 2016, the northward transport in positive and vice versa, unit: Sv. The transport anomaly is asked by variance with the average of each layer. The dashed lines indicate different levels: top layer over depth range of surface to 330 m, middle layer over ~330-1500m and the deep layer over ~1500-2700 m. Levels are decided by the vertical mean of the volume transport over the periods of before, within and after the shift.

The transport of the ITF is the most essential property in this gateway. During 1980 to 2016, the standard deviation is 2.74 Sv (1 Sv = 1 x 10^6 m^3) southwardly every month; the highest southward record is 21.7 Sv in August 1983, the lowest southward is 5.4 Sv in January 1991. The correlation coefficient between the ITF transport and Nino 3.4 is 0.018 and 0.019 with the IODMI. However, after carrying out 3-year moving averaging, the transport of the ITF had a significant correlation with ENSO (correlation coefficient: 0.45, which is statistically significant at the 0.001 level), and a lesser, but still significant (at 0.01 level) correlation with the Indian Ocean Dipole (IOD) events (correlation coefficient: 0.128,

fig 2.3). Thus, the ITF transport is influenced by the ENSO cycle variation rather than individual seasons and has only weak links to the IOD.

The extremely complicated bathymetry of the Indonesian Seas leads to its unique oceanographic state. Therefore, examining the vertical structure of the ITF is important for a better understanding of this current. Figure 2.5 presents the vertical structure of the monthly ITF transport during 1980 to 2016. Generally, the transport shows a clear vertical pattern of transport direction reversal. From near the surface to about 400 m depth, southward transport prevailed all the time, although above ~100m, the transport direction has a strong seasonal variation (fig. 2.5). In the deeper layer between 400 m and 2000 m northward transport occurred much of the time. Deeper, from ~2000 m to 3000 m there was weak southward transport; below 3000 m the transport shows an oscillating pattern, although relatively little of the basin reaches such depths so the reality of this feature is debatable.

There are two noticeable shifts in the time series, at about 1994 and 2000. After the first shift, the northward transport layer between 1000-2000 m has lifted to 500-1500 m, and the transport strength slightly increased. In the meantime, the layer below has lifted from about 2000-3000 m to ~1500-2700 m and strongly strengthened, the vertically averaged transport increased 124%. The first shift started with the upper northward transport layer lift in 1992; the most significant anomaly, the southward transport layer between ~1500-2700 m, appeared around 1993 and ended about 2000. After the perturbed southward transport anomaly stopped, the upper northward perturbed transport was prolonged for two more years.

To further understand the origin of the shifts the ITF calculation area is separated into 3 parts, guided by the bathymetry (fig 2.2). The region A mainly is the eastern Java Sea and the southern Makassar Strait; the region B contains the Flores Sea and most of the Banda Sea; the region C includes the east of the Banda Sea and the North of the Arafura Sea. Figure 2.6

shows the vertical distribution of the transport over these three regions. The shift during 1992 to 2000 is easily seen in region B. For all 3 regions, there are several strong transport cores at depth between ~500-1500 m, but the direction is opposite between different regions, which means the whole ITF transport vertical distribution is not changed significantly. In summary, the vertical stratification shift of the ITF transport happened in the Banda Sea during 1993 to 2000.

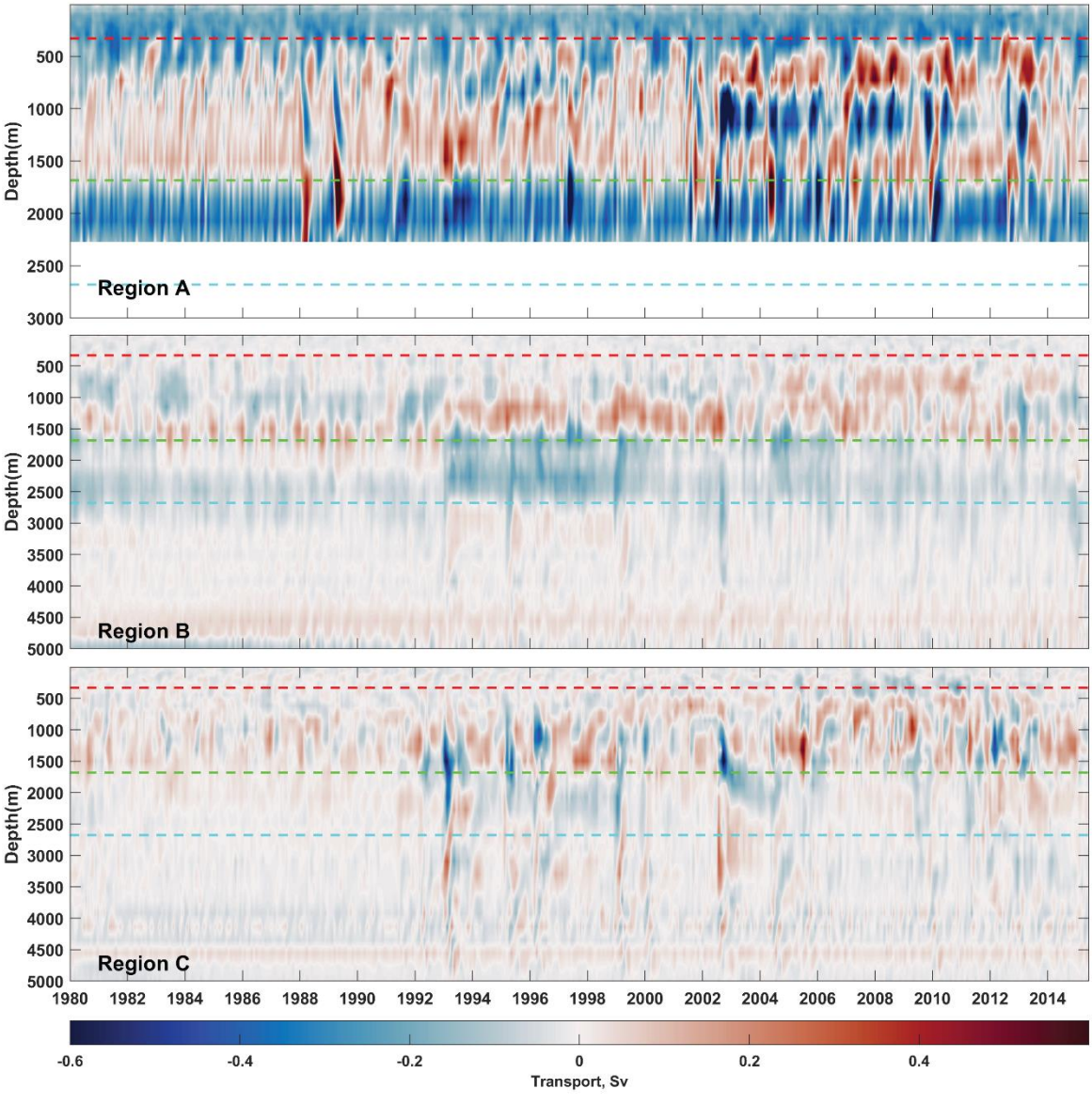

Figure 2. 6 The vertical distribution of horizontal transport over region A, B and C (see Fig 2.1), northward transport in positive and vice versa, unit: Sv.

2.3.2 The Seasonal Variation of the ITF during 1980 to 2016

To discover the cause of these two shifts, the water column is split into its 3 principal layers, as guided by fig. 2.5: the layer 1 from the surface to 330 m, the layer 2 from 330 m to ~1500 m and the layer 3 from ~1500 to ~ 2700 m. Figure 2.7 shows the mean seasonal transport and wind field (from the ERA5 dataset) during 1980 to 2016 over layer 1. Here, all seasons are determined by the Northern Hemisphere, where March, April and May are the spring, June, July and August are the summer, September, October and November make up the autumn, and December, January and February are winter. The upper layer, 1, is mainly driven by the wind, therefore, the seasonal variation is most noticeable in this layer. There is a significant pathway prevailing over the whole year, which transfers water from the Mindanao Current (MC) to the Celebes Sea and via the Makassar Strait flowing into the Indian Ocean by the Lombok Strait. The strength of this pathway varies with seasons, reaching a maximum in summer and a minimum in winter. However, there is also a significant second inflow where the New Guinea Coastal Current (NGCC) supplies South Pacific water to the ITF via the Lifamatola Strait. The third water supply route is from the South China Sea (SCS) to the Java Sea via the Karimata Strait. In spring, the NGCC is relatively strong; under the northwest wind effects, the SCS presents anti-clockwise current in the north, and feeds relatively more water to the ITF via the Sulu Sea than the Karimata Strait. Throughout the year the Makassar Strait is the largest inflow for the ITF. In summer, the strong southwest monsoon makes the NGCC much weaker than in the rest of the year. By the time of the southeast monsoon in the SCS, the SCS mainly is controlled by weak northward transport through the Karimata Strait. Note that the strong south monsoon in the summer dominates the whole Indonesian Seas, therefore, the transport is generally smaller than at other period of year. In the autumn, the NGCC strengthens, compared with the summer, and the transport reverses back to southeast in the Karimata Strait. In winter, the

NGCC significantly weakens. Under the strong winter monsoon, the SCS becomes the second most important inflow to the ITF via the Karimata Strait, leading to the Banda Sea showing an anticlockwise current. Overall, the ITF current in layer 1 is tremendously influenced by the wind field; the volume transport seasonal variation follows the monsoon pattern variation.

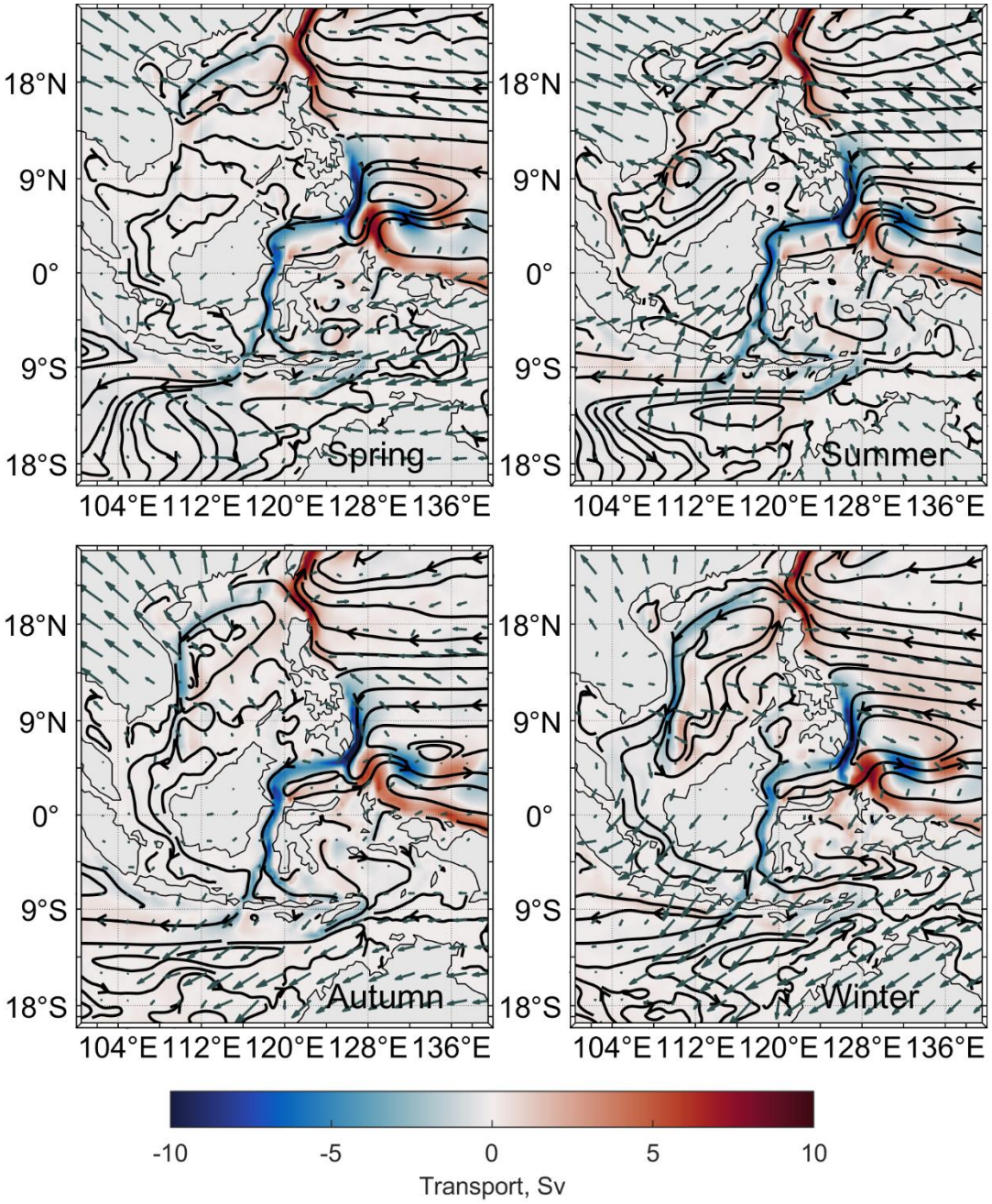

Figure 2.7 The seasonal averaged transport distribution during 1980 to 2016 over depth layer 1 in contour, unit: Sv. The positive value in contour means northward

transport. The black streamline indicates the ocean current stream; the grey quiver indicates the wind field at 1000 hPa, unit: m s^{-1}, same below.

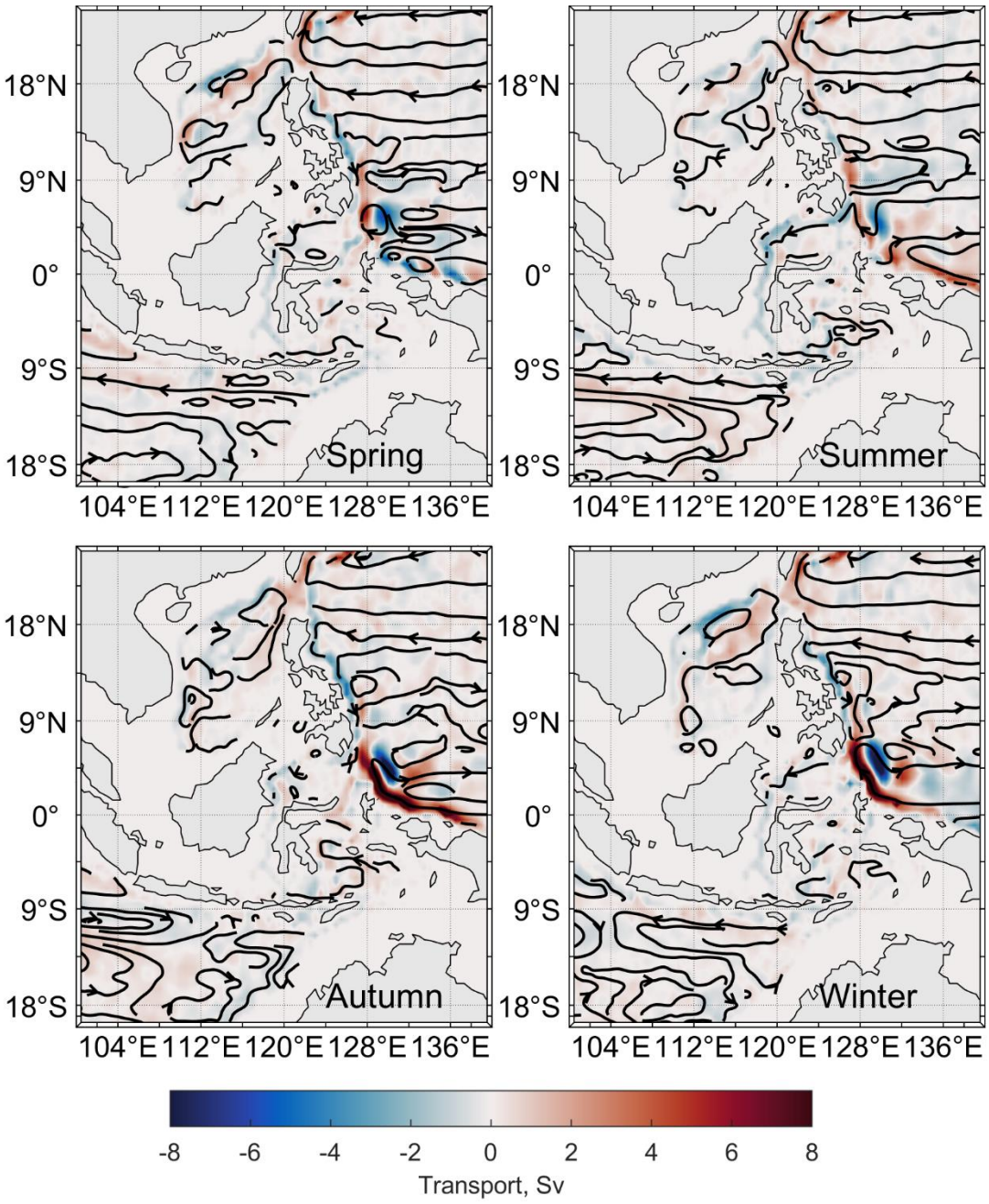

Figure 2.8 The seasonal averaged transport distribution during 1980 to 2016 over depth layer 2, unit: Sv. The blank data is resulted from the bathymetry at this depth.

Figure 2.8 shows the mean seasonal transport averaged over layer 2. In fig 2.8 and 2.9, there are streamlines at isolated basins look like that not connected with any upstream

nor downstream, due to the depth. However, there is data at channels, like the Lifamatola Strait, but the number of those data is not enough for plotting out. The strength of volume transport in this layer varies tremendously. The MC, and especially the NGCC, powerfully feed water into the ITF, but the SCS plays no role. The main seasonal difference is in the strength of the MC and NGCC. The strength of the MC and NGCC both reach a peak in winter and are lowest in the summer at this layer. The inflow path of the Celebes Sea to the Makassar Strait is most noticeable in summer. However, some basins are shallower than 330 m making the pattern of transport at this level in the Indonesian Seas complex.

The averaged transport over layer 3 is presented in fig.2.9. In this layer, the volume transport quantity is extremely small. The most significant difference in this layer is the current along the southern Malaysian Trench. This current flows southward in winter and spring, but northward in autumn and summer. The strength of this current approaches a maximum in spring and autumn.

The transport anomaly seasonal distribution during 1980 to 1992, 1992 to 2000 and 2001 to 2016 are shown in the appendix (fig S1-S6). The main differences between layers 1 and 2 and the period have been listed in table 2.1. Because the transport value in layer 3 is extraordinarily small, the following discussion will not include this layer. A summary of the Table can be presented as follows. An east(west) wind anomaly above the NGCC occurs when there is a north(south) wind anomaly above the MC and this combination will increase(decrease) the water supply for the ITF. The transport of the Karimata Strait is highly influenced by the wind field. For the period of the shift (1993 to 2000): 1) in layer 1, the MC is perturbedly weaker over the whole year, and the NGCC is stronger only in spring; 2) the summer and winter monsoon are both significantly weaker than the average over the SIS and East Asia.

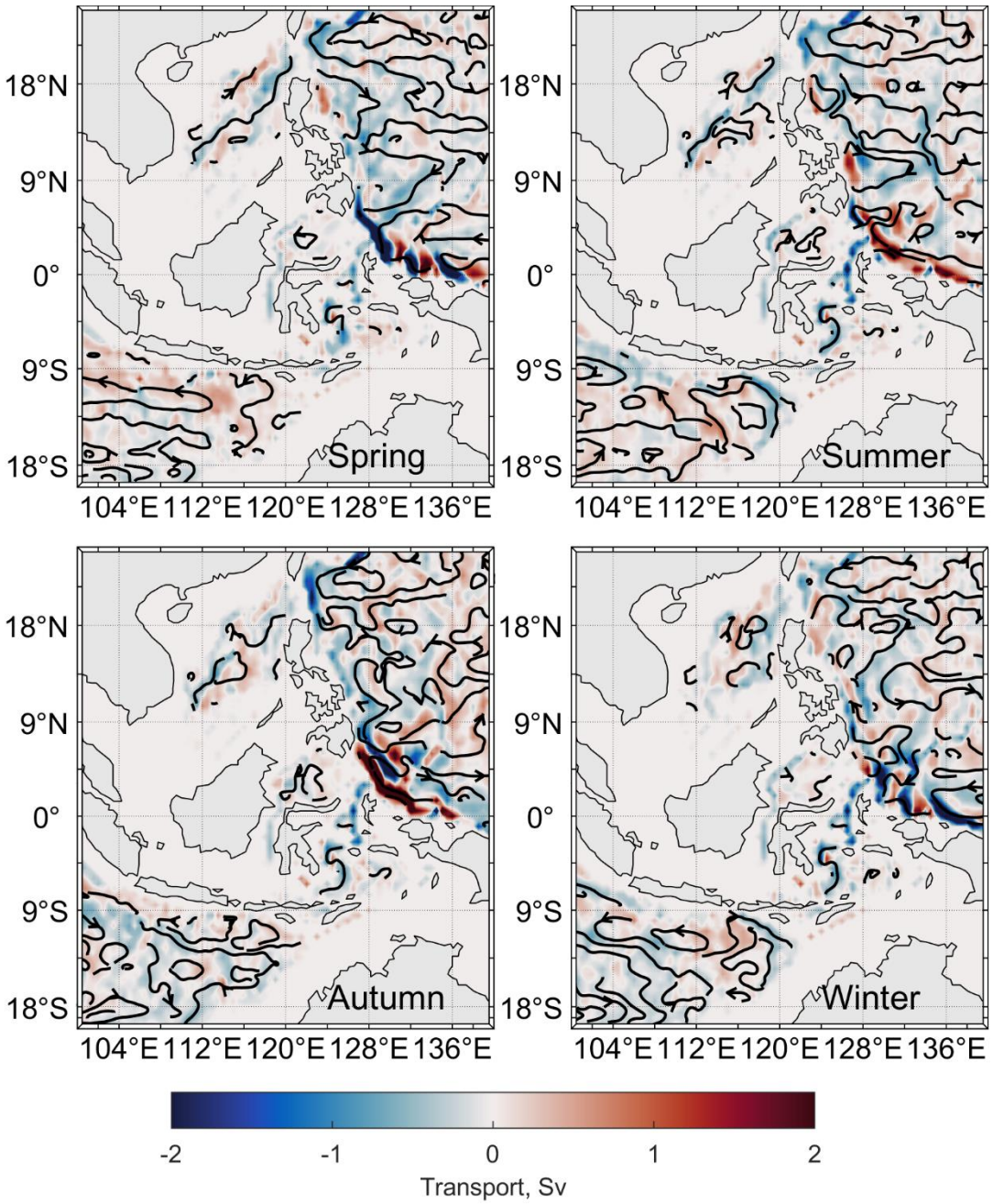

Figure 2.9 The seasonal averaged transport distribution during 1980 to 2016 over depth layer 3, unit: Sv. The blank data is resulted from the bathymetry at this depth.

2.4 Discussion and Conclusions

The ENSO adjusts the water properties of the ITF by changing the water supply and the monsoon anomaly. However, as fig 2.3 shows, overall the volume transport of the ITF is not strongly affected by the ENSO. Nevertheless, the properties of the Indonesian Seas do change in the long term and the vertical distribution of the ITF transport presents a clear shift

in transport direction layers during the study period (fig 2.5). This shift is located in the Banda Sea and occurred between 1993 and 2000 (fig 2.6). The mechanism causing this shift will be investigated in Chapter 3.

Table 2.1 The variation of transport and wind field in key regions over different periods. SCS: the NP: the North Pacific, SIS: the South Indonesian Seas.

Period	Layer	NGCC	MC	SCS	Wind field
1980-1992	1	Weaker in all seasons	Stronger in all seasons, most strengthened in winter	In spring, summer and winter, more water flowed into ITF	Spring: strong west wind bias in Equatorial area; summer: weaker in SCS/NP but stronger at Makassar Strait
	2	stronger in all seasons	Not significant	Weak southward bias along the west boundary	
1993-2000	1	Except spring, strengthened at others	Weakened in all seasons	Except in spring, more water flowed into ITF	Spring: strong southwest bias in NP; south bias in SIS Summer: east bias in SIS; Autumn: strong east bias above NGCC; Winter: strong East Asian monsoon
	2	Noticeably strengthened in spring	Northward bias at north Philippine Trench in autumn	Not significant	
2001-2016	1	weakened in all seasons, especial in winter	Strengthened in all seasons, especial in spring and winter	Western boundary effect is more significant; less water supply via the Karimata Strait	All: west bias in equatorial area; Summer: weak East Asian monsoon; Winter: weak monsoon in SIS;
	2	Noticeable strength in spring and autumn; weaker in summer and winter	Northward bias at the north Philippine Trench in all seasons	Northward anomaly along the west SCS.	

Chapter 3 A Box Model Causal Analysis of the Vertical Profile Shift of the Indonesian Throughflow Transport during 1993 to 2000

The shift of the vertical distribution of the ITF transport that occurred over 1993 to 2000 was introduced in part 2.3. Here, this shift was identified as occurring in the Banda Sea basin. In this chapter, the cause of this shift is studied using a simple box model. Section 3.1 will explain the design of the box model and experiments. The experiments' results will be presented in 3.2, and discussed in 3.3.

3.1 The Design of the Box Model and Experiments

3.1.1 The Box model Design

The box model employed here is based on the idealized model for the thermohaline circulation developed by Stommel (1961). Figure 3.1 shows the schematic diagram of the Banda Sea box model. For this model the Banda Sea is delimited by the box shown in fig.3.2; the area of each box is 5.27×10^4 km^2, and the thickness of boxes 1, 2 and 3 are 330m, 1353m and 607.5m respectively, which are same as the thicknesses of layers 1, 2 and 3 in chapter 2. The water is assumed to be well mixed within each box, therefore the temperature and salinity are uniform in each box. The mass and energy are exchanged by pipes which connect each of the boxes. The atmosphere-ocean interaction is simulated by the total fresh water and heat fluxes at the top surface of box 1. The thermohaline fluxes between the layers, denoted as Q_{12} andQ_{23}, and those with the Pacific side boundary, P_1, P_2 and P_3, and the Indian Ocean (IO) side, I_1, I_2 and I_3, are driven by density differences.

The advective fluxes Q_{nm} between boxes n and m, and P_n between the boxes n and the Pacific side boundary, are calculated from Marotzke (2000):

$$Q_{nm} = k_{nm}[\alpha(T_n - T_m) - \beta(S_n - S_m)], \quad (3.1)$$

$$P_n = k_{xn}[\alpha(T_p - T_n) - \beta(S_p - S_n)], \quad (3.2)$$

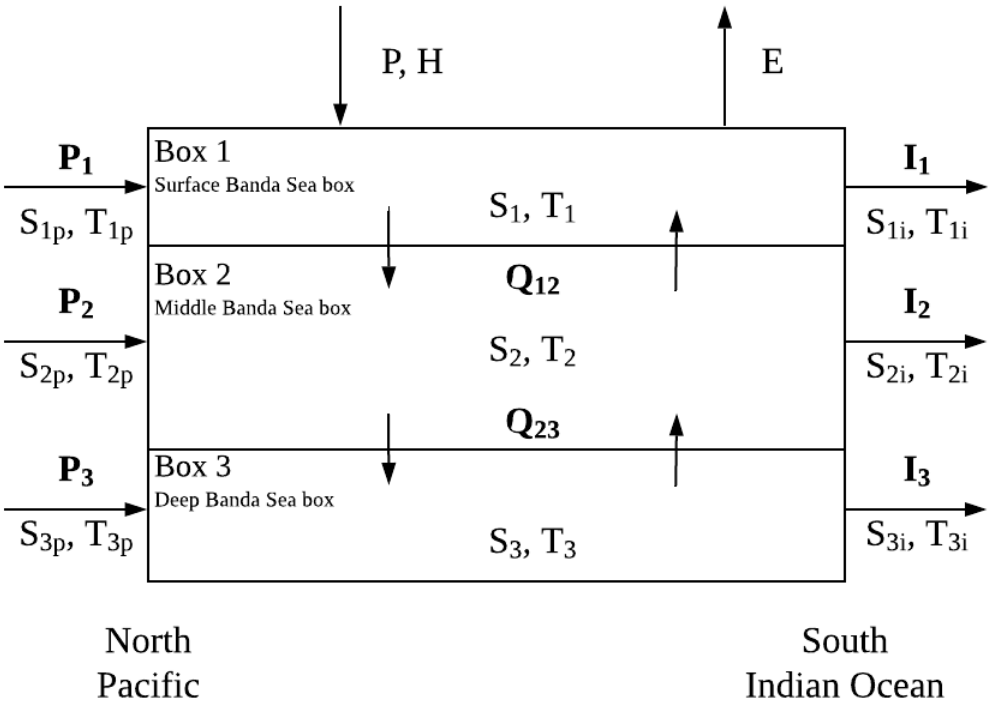

Figure 3.1 The schematic diagram of the box model. The boxes 1, 2 and 3 indicate the layers 1, 2 and 3 in chapter 2; the P_1, P_2 and P_3 mean the inflow from the Pacific in different layers; I_1, I_2 and I_3 mean the outflow to the Indian Ocean in different layers; Q_{12} and Q_{23} standard the vertical exchanged between box 1\2 and 2\3. All S and T represent the salinity and temperature fluxes, which exchanges with the current. The P is the precipitation and H is the heat flux with the atmosphere; E is the evaporation.

The T and S here mean the temperature and salinity of the boxes or side boundary input data (see table 3.3); the thermal (α) and saline (β) expansion coefficients of seawater are listed in table 3.1. The hydraulic constant (k) is a tuneable parameter which described all the dynamics of the thermohaline current (see values in table 3.2). Based on (3.1) and (3.2), the theoretical hydraulic constants (k_t) for each flux, excepts I_n, are decided by,

$$k_{tnm} = \frac{Q_{nm}}{\alpha(T_m - T_n) - \beta(S_m - S_n)}, \quad (3.3)$$

Where the Q_{nm} here is the long-term averaged volume transport of each flux, listed in table 3.2. To clarify, in table 3.2, the fluxes from the Pacific are determined by the vertical sum of each box thickness of the north boundary of the Banda Sea basin instead of the full ITF itself, therefore the values of P_s are significantly smaller than the ITF volume transport. The T_n/T_m and S_n/S_m are the climatological mean temperature and salinity of box n/m or side boundaries (see table 3.3). All the k_t are listed in table 3.2. However, the wind field and the Ekman effect play essential roles in the Banda Sea area (Gordon and Susanto, 2001). Moreover, the box 1 only interacts with the atmosphere by heat and freshwater fluxes exchange. Therefore, the k values should not only be decided by (3.3), but also need to adjust. On the other hand, the Ctl run result by the k_t presents an extremely unstable transport in box 2 and 3 (see S7 and 8). Thus, to obtain a better equilibrium, the k values used in the following simulation are adjusted and listed in Table 3.2.

Table 3.1 Values of parameters used in the box model (Kahana et al., 2004).

Parameters	Notation	Value
Thermal expansion coefficient	α	$1.5 \times 10^{-4}\ K^{-1}$
Saline expansion coefficient	β	$8 \times 10^{-4}\ psu^{-1}$
Seawater density	ρ_o	$1026\ kg\ m^{-3}$
Heat capacity of seawater	$C_{p,o}$	$3990\ J\ kg^{-1}\ K^{-1}$
Thermal coupling strength	λ	$35\ \mathrm{W}\ m^{-2}\ K^{-1}$
Reference salinity	S_r	$35\ psu$

All advective exchanges calculated in this way are scalar quantities. The directions of these exchanges are determined by the density difference. Here, a simplified linear density calculation is utilized, as,

$$\rho = \rho_0(1 - \alpha T + \beta S), \tag{3.3}$$

where the ρ_0 is seawater density, using the value in Table 3.1. To maintain the mass balance, the transport between boxes and the Indian Ocean side boundary is calculated by,

$$P_1 + P_2 + P_3 = I_1 + I_2 + I_3, \tag{3.4}$$

For each box, the flux to the Indian Ocean is determined by the mass balance, as:

$$I_1 = P_1 - Q_{12} + FW^C, \tag{3.5}$$

$$I_2 = P_2 + Q_{12} - Q_{23}, \tag{3.6}$$

$$I_3 = P_3 + Q_{23}, \tag{3.7}$$

The FW^C is the long-term climatological averaged freshwater flux, which will be introduced in (3.17).

Table 3.2 The thermohaline flux properties.

Flux	Description of location	Value based on SODA (Sv)	Theoretical hydraulic constant, k_t ($10^6\ m^3\ s^{-1}$)	Selected hydraulic constant, k ($10^6\ m^3\ s^{-1}$)
P_1	Box 1and Pacific side boundary	0.4 (Southward)	2156.49	2156.49
P_2	Box 2 and Pacific side boundary	0.23(Northward)	11698.09	1118.57
P_3	Box 3 and Pacific side boundary	0.31(Southward)	2782.01	45.53
Q_{12}	Box 1 and 2	0.02 (upward)	7.75	7.75
Q_{23}	Box 2 and 3	0.09 (upward)	149.69	117.67

Based on the NCEP/NCAR (National Centers for Environmental Prediction – National Center for Atmospheric Research) reanalysis 1 (Kalnay et al., 1996), the

climatological downward surface heat fluxes (Q_1^c) of box 1 is calculated by the sum of the latent heat (LH), sensible heat (SH), net longwave radiation (NL) and net shortwave radiation (NS), as,

$$Q_1^c = NS - (LH + SH + NL). \tag{3.8}$$

From the Haney-type boundary (Haney, 1971), under the Newtonian cooling law, the modelled reservoir heat flux of the box 1 (Q_1^m) would be:

$$Q_1^m = \lambda(T_1^* - T_1^m), \tag{3.9}$$

Where λ is the thermal coupling strength (table 3.1), T_1^m is the modelled box 1 temperature and T_1^* is the prescribed apparent temperature of box 1, defined as,

$$T_1^* = T_1^c + \frac{Q_1^c}{\lambda}, \tag{3.10}$$

The long-term climatological averaged temperature of box 1, T_1^c, is calculated from the SODA data (section 2.1.1).

The box 1 restoring time constant (τ_1) is related to λ, as:

$$\tau = \frac{C}{\lambda} = \frac{C_{p,o}\rho_o D_1}{\lambda}, \tag{3.11}$$

Where C is the heat capacity per unit area, $C_{p,o}$ is the specific heat capacity of seawater (Gill, 1982), and ρ_o is a reference density of seawater (see table 3.1). The D_1 is the depth of box 1. Therefore the equation (3.9) can be written in:

$$Q_1^m = \frac{C_p\rho_o D_1}{\tau}(T_1^* - T_1^m), \tag{3.12}$$

And then the modelled heat flux of box 1, $H_{T_1}^m$ is,

$$H_{T_1}^m = Q_1^m \times A_1 = \frac{C_p\rho_o D_1 A_1}{\tau}(T_1^* - T_1^m) = \frac{C_p M_1}{\tau}(T_1^* - T_1^m). \tag{3.13}$$

The A_1 and M_1 represent the area and mass of water respectively in box 1. Therefore, the rate of temperature change in box 1 due to atmosphere-ocean exchange is represented by

$$\frac{\partial T_1^m}{\partial \mathrm{t}} = \frac{1}{\tau}(T_1^* - T_1^m) = \frac{H_{T_1}^m}{C_p M_1}, \tag{3.14}$$

For box n, the rate of change of the temperature caused by exchanges with side boundary m or box m, is calculated by,

$$\frac{\partial T_n^m}{\partial \mathrm{t}} = \frac{|Q_{mn}|(T_m - T_n)}{V_m}. \tag{3.15}$$

The Q_{mn} and T_m are the transport between box n and side boundary (box) m and temperature of side boundary (box) respectively. Therefore the time rate of temperature change for box 1 is given as:

$$\frac{\partial T_1^m}{\partial \mathrm{t}} = \frac{H_{T_1}^m}{C_p M_1} + \frac{|Q_{1m}|(T_m - T_1)}{V_1}, \tag{3.16}$$

The salinity of box 1 is not only decided by the mass exchanges with side boundaries and box 2, but also the surface freshwater fluxes. The surface freshwater flux depends on the evaporation €, precipitation (P) and runoff. However, there is no major river on the islands surrounding the Banda Sea. Thus, the surface freshwater flux for box 1 with area A_1 is,

$$\mathrm{FW} = (\mathrm{E} - \mathrm{P}) \times A_1. \tag{3.17}$$

Because the long-term climatological freshwater flux (FW^C) would change the volume of the box 1, and the volume of boxes is fixed, therefore the "virtual" salinity flux (Kahana et al., 2004) is employed here, H_S^C,

$$H_S^C = S_r \times \frac{FW^C}{V_1}, \tag{3.18}$$

where S_r is the reference salinity, 35 psu. Utilizing the similar Newtonian restoring law on the box 1 salinity with the same time parameters in (3.11), the modelling restoring salinity of box 1 can be written as,

$$H_{S_1}^m = \frac{1}{\tau}\,(S_1^* - S_1^m), \tag{3.19}$$

where the prescribed apparent salinity, S_1^*, is calculated:

$$S_1^* = S_1^C + \frac{FW^C \times S_r}{V_1} \times \tau = S_1^c + H_{S_1}^C \times \tau \tag{3.20}$$

Here the S_1^C is the climatological salinity of the box 1, calculated by the SODA dataset (section 2.1.1). Therefore the time rate of change for salinity in box 1, due to air-sea exchange is:

$$\frac{\partial S_1^m}{\partial t} = \frac{1}{\tau}(S_1^* - S_1^m) = H_{S_1}^m, \tag{3.21}$$

In addition, the rate of salinity change caused by the exchange between box n with side boundaries m and/or box 2, can be calculated as:

$$\frac{\partial S_n^m}{\partial t} = \frac{|Q_{nm}|(S_m - S_n)}{V_n}. \tag{3.22}$$

Therefore the time rate of salinity change for box 1 is:

$$\frac{\partial S_1^m}{\partial t} = H_{S_1}^m + \frac{|Q_{1m}|(S_m - S_1)}{V_1}. \tag{3.23}$$

In the box model, the temperature and salinity of box 1 are calculated using (3.13) and (3.20), and of box 2/3 using (3.15) and (3.22). The equations are solved by the Runge-Kutt[a] 4th order method.

3.1.2 The Experimental Plan for the Box Model

Before further introduction of the detail of the plans, here will first be addressed the reason behind the design. At the conclusion of chapter 2, the water sources of the Indonesian Seas showed a significant variation with ENSO on the seasonal scale. Furthermore, the water sources - the North and South Pacific - supply water with very different properties to the ITF. Therefore, the water supply characteristics are investigated first, as the hypothesis behind the box model is that the cause of the Banda Sea anomalies is linked to changes in the supply of water from the Pacific.

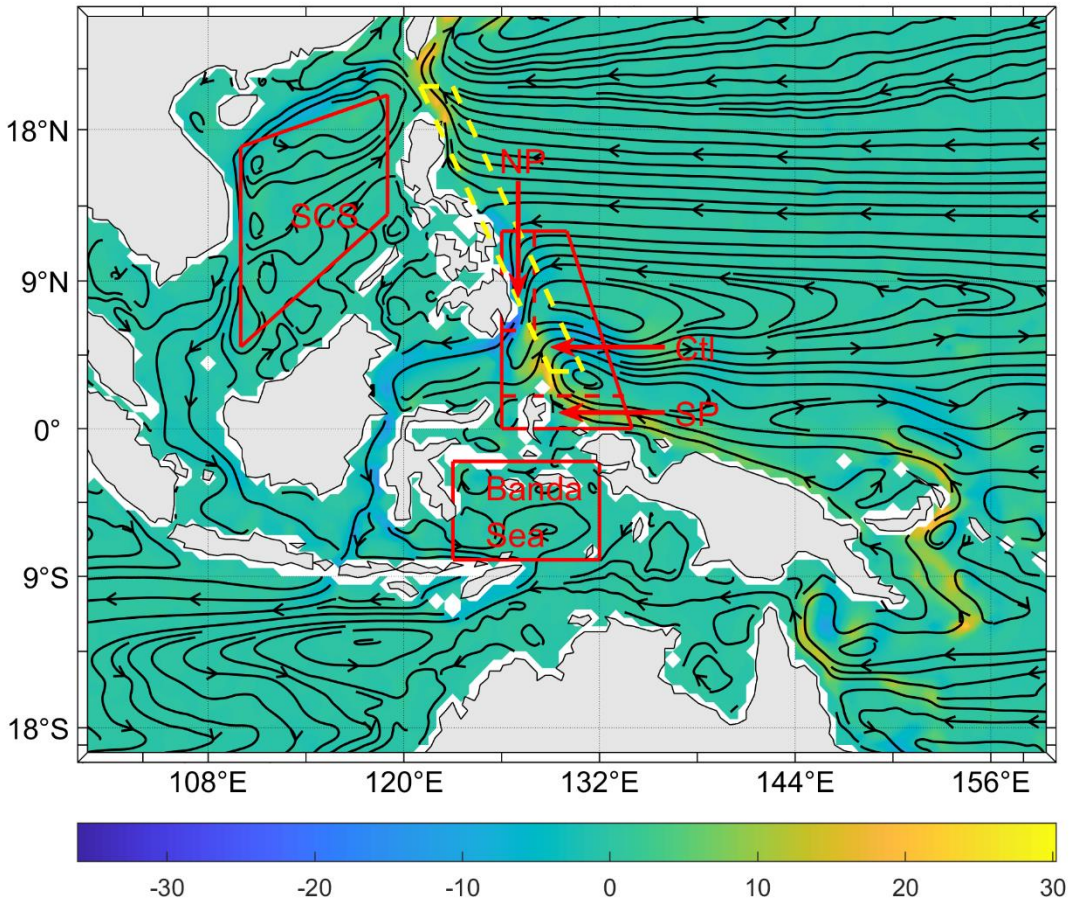

Figure 3.2 The averaged area for the Pacific side boundary of Ctl (control), NP (North Pacific), SP (South Pacific) and SCS (South China Sea) runs (in red boxes), and the area of the Philippine Trench for fig 3.3. The contour is the long term all-level vertical

averaged transport calculated from SODA, northward transport in positive and versa vice, unit: Sv.

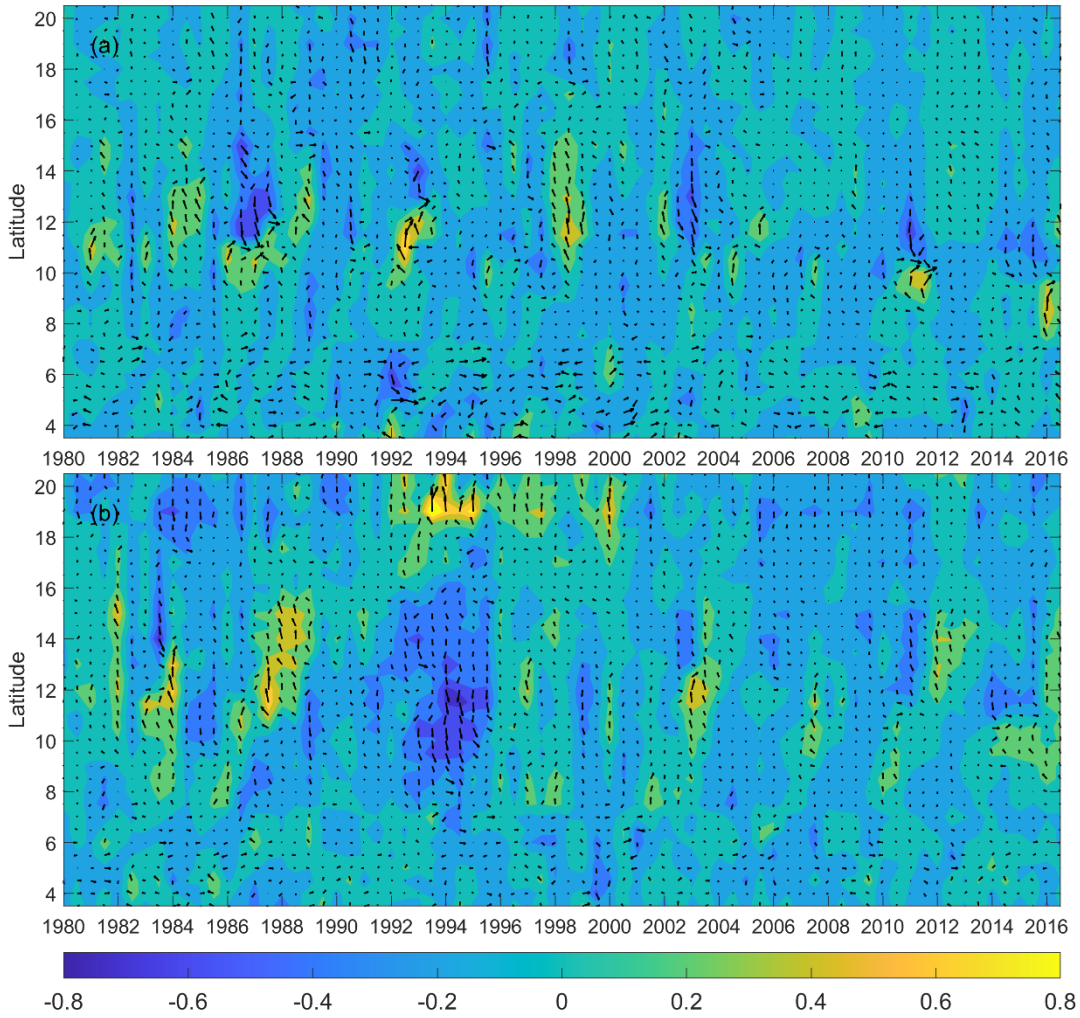

Figure 3.3 The propagation of the horizontal averaged perturbed transport along the Philippine Trench from SODA dataset, shown in fig. 3.2, during 1980 to 2016. The a and b indicate the anomalies in layers 2 and 3 respectively. The time step is every 6 months. The positive value suggests northward bias and the negative means southward bias, and the unit is Sv.

Fig 3.2 shows the topography of the Philippine Sea, and the yellow dashed box here indicates the Philippine Trench, which has a length of approximately 1320 km and is the third deepest ocean trench in the world. The Mindanao Current (MC) feeds fresh and cold water

from the North Pacific to the ITF over the Philippine Trench. Therefore, to investigate the variation of its water supply, the propagation of the horizontal averaged anomalous MC transport is presented in different layers in fig 3.3. There is mostly a regular annual variation in the propagation within layer 1, so fig. 3.3 only presents the flow anomaly in layers 2 and 3. In fig 3.3.a, at around 12°N, there is a roughly 2 year cycle of north-south oscillation in layer 2. In this layer, the largest such northward bias occurred in 1985, 1992 and 1999. The strongest southward bias appeared at this latitude in 1987 and a smaller one in 2003. In addition at around 6°N, a significant southward anomaly is found in 1992. There is not a very clear precursor for the onset of the anomaly seen in the transport of the Banda Sea during 1993 to 2000, which was the period of ENSO phases altering in high frequency (fig 2.3). For the layer 3 (fig 3.3.b), the most significant transport bias is the very strong southward bias during 1992 to 1996 in the 8° to 18°N band. This suggests that there was more water supplied to the ITF during 1992 to 1996, which may be a precursor for the Banda Sea anomaly.

The experiments are designed in two groups: a control run and sensitivity runs. Each experiment is run for 30 years, every simulating year is 365 days, and the time step is 100 seconds. For the control run (Ctl run), the Pacific side boundary input data, P_1, $P_2$and P_3 (see fig.3.1), are area averaged as shown in fig.3.2. This area includes both the Mindanao Current and the New Guinea Coastal Current (NGCC). The sensitivity runs are designed to test the effects of different water sources on the Banda Sea. Thus, the sensitivity runs are constructed with 3 options: the North Pacific run (NP), the South Pacific run (SP) and the South China Sea run (SCS). In this way, instead of changing the ratio of inflow water source structure, the sensitivity runs adjust the side boundary input to be composed of just one pure source. The Pacific side boundary input data for all the sensitivity runs are area averaged as indicated in fig 3.2. In sensitivity runs, the first 5 years of each simulation used the Ctl run side boundary input data, but during the 6th to 15h year, the Pacific side boundary input data is replaced by

different pure sources. From the 16th year, the side boundary input changes back to the Ctl run format.

Table 3.3 The temperatures and salinities of the Pacific side boundary input in all runs, data: SODA.

Parameters	Runs	T_{P1}(℃)	T_{P2}(℃)	T_{P3}(℃)	S_{P1}(psu)	S_{P2}(psu)	S_{P3}(psu)
Values	Ctl	21.6549	5.7138	1.9966	34.5561	34.5552	34.639
	NP	22.0138	5.5870	1.9856	34.5351	34.509	34.6378
	SP	22.4817	6.1059	2.0368	34.6486	34.6001	34.6419
	SCS	20.0584	6.1300	2.3181	34.2160	34.5025	34.6178

3.2 Model Results

3.2.1 Control Simulation Result

The modelled temperature and salinity of the Ctl run are presented in fig 3.4. They are fairly stable, with only a slight drift in the properties of box 3. The average modelled temperature for box 1, 2 and 3 are 21.26 ℃, 6.04 ℃ and 2.37℃ respectively, consistent with the long-term climatological temperatures based on the SODA dataset (see table 3.4). The mean simulated salinity for each box are 34.3 psu, 34.6 psu and 34.62 psu respectively; these also agree with the climatological salinity over the Banda Sea. The simulation of the fluxes for the Ctl run are presented in fig 3.5. It is to be noted that, unlike the convention in chapter 2, the direction of the transport is counter-geographical for horizontal transport, with southward transport being positive and northward transport negative. In the case of vertical transport, downwards is positive and upwards is negative. For the Pacific side boundary input fluxes, the value of the P_1, P_2 and P_3 are 0.32 Sv, -0.01 Sv and 0.032 Sv, all consistent with Table 3.2; the Q_{12} and Q_{23} in the Ctl run are -0.0196 Sv and -0.0663 Sv so upward in both boxes; for the outflow fluxes, I_1, I_2 and I_3 are 0.77 Sv, -0.037 Sv and -0.063 Sv respectively, so there is only outflow to the Indian Ocean from box 1 and weak inflow from the other two

boxes. Except for P_3, the Ctl run successfully simulated all fluxes (comparing with table 3.2). Because the Lifamatola Strait is in reality shallower than the depth of box 3, the water is well mixed before entering the Banda Sea, which is not included in the box model. Therefore generally, the box model is considered to successfully simulate the horizontal transport in each box. In the Ctl run, box 1 fluxes reached equilibrium within the first 3 years. The horizontal flow is the main process in each box. Due to the relatively small vertical fluxes (Q_{12} and Q_{23}), the inflow from the Pacific and the outflow to the IO are close to each other in all three boxes. For box 2, the P_2 and I_2 present a strengthening trend in northward transport, the P_2 and I_2 increased from ~-0.02 Sv and 0.02 Sv to ~0 Sv and ~0.05 Sv. In box 3, the P_3 shows a stable trend but the I_3 and Q_{23} decreased from ~-0.057Sv and ~-0.06 Sv to ~-0.07 Sv both during 30 years simulation. The variation trends of box 2 and 3 might not be ideal, but acceptable as a simple physical basin model.

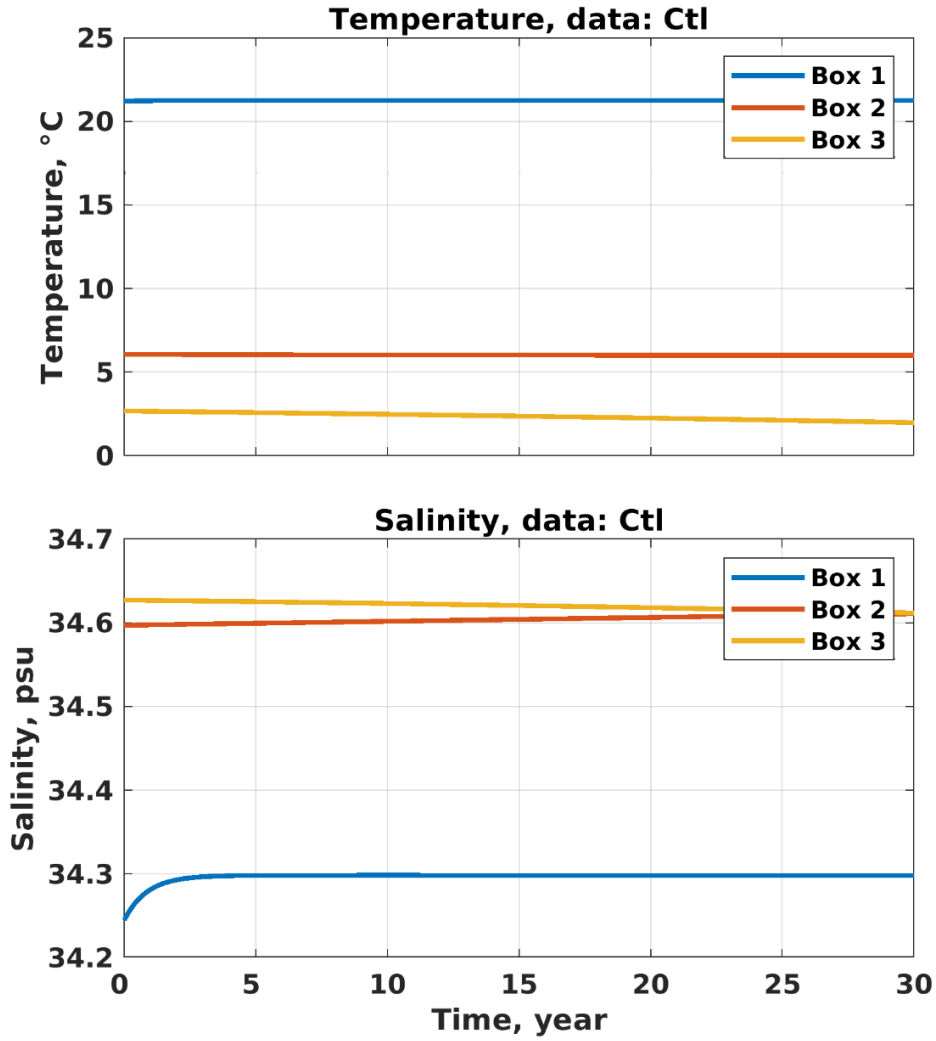

Figure 3.4 The modelled temperature and salinity of the Ctl run.

Table 3.4 The water properties of each box from the SODA dataset and Ctl run.

Data	T_1, ℃	T_2, ℃	T_3, ℃	S_1, psu	S_2, psu	S_3, psu
SODA	21.23	6.07	2.69	34.24	34.60	34.63
Ctl	21.26	6.04	2.37	34.30	34.60	34.62

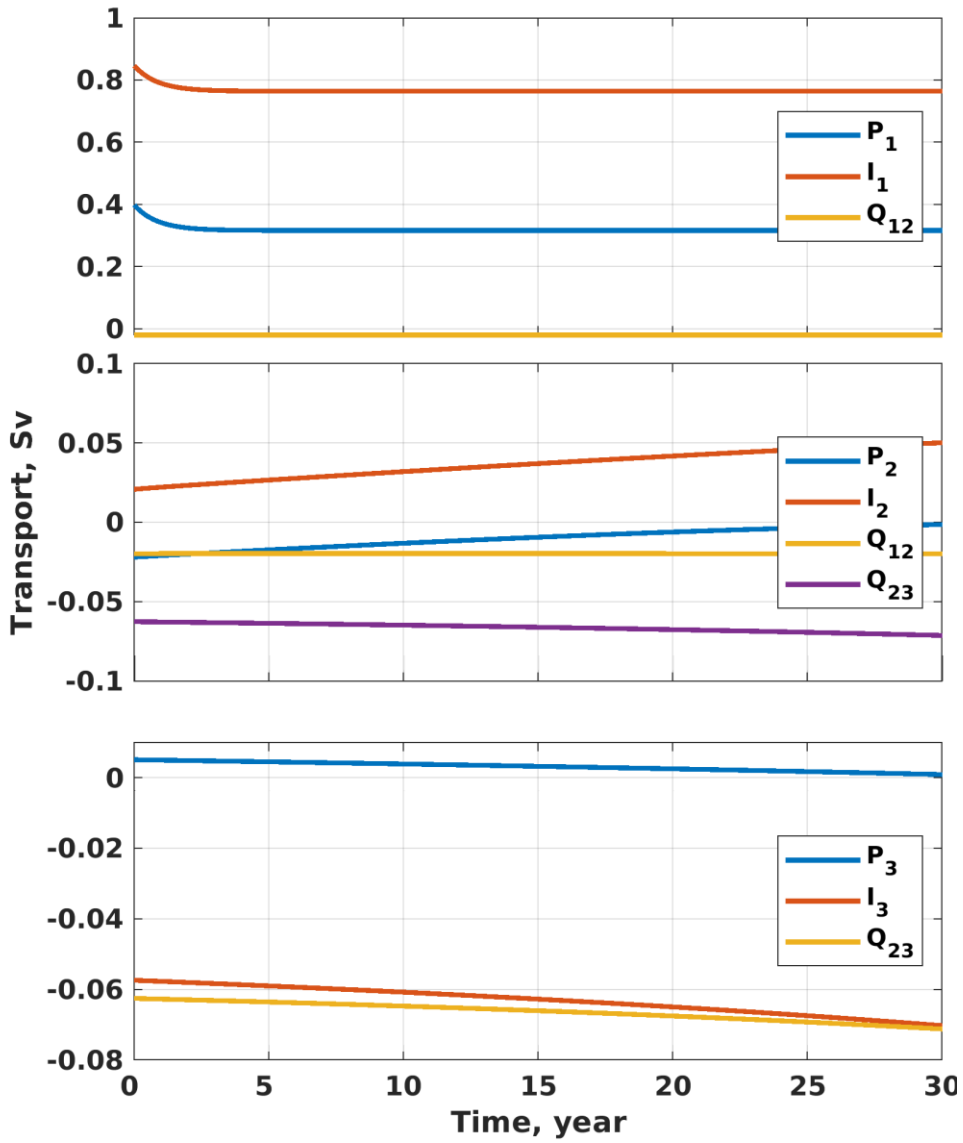

Figure 3.5 The modelled transport of the CTL run. For the horizontal transport, Ps and Is, the southward transport is in positive, and the northward transport in negative; for vertical transport,Q_{12} and Q_{23}, the positive value means downward transport, and the negative means upward transport. The sign of the transport value representatives the same direction in following this chapter.

3.2.2 Sensitive Simulations Result

The sensitivity runs examining different water sources are next compared. (see table 3.3 for input T and S). For box 1, the difference of temperature, salinity and transport

between the Ctl run and the sensitivity runs are presented in fig 3.6. After the input into the Pacific side boundary changes in year 5, all supplying water experiments tends to decrease the Banda Sea temperature in layer 1. The North Pacific water cools the box 1 the most, by $\sim 6.87 \times 10^{-4}$ ℃, the South Pacific second by lowest to $\sim 4.82 \times 10^{-4}$ ℃, and the SCS water cools the box 1 down about 3.09×10^{-4} ℃ also but all of the temperature anomalies changed back to near zero after the perturbation stopped. The average temperature anomalies during and after the perturbation inputting (year 6 to 15) are listed in table 3.5. In the case of salinity variation, all sensitive runs present a freshening effect on box 1, the NP decreased the salinity to about 0.012 psu, the SP decreased about 0.008 psu and about 0.005 for the SCS, in 5 years and reached balance before the anomalous input ends. Similar to the case for temperature, the disturbance of salinity trends to disappear after year 15 rapidly, and reach balance again at about year 20. The overall box 1 perturbed transport present a negative bias for all sensitivity runs, the lowest values happening immediately the anomaly started, reaching -0.3 Sv, -0.22 Sv and -0.14 Sv, for the NP, SP and SCS runs respectively. These levels are then maintained throughout the inputting period. The maximum transport anomalies appear when the imposed anomaly ceases, and the anomalies reach equilibrium within three years.

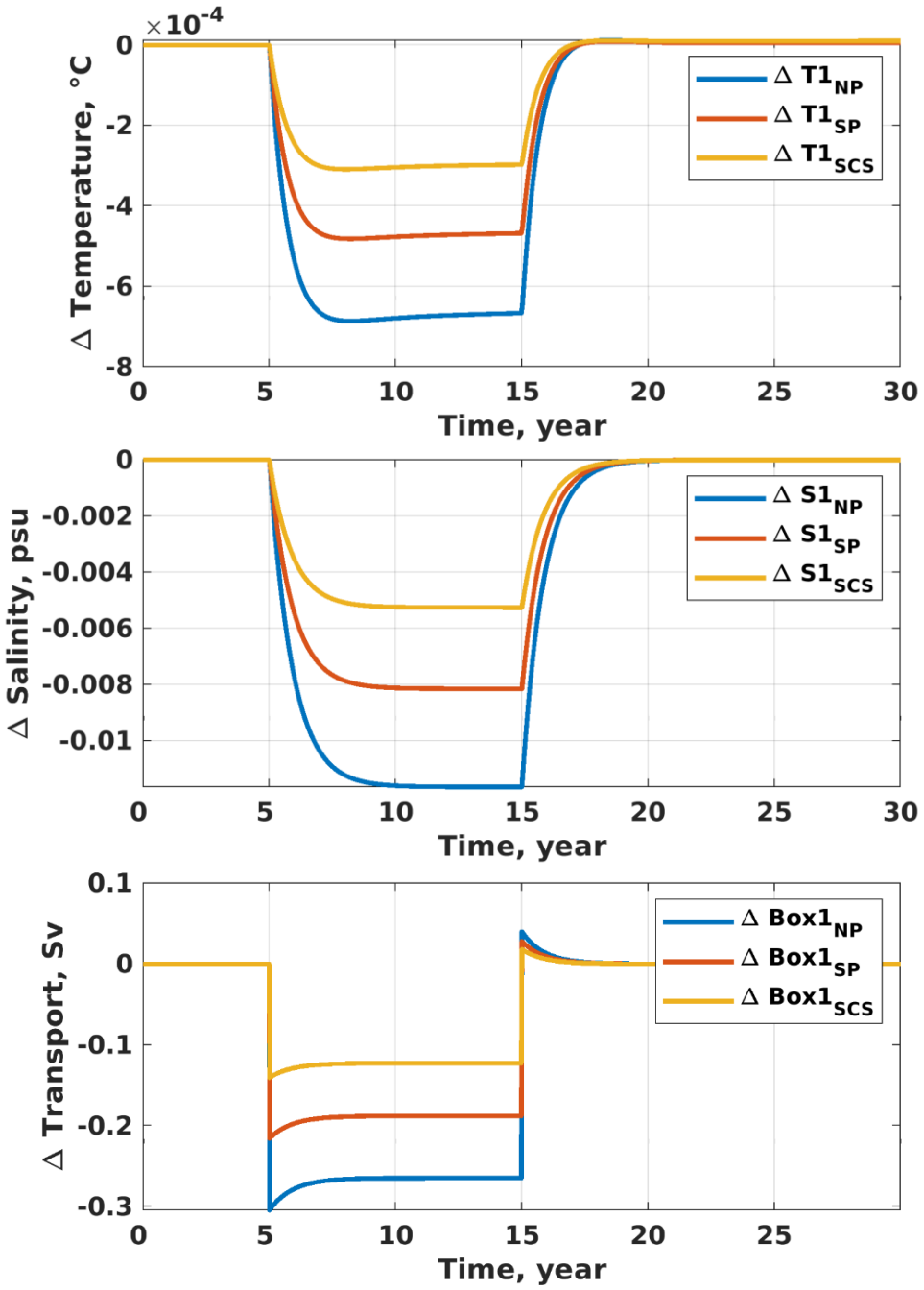

Figure 3.6 The anomaly of temperature, salinity and transport between the Ctl run and sensitive runs in box 1.

The sensitivity runs examining different water sources are next compared. (see table 3.3 for input T and S). For box 1, the difference of temperature, salinity and transport between the Ctl run and the sensitivity runs are presented in fig 3.6. After the input into the Pacific side boundary changes in year 5, all supplying water experiments tends to decrease

the Banda Sea temperature in layer 1. The North Pacific water cools the box 1 the most, by $\sim 6.87 \times 10^{-4}$ ℃, the South Pacific second by lowest to $\sim 4.82 \times 10^{-4}$ ℃, and the SCS water cools the box 1 down about 3.09×10^{-4} ℃ also but all of the temperature anomalies changed back to near zero after the perturbation stopped. The average temperature anomalies during and after the perturbation inputting (year 6 to 15) are listed in table 3.5. In the case of salinity variation, all sensitive runs present a freshening effect on box 1, the NP decreased the salinity to about 0.012 psu, the SP decreased about 0.008 psu and about 0.005 for the SCS, in 5 years and reached balance before the anomalous input ends. Similar to the case for temperature, the disturbance of salinity trends to disappear after year 15 rapidly, and reach balance again at about year 20. The overall box 1 perturbed transport present a negative bias for all sensitivity runs, the lowest values happening immediately the anomaly started, reaching -0.3 Sv, -0.22 Sv and -0.14 Sv, for the NP, SP and SCS runs respectively. These levels are then maintained throughout the inputting period. The maximum transport anomalies appear when the imposed anomaly ceases, and the anomalies reach equilibrium within three years.

Table 3.5 The temperature and salinity anomaly between the Ctl and sensitive runs in box 1 during and after perturbation inputting.

Parameters	NP	SP	CSC
Mean ΔT_1 (yr 6-15; 10^{-4} ℃)	-6.35	-4.46	-2.85
Mean ΔT_1 (yr > 15; 10^{-5} ℃)	-1.98	-1.34	-0.28
Mean ΔS_1 (yr 6-15; psu)	-0.01	-0.01	-0.01
Mean ΔS_1 (yr > 15; $10^{-4}\ psu$)	-6.72	-4.71	-3.08

In box 2 (fig 3.7), all three runs warm the Banda Sea to a greater extent than is the case for box 1. Unlike in box 1, this temperature variation continued throughout years 6 to 15 and had only a slight cooling tendency after the imposed input anomaly ceased after year 15. At the end of year 15, the temperature anomalies reached a maximum as 1.65×10^{-4} ℃, 4.66×10^{-4} ℃ and 0.0032 ℃ for the NP, SP and SCS runs respectively. After the

perturbation was removed, all the temperature anomalies decreased with time but remained high at the end of simulation, with the value of each being 7.13×10^{-6} ℃, 3.1×10^{-4} ℃ and 0.0025 ℃ respectively. For salinity variation, the SCS water supplement increased the box 2 salinity about 0.0017 psu during the perturbation with this being only slightly decreased to 0.0016 psu by the end of the simulation; the NP and SP runs presented a similar increasing pattern but to smaller values, 4.05×10^{-4} psu and 4.59×10^{-4} psu at the end of the perturbation, and 3.95×10^{-4} psu and 4.41×10^{-4} psu at the end of simulation. The average temperature and salinity anomalies during and after the perturbation are listed in table 3.6. With respect to the transport, the replacement of the input with SCS water decreased the transport tremendously by approximately 0.24 Sv during the disturbance ($P_2 = -0.01$ Sv in Ctl run); the NP and SP runs also show a decreasing effect on box 2 transport, but of less a quarter the size of that in the SCS run. After changing the input data back to the Ctl plan, the anomalous transport of the NP, SP and SCS runs reduced to near 0 Sv immediately

Table 3.6 The temperature and salinity anomaly between the Ctl and sensitive runs in box 2 during and after perturbation inputting

Parameters	NP	SP	CSC
Mean ΔT_2 (yr 6-15; 10^{-5} ℃)	7.2720	20.9880	146.6111
Mean ΔT_2 (yr > 15; 10^{-5}℃)	7.0018	37.8670	287.2037
Mean ΔS_2 (yr 6-15; 10^{-4} psu)	2.0693	2.3761	9.3372
Mean ΔS_2 (yr > 15; 10^{-4} psu)	4.0477	4.5101	16.9984

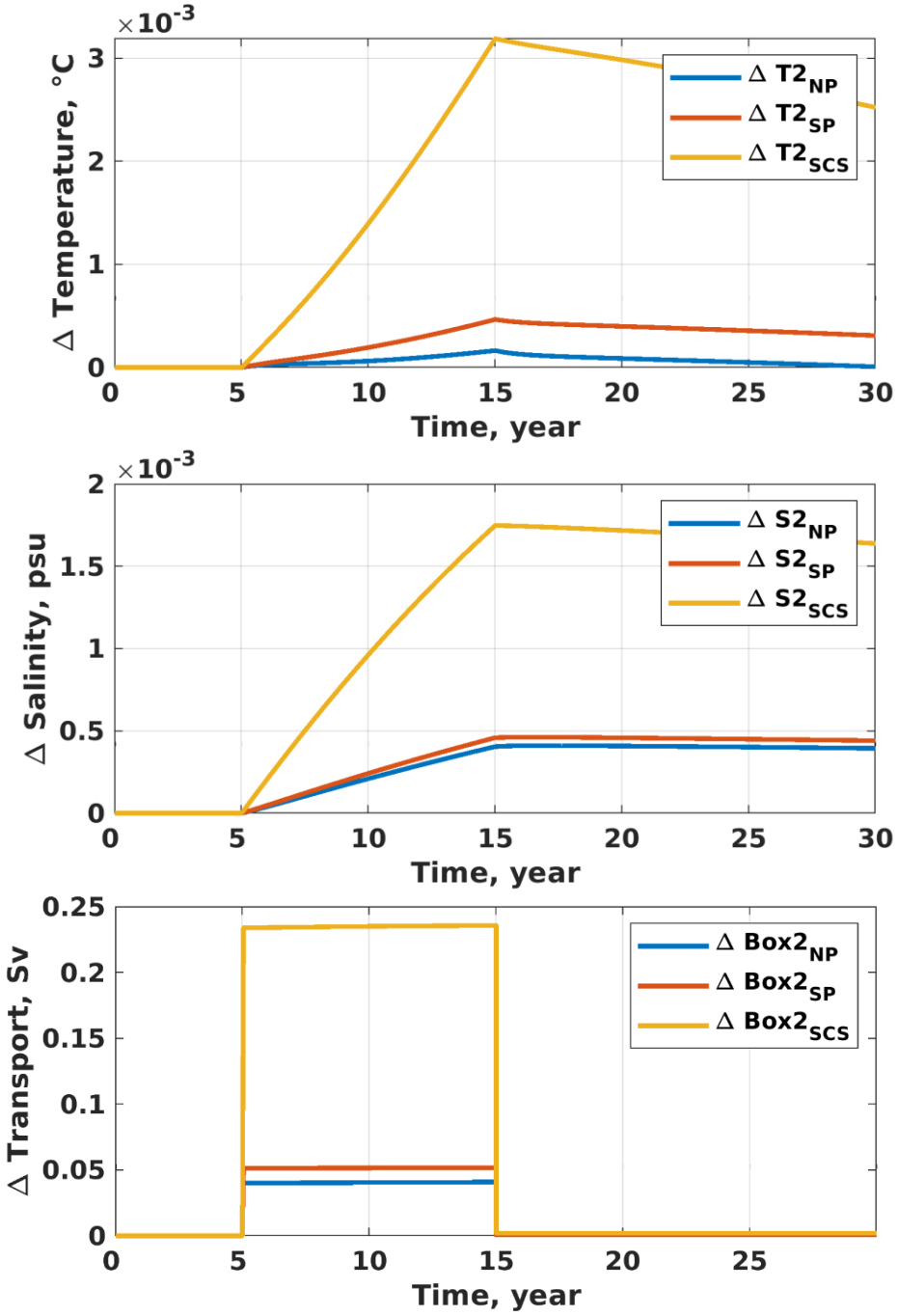

Figure 3.7 The perturbed temperature, salinity and transport between the Ctl run and sensitive runs in the box 2.

In fig 3.8, the sensitivity results for box 3 are shown. The deviations of temperature are positive for all the runs. The perturbed temperature between the Ctl and SCS is much bigger than the anomalies with NP and SP inputs. For the SCS run, the rate of increase became slower after the disturbance input ceased but remaining positive, and reached a

maximum when the simulation ended. All sensitivity tests showed continued temperature rise in box 3 after the anomaly was removed. For salinity, the SCS water freshened box 3 the most comparing with the other 2 runs, the freshening anomaly reaching 4.44×10^{-4} psu by the end of the run. The South Pacific run freshened box 3 also, but by less (minimum: -2.77×10^{-5} psu). The North Pacific water increased the salinity in box 3, marginally, by about 2.69×10^{-6} psu at the maximum. When the Pacific side input data switched back to the Ctl plan, all salinity differences kept their tendency and arrived at their maximum at the end of the simulations. The box 3 temperature and salinity differences of the Ctl run compared to the sensitivity runs are shown in table 3.7. Fig. 3.8 also shows the horizontal transport responses of the sensitivity runs. For the horizontal transport, the SCS run presented a strong northward transport bias, the peak appeared at the beginning of perturbation (~ -0.0059 Sv), reduced only slightly during the perturbation period (to -0.0057 Sv). After the perturbation ceased transport changed to a slight southward bias (~ 2.83×10^{-4}Sv). The SP run showed a slight northward transport anomaly (mean: -3.14×10^{-4}Sv) during the imposition of the anomaly, with this almost returning to Ctl values after the input anomaly ceased. In the case of the NP water experiment box 3 transport saw slightly more water moving to the south (7.43×10^{-5}Sv averagely) during the anomaly phase, and this tendency remained after the anomaly ceased ($\sim 4.11 \times 10^{-5}$Sv).

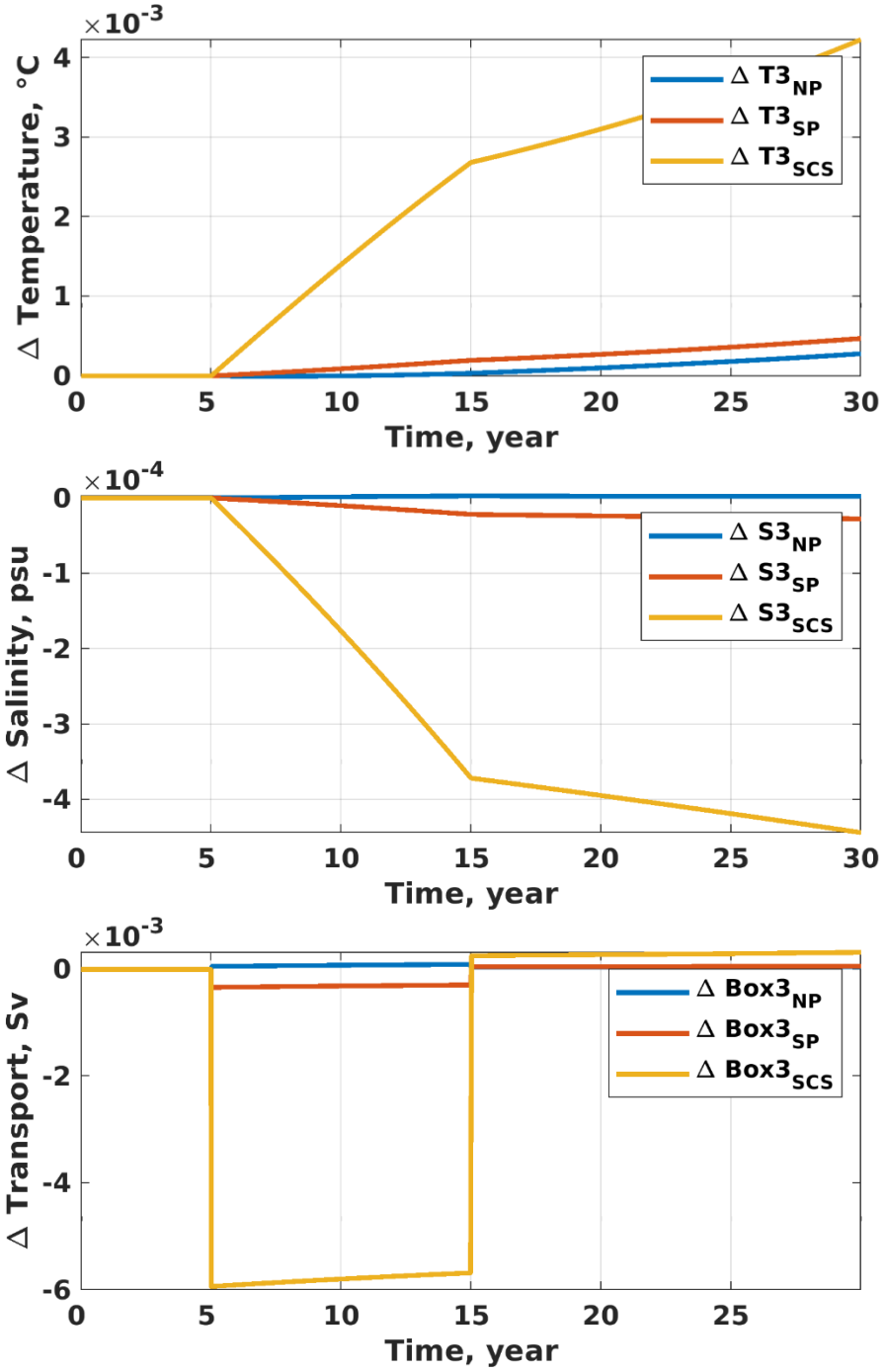

Figure 3.8 The perturbed temperature, salinity and transport between the Ctl run and sensitive runs in the box 3.

Table 3.7 The temperature and salinity anomaly between the Ctl and sensitive runs in box 3 during and after perturbation inputting.

Parameters	NP	SP	CSC
Mean ΔT_3 (yr 6-15; 10^{-5} ℃)	0.62	9.29	138.03
Mean ΔT_3 (yr > 15; 10^{-4} ℃)	1.45	3.21	33.81
Mean ΔS_3 (yr 6-15; 10^{-5} psu)	0.14	-1.05	-17.97
Mean ΔS_3 (yr > 15; 10^{-5} psu)	0.21	-2.48	-40.70

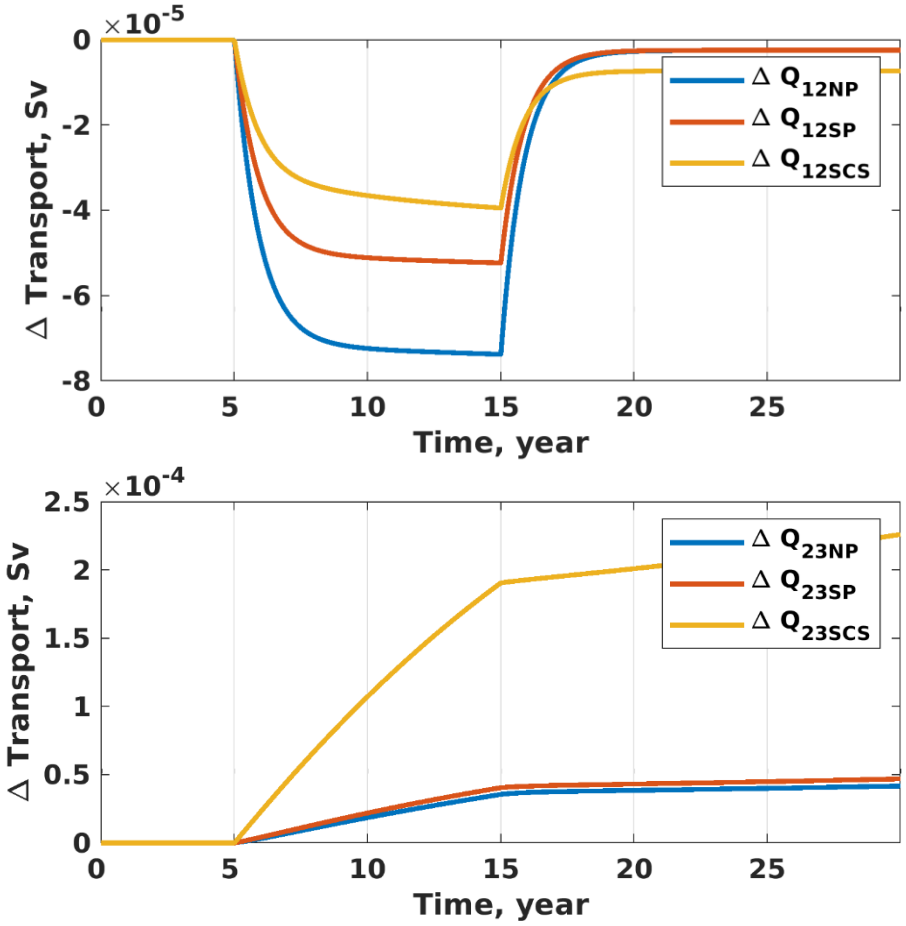

Figure 3.9 The perturbed vertical transport between the Ctl run and sensitive runs, unit: Sv.

Fig 3.9 shows the vertical transport difference of Q_{12} and Q_{23} between the Ctl and sensitivity runs. For Q_{12}, all three sensitivity runs trend to strengthen the downward transport. During the anomalous input stage, all three runs increased the transport quickly during the first 3 years, but with the rate of increase slowing thereafter. These increasing trends stopped immediately after the anomalies ceased, decreasing over about 3 years but then remaining

slightly negative for the rest of the simulation. For Q_{23}, unlike the Q_{12}, all three anomalies are positive which mean these sensitivity runs weakened the upward transport. During the inputting period, the NP and SP show a small weakening bias; the SCS run decreased the Q_{23} most with a stronger trend. After the inputting end, all three variations maintained the upward bias, but with a much slower increasing rate.

3.3 Discussion and Conclusions

It is the very first time that the shift of the vertical structure of the horizontal transport at the Banda Sea be found, which is introduced in Chapter 2, and the three-layer structure is consistent with the modelling result also (Liang et al., 2019). This modelling research suggests that each layer has different water properties, and the water source is different too. Therefore, it is assumed that the ratio change of water from different sources causes the structure shift. The box model simulating plans are designed based on this hypothesis.

For the Ctl results, the simulation is reasonably realistic. The layer 1 transport reached equilibrium within the first 3 years and maintained this throughout the simulation. However, in box 2, the P_2 and I_2roughly stabilised in the first 10 years, but continued strengthening afterwards. Moreover, in box 3, the P_3 and I_3 present a negative flux trend during the whole simulation. The reason of the unstable variation in the box 2 and 3 might be because the box volume is too small comparing with the strong input fluxes but the stability has been improved after k values adjustment (compare fig. 3.5 with Appendix fig S7-8). On the other hand, the Banda Sea is highly affected by Ekman pumping (Potemra, 1999; Gordon and Susanto, 2001; Horhoruw et al., 2017). However, the box model only allows the ocean to interact with atmosphere by freshwater and heat fluxes exchange. Without a proper wind field applied to box1, it is impossible for the box model to simulate the Ekman pumping effectively. Thus, the vertical transport between boxes was simulated poorly.

Although the results of differences of the control and sensitivity runs are extremely small, but it is enough to support the hypothesis qualitatively. Comparing the box model results with fig 2.5 and 2.6, the possible reason for the transport vertical shift during 1993 to 2000 might be that there was a relatively short surge from the SCS or the South Pacific to the Banda Sea into layer 3. Therefore, after this surge, layer 3 had more water transported to the south and in layer 2, not only there was more water transport to the north, but also more water flowed vertically into this layer from both layers 1 and 3.

To verify the box model results and the hypothesis, the annal volume transport via the Mindoro Strait, the Lifamatola Strait and the Makassar Strait are calculated. The Mindoro Strait connects the South China Sea and the Sulu Sea. Although, the South China Sea supplies the Banda Sea through both the Karimata Strait and the Mindoro Strait, the depth of the Java Sea limits the deep transport ability. Thus, the Mindoro Strait represents the effective transport from the South China Sea to the Banda Sea, the Lifamatola Strait provides the South Pacific water source route and the Makassar Strait that for the North Pacific water. Fig 3.10 presents the annual transport variance via the Mindoro Strait, the Lifamatola Strait, and the Makassar Strait in layer 3. In 1993, the Mindoro Strait fed more water at the layer 3, but the transport decreased to positive transport variance until 1996. For the Lifamatola Strait, more water flowed into the Banda Sea during 1993 to 2000. Although, the box model results suggest that the box 3 transport is more sensitive with the SCS run, the Ctl run water source is composed of a mixture of the North and South Pacific water, which naturally suggests the observed behaviour would be closer to the NP and SP sensitivity runs. Therefore, more water flowing into the deep Banda Sea during 1993 to 2000 from the South Pacific is most likely to be the cause of the transport's vertical distribution shift found in Chapter 2 during the same time.

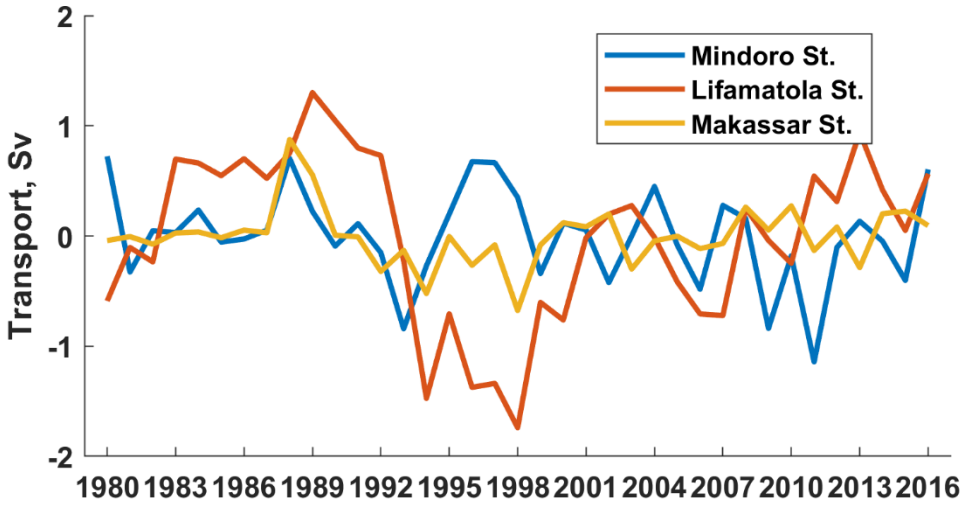

Figure 3.10 The annual transport variance series via the Mindoro Strait, the Lifamatola Strait, and the Makassar Strait in layer 3 calculated from the SODA data, the positive means northward vice versa, unit: Sv.

Chapter 4 The Palaeoclimate FRUGAL Model Simulation

In this thesis, to explore the role of the ITF in palaeoclimate, an ocean-atmosphere coupled model, the FRUGAL model (fine resolution Greenland Sea and Labrador Sea model; Wadley and Bigg, 2002), has been used for simulating aspects of the global climate since the Last Glacial Maximum (LGM). The first part in this chapter will introduce the previous palaeoceanography research focused on the ITF and nearby area. The part 4.2 will introduce the FRUGAL model and the design of the simulation plans. The control run results will be discussed in part 4.3.

4.1 The Introduction of the ITF Palaeoclimate Research

The prevailing research scope in the ITF palaeoceanography is hydrological data reconstruction, such as sea temperature and salinity, from ocean cores, combined with numerical modelling. Utilizing the ocean cores, the hydrological characters, such as sea temperature and salinity, are reconstructed, and the variations of those variable are presented over different time periods for different basins and channels within the Indonesian Seas (Hendrizan et al., 2017; Zhang et al., 2018; Schröder et al., 2016), and the nearby area in the Pacific and Indian Ocean (Xu et al., 2017; Rippert et al., 2015; Linsley et al., 2017). Because of its role in the global thermohaline circulation, the ITF not only affects the local and nearby area, but the whole globe. Comparing the ocean cores from the west Equatorial Pacific, east Indian Ocean and North Atlantic, the reduced ITF transport during the MIS M2 (~3.3 Ma BP) contributed to the Southern Hemisphere climate cooling through reduced tropic-pole heat transfer (De Vleeschouwer et al., 2018), and the eastern subtropical Indian Ocean and the Mediterranean outflow (Sarnthein et al., 2018). Although the ocean cores recorded the reality, the reconstruction data based on it only can offer basic hydrological variables and even for the high-resolution core data, the time resolution is at best about 100 years (Hendrizan et al.,

2017) at a specific location. Therefore, the temporary and spatial resolution, and narrowed variable options limit the ocean core reconstruction data for more detailed and comprehensive studies. In palaeo background, the ITF were reduced due to the sea level change or tectonic movements (Cane and Molnar, 2001; Kuhnt et al., 2004; Petukhova et al., 2010), however, this reduction is less quantified. Here are the modelling studies that quantified the difference in different periods. Modelling results show that due to the topography difference at the Early Pliocene, the transport of the ITF was 1.7 Sv smaller than for present-day bathymetry and caused Indian Ocean cooling of 1 ℃ (Krebs et al., 2011). Comparing the LGM to present, the ITF transport was decreased about 1.5 to 5 Sv due to the sea level was ~120 m lower (Di Nezio et al., 2016; Kuhnt et al., 2004; Shin et al., 2003; Bigg and Wadley, 2001;). Therefore, the current researches have focused on the variability of the ITF itself over different timescales, its relationship with the Indian Ocean and the Pacific, and teleconnection with the Atlantic and the Antarctic. Most of these analyses focused on examining the hydrological situation in different geological periods by using the ocean core evidence. Most palaeocean modelling researches which mentioned the ITF, focus on the global scale and highlighting the popular currents/regions, as the AMOC and the Southern Ocean, instead of the ITF itself (Okazaki et al., 2010; Yu et al., 2004; Menviel et al., 2011; Kim et al., 2002; Liu et al., 2002; Paul et al., 2010). For the very a few palaeocean modelling studies that aim at the ITF, the discussion has focuses on the ITF pathway differences between palaeo and nowadays from Pleistocene to LGM (Cane and Molnar, 2001; Di Nezio et al., 2016). The global effects of the ITF is still uncertain under the LGM deglacial process, and modelling seems the best approach to investigate it.

In this research, the first aim is to use the FRUGAL model (Wadley and Bigg, 2002) to run a global simulation under the LGM condition. As an intermediate complexity climate model, FRUGAL has a simple atmosphere layer which allows air-sea interactions with the

more complex ocean component but efficiently. The second purpose in this study is to discern what effect the insolation variation plays during the deglacial process, particularly on the role of the ITF. The last aim is studying the local and global effects of the ITF connection under the paleo background.

4.2 The Introduction of FRUGAL

The FRUGAL was developed from the Southampton-East Anglia ocean general circulation model. This model has been used for various palaeoclimate studies, including for the LGM (Bigg et al., 2012), the MIS 6 glaciation (Green et al., 2010) and the Early Pleistocene (Rea et al., 2018). Comparing with typical OGCMs (ocean general-circulation models), the North Pole in FRUGAL is moved to central Greenland rather than being in the Arctic within a similar orthogonal curvilinear grid (Wadley and Bigg, 2002), as shown in fig 4.1. That means there is a much finer zonal grid space in the North Atlantic and Arctic region. As the result of this grid change, the spatial resolution in the Northern North Atlantic is four times finer than in the Southern Hemisphere and North Pacific, and in the meridional direction the resolution in the equatorial region is increased. For efficient integration, the time step varies with local model resolution rather than being consistent with the finest grids (Wadley and Bigg 2002). In this study, the spatial resolution grid is 182 x 211 cells, which is equivalent to approximately 2° longitude by 1.5° latitude in the Southern Hemisphere and a resolution of 20 km around the Greenland coast.

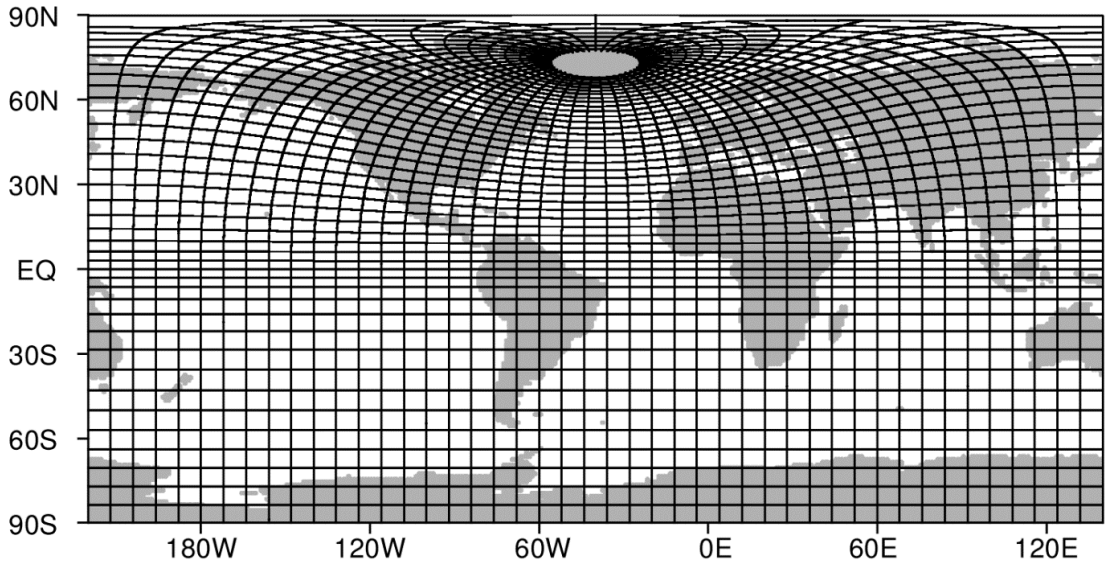

Figure 4.1 The FRUGAL grid projection, with the grid north pole in Greenland at 40.0°W, 72.5°N (Wadley and Bigg, 2002).

The FRUGAL climate model is composed of 19 layers of ocean and 1 layer of simple atmosphere to allow grid point by grid point air-sea interaction, as exchanges of heat, freshwater, and surface wind stress (Bigg and Wadley, 2001). The mixing of sea temperature and salinity follows the direction of the horizontal, vertical and isoneutral surfaces (Griffies et al., 1998), with the values of the mixing coefficients being taken from England (1993). More physical process formulation of the FRUGAL model is introduced in Wadley and Bigg (2002). Because this study focuses on palaeoclimate, the LGM topography used in FRUGAL is according to the ice-sheet topography (Peltier, 1994) which is 120 m lower sea level than the original topography.

The atmosphere in FRUGAL is a simple radiative-advective atmosphere, which is an adaptation of the energy and moisture balance model of the UViC Earth Systems Model (Fanning and Weaver, 1996) that allows for advection of water vapour. This includes thermodynamic sea-ice, which is advected by the surface ocean currents. Moreover, the atmosphere model includes parameterisations of clouds, mountains, land-ice, and land

hydrology. The wind stress varies monthly in simulations of this study, but has no feedback from the SST field.

In this work, there are four simulations, two are the LGM deglacial control runs (Ctl run), in which both of them have an open ITF but the Ctl 2 run enabled varying insolation during the whole simulation, which means that the Ctl 1 presents the nature variability in the FRUGAL and the Ctl 2 shows the deglacial processes; and another two are the LGM sensitivity runs (Sen run) with closed-ITF and without varying insolation (table 4.1). In the control simulations, the freshwater flux is allowed to flow from land into the ocean via the steepest gradient; for the basic conditions of the model simulations see Levine and Bigg (2008). The sensitivity runs are designed to study how the local and global climate respond to fully/semi closed Indonesian Seas during the deglacial process after the LGM. As fig 4.2 shows, for the Sen 1 run, the bathymetry value is raised for all the grids within the Indonesian area to the surface and in the Sen 2, the grids within the area whose depth is between 0 to 2 levels (surface to 30 m deep) is decreased by 1 depth level. However, although in Sen 2, after editing the bathymetry there are grids still under the sea surface in the Indonesian Seas, all the channels of inflows remained cut in the model.

Table 4.1 the FRUGAL simulations design.

Runs	Simulation time	ITF connection	Insolation varying
Ctl1	21 ka	Open	No
Ctl2	21 ka	Open	Yes
Sen1	6ka	Closed	No
Sen2	6ka	Semi-closed	No

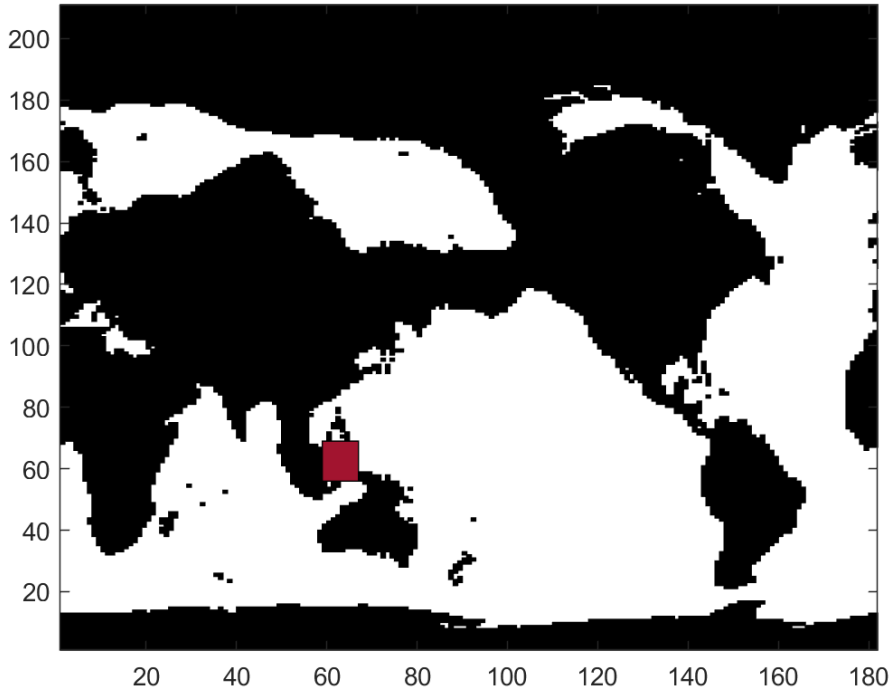

Figure 4.2 The global bathymetry in the LGM FRUGAL simulation. The Ctl run used the black bathymetry. In Sen runs, the ITF is blocked by raising the seabed to the sea surface in the red area.

4.3 The Ctl 1 Simulation Results Analysis

To verify the model's reliability, the FRUGAL Ctl simulation result is compared with the Last Glacial Maximum Reanalysis (LGMR; Osman et al., 2021). The LGMR is a global gridded palaeoclimate dataset which combined proxy and independent model results for the past 24 ka. To more easily compare with the FRUGAL simulations, here only the past 18 ka of the LGMR data is used (fig 4.3). Unlike the LGMR dataset, in the Ctl run, the orbital parameters are fixed, therefore here the comparison focuses on the values of the LGM. The mean global LGMR SST at the LGM is 12.54 ℃ and the initial, pre-spinup (first 3000 years), mean global Ctl 1 SST is 13.1 ℃. After the Ctl runs reached equilibrium at around 18 ka, both the Ctl 1 and 2 SST are stable but their mean SST reduces to 10.06 ℃, while the LGMR mean at that time is 15.26 ℃. Due to the fully cut inflows in Sen 2, the bathymetry change

actually is same with Sen 1. Therefore their global mean SST is same too. The global average for FRUGAL runs are calculated after the SST data is masked by topography. Because the FRUGAL only has one layer of atmosphere, and in Ctl 1 run, the insolation, surface winds and the land ice extent are not changed from one year to the next, as a result the model SST does not change much and is different from the LGMR, but the Ctl 1 and 2 are different from each other.

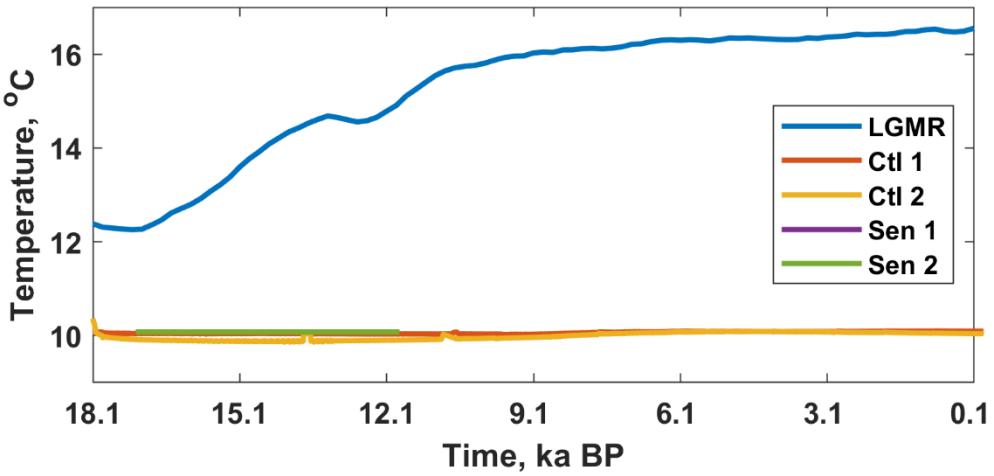

Figure 4.3 The surface sea temperature (SST) from the LGMR dataset and the FRUGAL simulations since 18 kyr BP.

In the Ctl run, to take into account the complex bathymetry change during the deglacial the model ITF is calculated as the volume difference between the volume transport along 105ºE between the Indonesian Seas and the Antarctica and that along 125ºE from Australia to the Antarctica, which is different from the present day calculation used in chapters 2 and 3. The Ctl simulations reached equilibrium after 3 ka, therefore all the following plots only show the fluxes after the spin-up, as fig 4.4.The ITF flux presents a strong annual variation and has a mild increasing trend overall but a decreasing trend for the last 1 ka. Between 18 ka to 0, the averaged ITF flux is 13.33 ± 3 Sv, the maximum is 21.4 Sv

and the minimum is 4.66 Sv; the ITF flux presents a strong annual cycle, the mean of annual maximum is 17.9 ± 1.6 Sv, the mean of annual minimum is 9 ± 1.8 Sv.

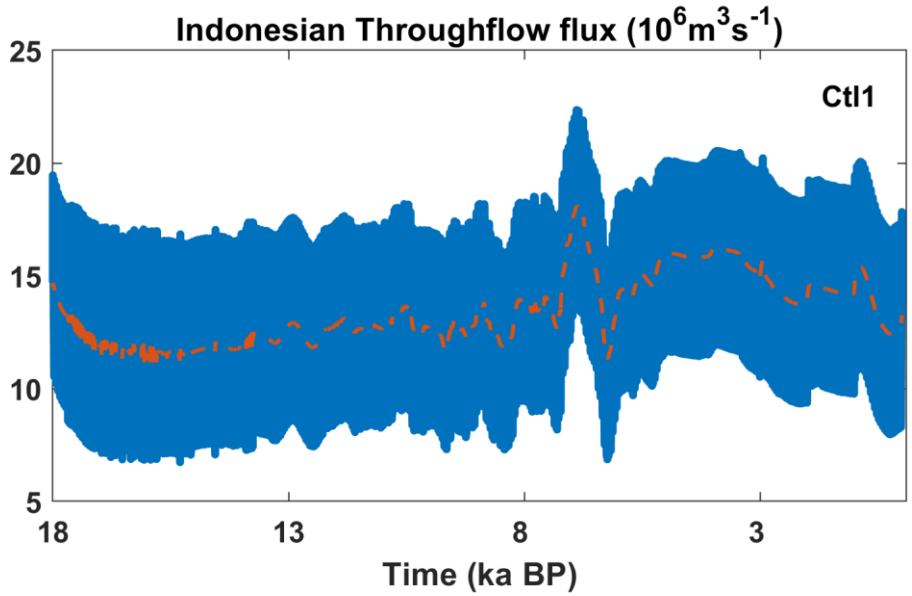

Fig 4.4 The ITF flux monthly variation in Ctl 1 simulation during 18 ka BP to 0. The decadal moving mean series is in orange dashed line, unit: Sv (10^6 m^3 s^{-1}).

Spectrum analysis, as the Fast Fourier Transform (FFT) is very helpful for a better understanding of the drive of the nature variability in different time scale. The power of the FFT of the ITF flux, shown in fig. 4.5, increases with the period, which indicates the variability of the ITF is time-independent. Additional, because of the model simulation is 18000 years long, the periods beyond 10000 years should be ignored.

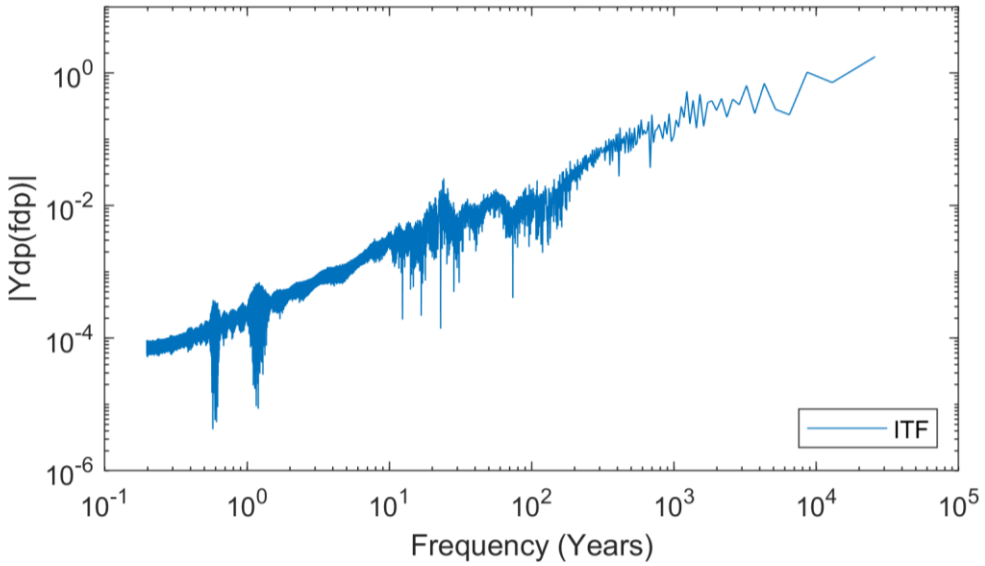

Figure 4.5 The Fast Fourier Transform result of the ITF flux between 18 ka BP to 0 from the Ctl 1 simulation.

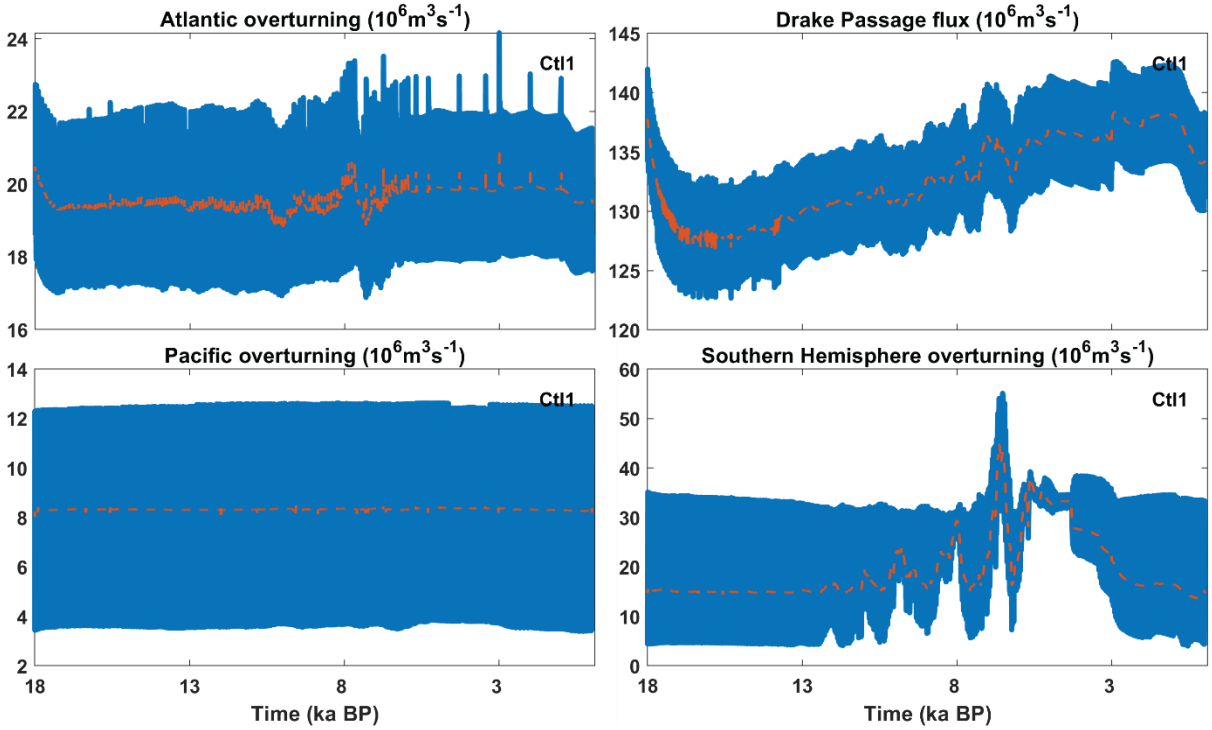

Fig 4.6 The fluxes monthly variation of thermohaline circulation members of the Ctl 1 simulation. The decadal moving mean is in orange dashed line, unit: Sv.

Because the ITF is linked to the global thermohaline circulation, fig 4.6 shows the key currents of the global thermohaline circulation since the spinup. In the global thermohaline

circulation, the water flows into the Indian Ocean from the Pacific via the ITF, then enters the South Atlantic through the Agulhas Current, goes north with the Atlantic Equatorial Current, and arrives where the Atlantic Overturning (AMOC) happens. The Atlantic Overturning flux shows a relative strong interannual change (~4 Sv), the average Atlantic Overturning flux during 18 ka BP to 0 is 19.7 ± 2.6 Sv, the maximum value is 56.7 Sv and minimum is 14.41 Sv; the average of annual maxima is 21.9 ± 2.4 Sv and the mean of the annual minima is 17.6 ± 2 Sv. After a decrease after the spin-up the annual low value presents an increasing trend generally and the annual high value is decreasing. In the Atlantic Overturning, the warm water at the surface cools during its northward travel and sinks down to deeper layers and becomes subsurface cold water. This cold subsurface water flows south along the west Atlantic to the Antarctica circumpolar current (ACC). As a part of the ACC, the Drake Passage represents the strength of the ACC well. In the Drake Passage (fig. 4.6) after a quick drop, the flux keeps increasing until about 2 ka BP then decreases again. The mean of the annual peak value of the Drake Passage is 136.4 ± 4 Sv and the mean of the lowest is 128 ± 4 Sv. Comparing with other key currents, the Drake Passage has highest volume transport with a relatively small interannual variation. Via the cold water routine, the cold and fresh water is sent to the North Pacific and generates the deeper branch of the Pacific Meridional Overturning (PMOC). In the Ctl 1 run, the Pacific Overturning in fig. 4.6 presents a relatively strong annual variation and stable variation. The Southern Hemisphere Overturning in the FRUGAL model includes all the overturning across the Southern Ocean. Therefore, the Southern Hemisphere Overturning (SHOC) is much larger than all other overturning fluxes. There is a significant increase at about 7 ka BP, and the annual variation much narrowed immediately and gradually increased again. The annual variation of the Southern Hemisphere Overturning is between about 5 to 35 Sv and the average flux is 19.9 ± 10.9 Sv. The mean of annual maximum is 34 ± 3.7 Sv, and for the minimum is 11.9 ± 10 Sv.

The dramatic change at about 7 ka BP is more considered as a real event instead of a systematic accident. The ocean core proxy data from the Atlantic sector of the Southern Ocean suggests that the Southern Ocean Overturning was strengthened at about 8 ka BP (fig 3c in Anderson et al., 2009), which matches the suddenly increased SHOC.

The fig 4.7 shows the FFT results of the Drake Passage, AMOC, PMOC and SHOC from the Ctl 1 simulation. All the series suggest that the fluxes variability is time-independent but with different slopes, which suggests the main period of each flux is different. For the Drake Passage, there is a significant drop in the period of about 100 years. The PMOC shows much lower long-term energy, which consistent with its stable variability (fig 4.6).

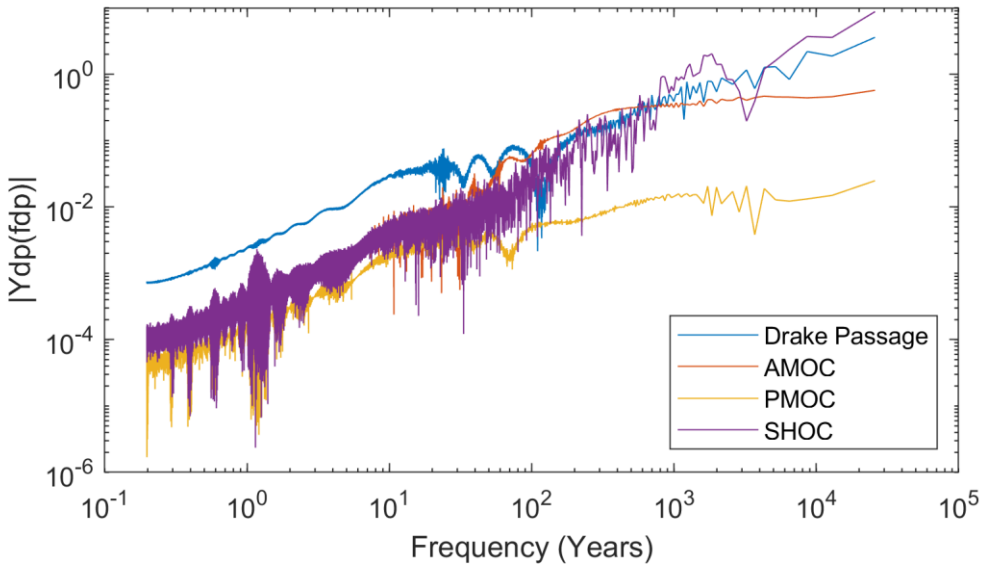

Figure 4.7 The Fast Fourier Transform of the Ctl 1 simulated fluxes of the Drake Passage (blue), Atlantic Meridional Overturning Current (AMOC; red), Pacific Meridional Overturning Current (PMOC; yellow) and Southern Hemisphere Overturning Current (SHOC; purple).

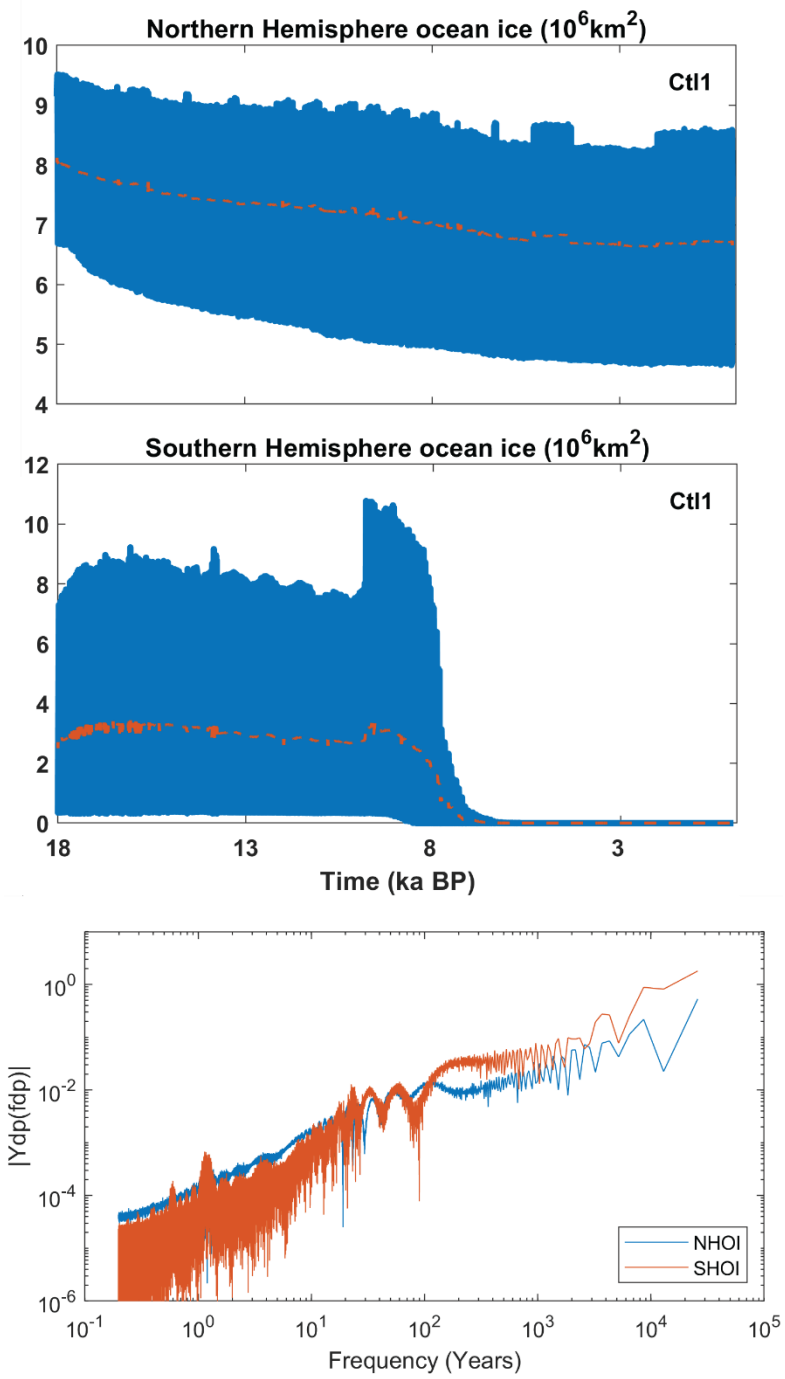

Fig 4.8 The Northern and Southern Hemisphere Ocean ice monthly variation from the Ctl 1 simulation, the decadal moving mean in orange dashed line, and the FFT results of origin series (bottom).

Under the LGM background, the most obvious difference with nowadays is the ice coverage. Moreover, the variation of the ocean ice coverage reflects the ITF's remote influence well. Fig. 4.8 introduces the ice variation in the Ctl 1 simulation. The Northern

Hemisphere ocean ice shows a noticeable decreasing tendency with a significant annual variation. The decreasing of the annual minima is quicker than the maxima. For the Southern Hemisphere ocean ice, the annual difference is bigger than the Northern, and both the annual maximum and minimum values decrease but there is a dramatic drop for the annual peak value at around 8 ka BP, from about 8-10 10^6 km^3 to near zero, which matches to the SHOC. Therefore, the decrease of the sea ice might cause by warming and dynamic movement due to the increased Southern Hemisphere Overturning. From the ocean core reconstruction data at the Drake Passage, research shows that a stronger ACC is related to a smaller sea ice coverage around the Antarctic (Wu et al., 2021). Therefore, this dramatic decreasing might be linked to the increasing of the Drake Passage flux seen in fig. 4.6 also. The FFT results (fig. 4.8) also suggest that the variations of both hemispheres ocean ice are time-independent and present the similar insignificant contribution as the current fluxes at around 100 years period.

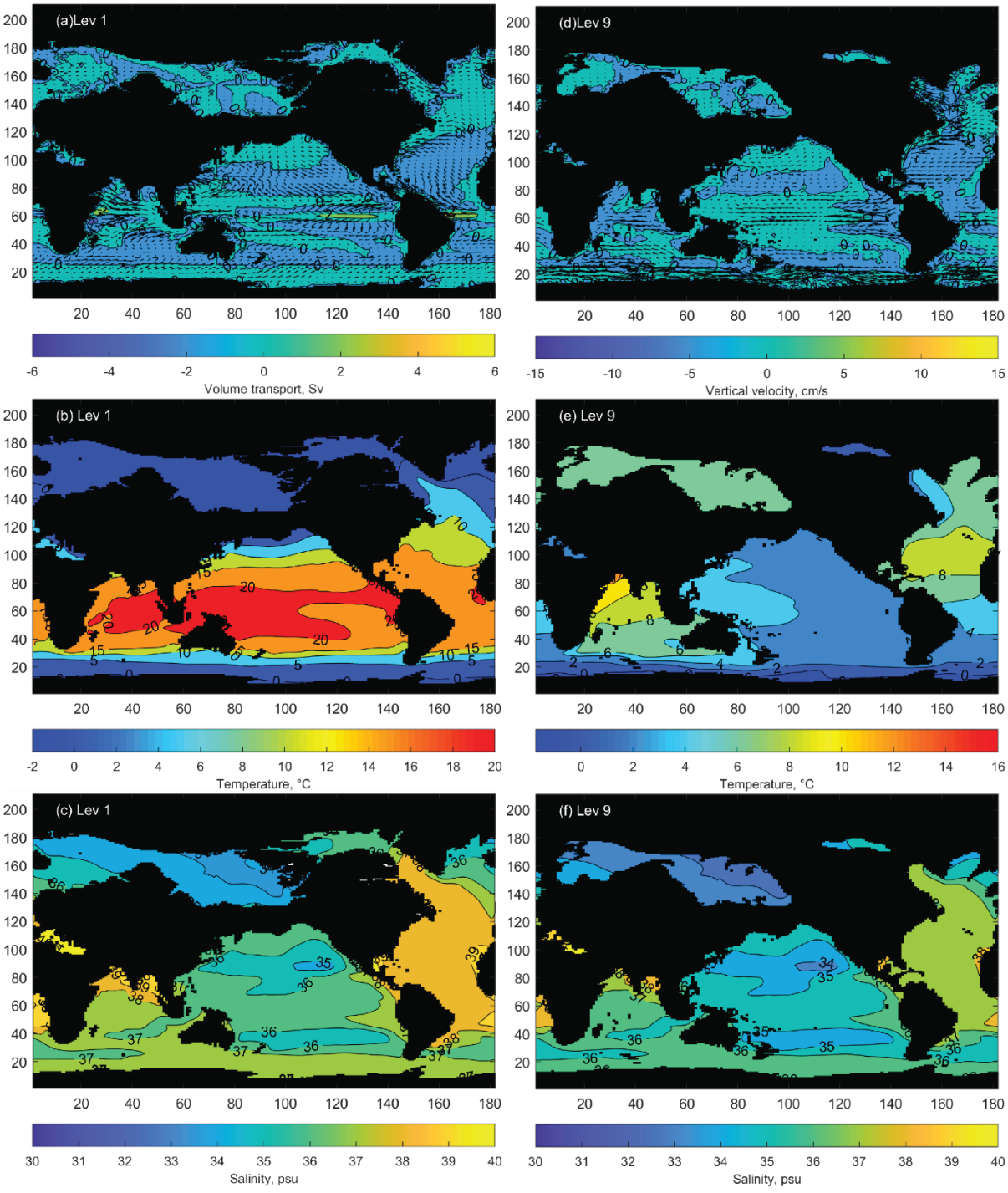

Fig 4.9 The January 18 ka averaged global ocean current (in vector) and vertical velocity of surface (a) and level 9 (d) (in contour, unit: cm/s), temperature (°C) at surface (b) and level 9 (e), and salinity (psu) at surface (c) and level 9 (f) of the Ctl 1 simulation.

After the Ctl simulation reached equilibrium, two representative layers are selected to stress the main hydrological features. The averaged global ocean surface current (fig 4.9(a)) presents a slightly different pattern than nowadays (fig 4.10(a)). In the Pacific, the equatorial counter current is stronger in the Ctl 1 run than the present-day; both the north and south equatorial current is weaker than present-day (fig 4.10(a)), but the north equatorial current barely exists in the Ctl 1. Although the Java Sea was shut, the inflow and outflow of the ITF are very significant. As the downstream of the ITF, the equatorial currents in the Indian Ocean are similar to the modern pattern but present a strong westward bias than the present-day (fig 4.10(a)). For other regions of the global meridional circulation: the Atlantic North Equatorial Current and Gulf Stream current are close to the present pattern but the North Atlantic Drift is less obvious. In the Southern Ocean, the Antarctic Circumpolar Current extends meridionally over a wider range but weaker than present-day (fig 4.10(a)), and the counter current is very weak. The vertical velocity responds to the horizontal current changes also. Along the east equatorial Pacific, west equatorial Atlantic and east Africa coast there is strong upwelling. The SST (fig 4.9(b)) is generally cooler than present-day (fig 4.10(b)), the cold tongue at the east equatorial Pacific and west equatorial Indian Ocean matches the distribution of the vertical velocity, where the upwelling brings deeper and cooler water to the surface. The east equatorial Indian Ocean is relatively warmer than the west due to the ITF transports of warm west equatorial Pacific water westwards also. The North Atlantic and the Southern Ocean are much cooler than present day (fig 4.10(b)). As fig 4.9(c) shows, the Arctic and North Pacific are relative fresher and the north Indian Ocean and Atlantic are saltier. There is a clear fresh path from the west equatorial Pacific to the east Indian Ocean which indicate the mass transport of the ITF. The counter currents appear at level 9 (depth: 1200 m; fig 4.9(e)), the east equatorial Pacific is controlled by a westward current and the west is controlled by an eastwards current. The equatorial Indian Ocean is dominated by an

east current. Comparing with the rest of the global ocean, the northern Atlantic and Southern Ocean have stronger currents. The vertical transport is relatively weak, the north and east Pacific, the Atlantic and the equatorial and west Indian Ocean present weak downwelling. At this level, the Arabian Sea and north Atlantic is relatively warmer than the rest of the global ocean due the global thermohaline circulation, and a cold tongue along the east North America coast (fig 4.9(f)). The salinity of the Bay of Bengal and Atlantic are higher and the Arctic and northern Pacific are fresher (fig 4.9(d)).

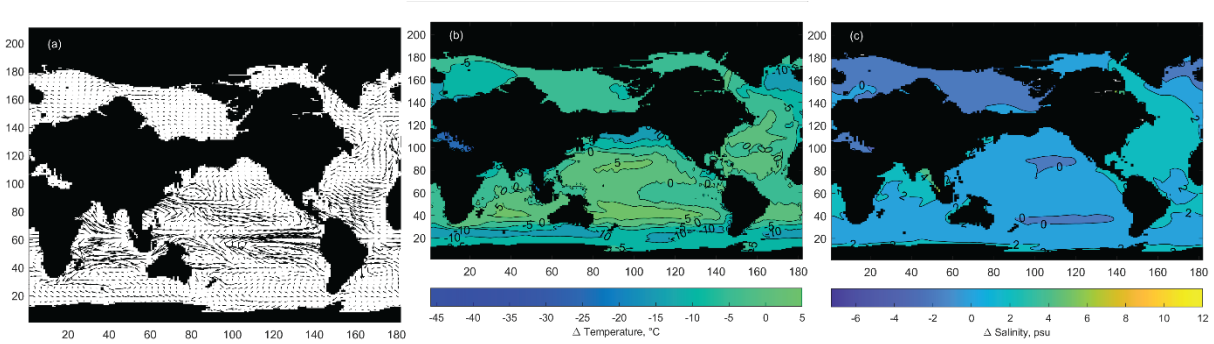

Fig 4.10 The difference of global ocean surface current (a), temperature (bb; unit: ℃) and salinity (c, psu) between the Ctl 1 run and averaged from 1987 to 2015 (dataset: FRUGAL present-day simulation personal communication, Ross, 2022).

The Ctl 1 simulated the deglacial progress with a spin up, successfully represented the global hydrological characteristics. The ocean currents and properties present a clear difference with the present day situation. In the following chapters, the effects of insolation variation in the FRUGAL palaeo simulation will be introduced first, then the thesis will focus on the local and global impact of a closed ITF under the palaeo-conditions.

Chapter 5 The Effects of the Insolation Variation in the FRUGAL Palaeo Simulation

In chapter 4, the FRUGAL model and the control simulation, Ctl 1, are introduced. As the simulation plan shows, the Ctl 2 simulated the natural variability with varying insolation, which represented a core element of the deglacial procedure. The insolation variation plays essential role in palaeoclimate, both reconstructed dataset and modelling results suggest that the insolation variation corresponds to the change of ice cover and sea level etc (Yin, 2013; Cutler et al., 2002; Risebrobakken et al., 2006; Robinson and Goelzer, 2014). Therefore, it is important to value the performance and interaction in the FRUGAL with varying insolation. In this chapter, the effect of the insolation variation in the FRUGAL paleo simulation is studied. The impact on the key currents of the global thermohaline circulation and ocean ice fluxes are discussed first. The second discussion focuses on the effects of insolation variation to the global oceanographic characteristics. Based on differences between the Ctl 1 and 2 simulations, section 5.3 focuses on the hydrological characteristics variation of insolation sensitive areas.

5.1 The Impact of Insolation Variation on Thermohaline Circulation and Ocean Ice

5.1.1 The Ctl 2 Simulation Results

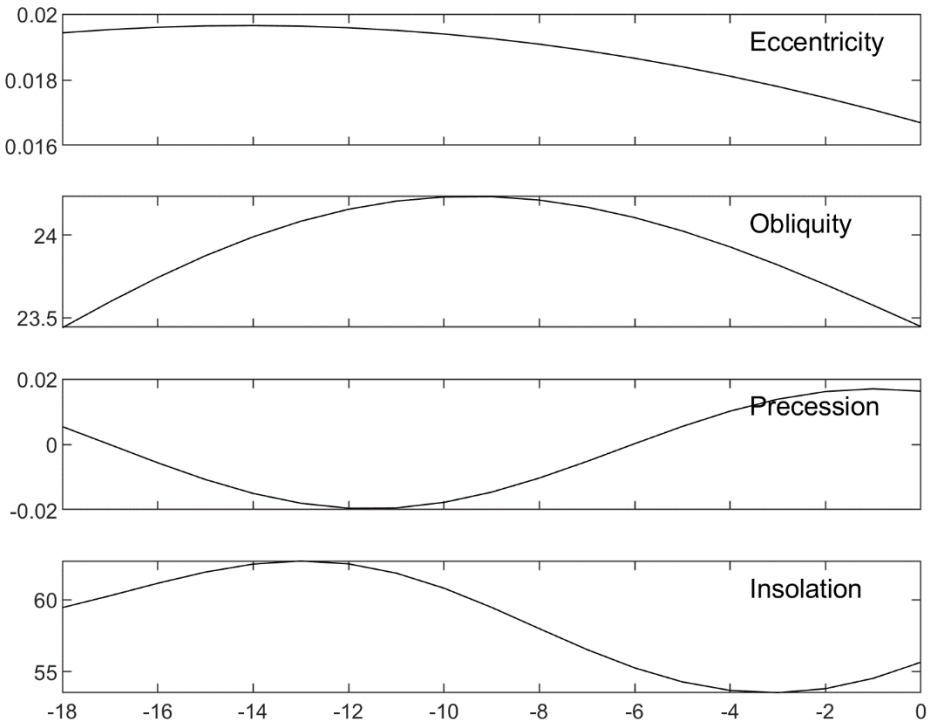

Figure 5.1 The variations of the eccentricity, obliquity, precession and insolation (unit: W/m^2) at 55 °S during 18 ka BP to now, calculated based on Berger's solution (1978).

Comparing with the Ctl 1 simulation, the Ctl 2 focuses on simulating the deglacial process by allowing the varying insolation. Fig 5.1 presents the variations of the eccentricity, obliquity, precession and insolation at 55 °S from 18 ka BP to now. During this period, the eccentricity increases mildly until 14 ka BP and decreases to now. It suggests that the Earth orbit is more circular after 14 ka BP, therefore, the seasonal changes would be smaller. The obliquity suggests that the tropical area reached a maximum at 9 ka BP, and decreased again. The equinoxes and solstices delayed between 18 to 12 ka BP but advanced afterwards. Considering the values of variations, the obliquity contributes more to the insolation variation than the precession. Due to the Drake Passage representing the Southern Ocean well, the insolation variation presented here is at 55 °S. The insolation reached a maximum at 13 ka

BP and dropped to a minimum at 3 ka BP. The decreasing speed of the insolation is fastest at around 8 ka BP.

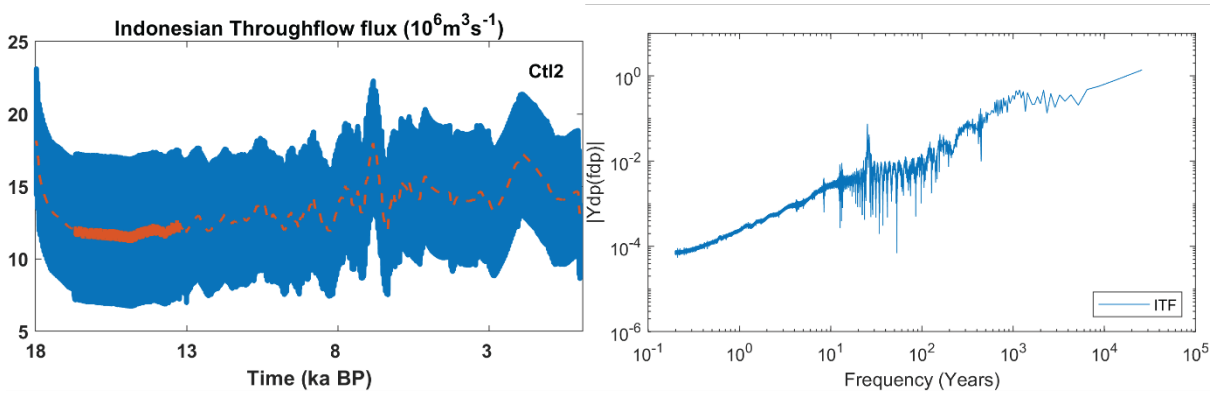

Figure 5.2 The monthly ITF flux from the Ctl 2 simulation (left) and the decadal moving mean in orange dashed line, and its FFT result (right).

In the global thermohaline circulation, the warm water route starts in the North Pacific. The warm and salty water flows into Indian Ocean via the ITF. Fig 5.2 shows the monthly ITF flux and its FFT spectrum from the Ctl 2 simulation. After the drop around 18 ka BP, the ITF flux presents a gentle increasing trend with a strong annual cycle. The average ITF flux is 13.2 ± 3 Sv, the mean annual maximum is 17.9 ± 1.4 Sv and the mean annual minimum is 8.7 ± 1.6 Sv. The FFT result suggests that the Ctl 2 ITF flux has a fairly time-independent variability, although there is a relatively strong frequency of variability about 25 years. Comparing with Ctl 1 simulation (fig 4.5), due to the similar slope, the Ctl 2 ITF flux presents a comparable level of variability but with a more significant frequency about 25 years.

Table 5.1 The comparison of the ITF flux from the Ctl 1 and 2 simulations

Runs	Mean	Mean of annual max.	Mean of annual min.
Ctl 1	13.33 ± 3 Sv	17.9 ± 1.6 Sv	9 ± 1.8 Sv
Ctl 2	13.2 ± 3 Sv	17.9 ± 1.4 Sv	8.7 ± 1.6 Sv

As fig 5.3 shows, the tendency of the AMOC is relatively stable until ~8 ka BP and then turns to being more oscillatory. The mean AMOC flux is 19.8 ± 2.6 Sv, and the mean of the annual maxima and minima are 21.9 ± 2.5 Sv and 17.7 ± 2 Sv respectively. For the Drake Passage flux, there is a significant drop between 18 to 16 ka BP, and the flux increases until about 5 ka BP then oscillates to the end of simulation, which is similar to what occurred in the Ctl 1 simulation (fig 4.4). This behaviour is therefore internal variability in the model, rather than being caused by the change in insolation. The Drake Passage flux average in Ctl 2 is 132.6 ± 5 Sv and for the annual highest and lowest average values are 137 ± 4.2 Sv and 128.5 ± 4.4 Sv respectively. Therefore, the annual difference is relatively small. The variability of the Pacific Overturning is very small, the average strength is 8.3 ± 3.2 Sv and mean annual maximum and minimum are 12.5 ± 0.1 Sv and 3.6 ± 0.3 Sv respectively. The Southern Hemisphere Overturning shows a close stable variability between 18 – 12 ka BP, but due to the variation of the annual minimum being much stronger after 12 ka BP, the interannual variation decreases during this period also. There are two peaks that appear at about 6.5 ka BP with the value of 60.6 Sv and at about 2 ka BP with the value of 52.4 Sv. The SHOC mean is 18 ± 10.3 Sv, the mean of the annual maximum and minimum are 33.5 ± 3.5 Sv and 9.2 ± 7.5 Sv respectively.

Fig 5.4 presents the fluxes FFT result for the Drake Passage, AMOC, PMOC and SHOC. All four of them present a time-independent character. The background level of the PMOC suggests that the PMOC has relatively small variability; the main frequency of its

variability is at the annual time scale. The AMOC and PMOC series present a similar slope, which suggests that they share a similar variability background, but the main frequency of the AMOC variability is decadal in scale. The Drake Passage flux has the highest variability and the main frequency distributes between decadal to multi-centennial. The SHOC presents the most significant variability between interannual to several decades in time scale.

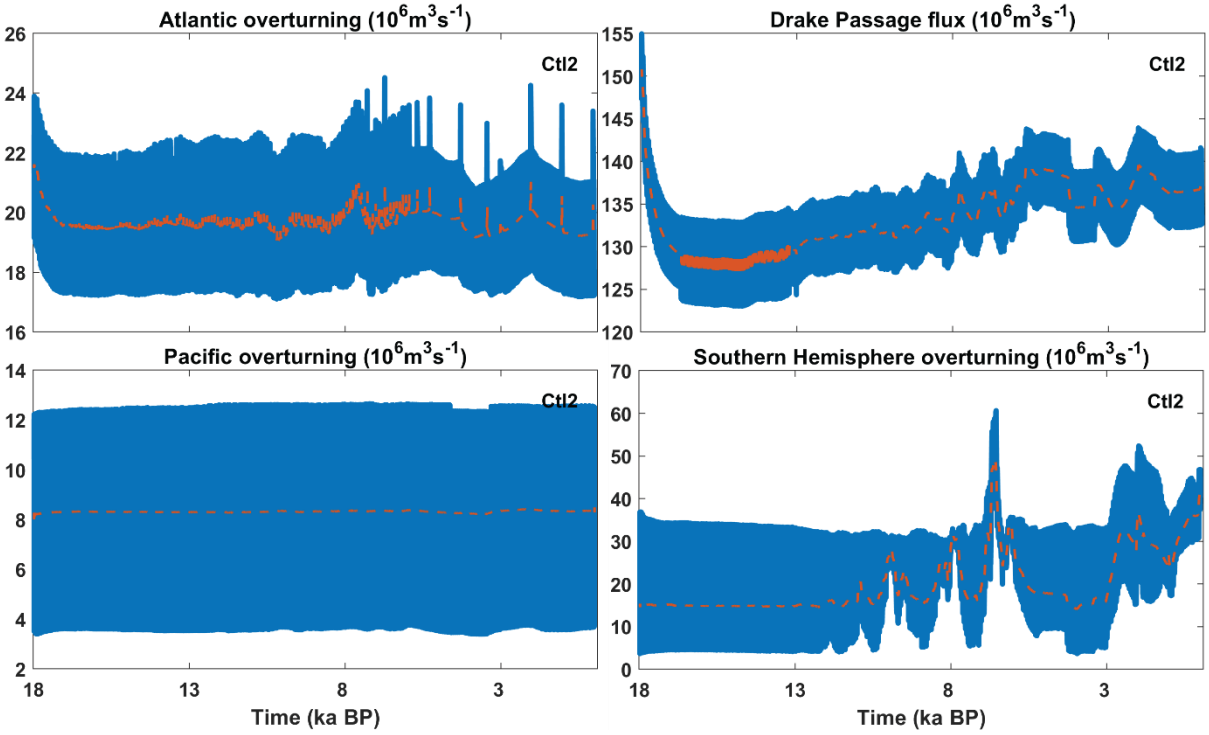

Figure 5.3 The monthly fluxes of AMOC, Drake Passage, PMOC and SHOC from the Ctl 2 simulation, and the decadal moving mean in orange dashed line.

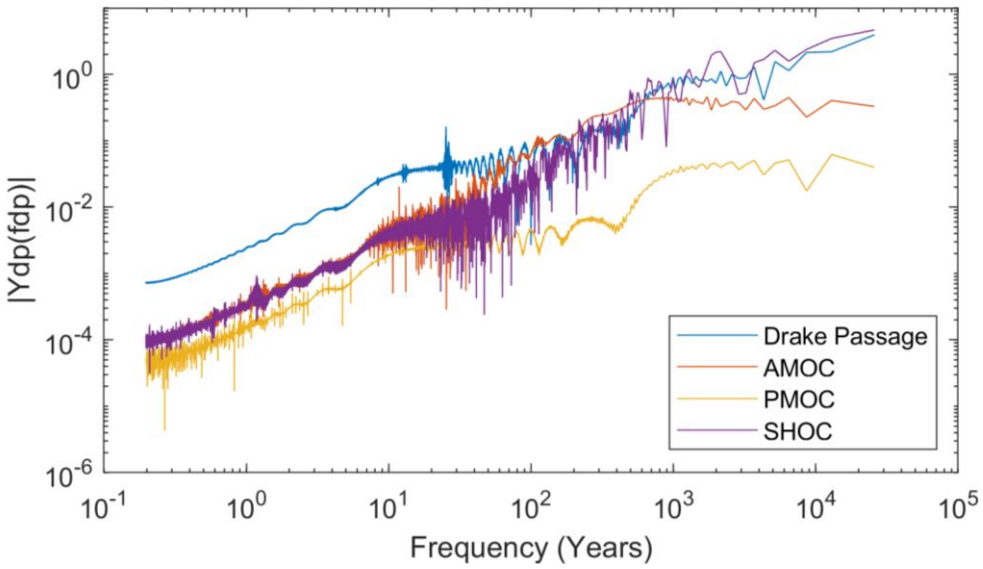

Figure 5.4 The FFT of the Drake Passage, AMOC, PMOC and SHOC from the Ctl 2 simulation.

The ocean ice cover is the most obvious parameter that changes during the deglacial process. Fig 5.5 presents the Northern and Southern Hemisphere Ocean sea-ice variations. The Northern Hemisphere Ocean Ice (NHOI) shows a significant decreasing tendency with a strong annual variation. The average NHOI is 7.2 ± 1.3 10^6 km^2, and the average annual maxima and minima are 8.9 ± 0.3 10^6 km^2 and 5.3 ± 0.6 10^6 km^2. The Southern Hemisphere Ocean Ice (SHOI) presents a huge annual variation of about 8 10^6 km^2 between 18 to ~8 ka BP, but the ocean sea-ice drops to 0 at about 7 ka BP, which is same with the Ctl 1 simulation. Therefore, the ocean ice melting at about 8 ka BP is due to model natural variability, rather than the insolation variation. Additionally, the period that the melting happens matches with the increasing of the SHOC (fig 5.3), therefore, this relates to the strengthened overturning also. The SHOI presents an extremely strong variability. The mean SHOI is 2 ± 2.7 10^6 km^2, and the mean annual highest and lowest are 5.9 ± 3.9 10^6 km^2 and 0.25 ± 0.2 10^6 km^2 for the whole simulation period; before and after the catastrophic sea-ice collapse (7 ka BP), the mean SHOI are 3.49 ± 4.28 km^2 and 0.004 ± 0.028 km^2 respectively. The mean annual maximum and minimum are 7.61 ± 2.52 km^2 and 0.33 ± 0.15 km^2 before

the drop, and 0.02 ± 0.06 km^2 and 0 km^2 for after. The FFT of the NHOI and SHOI is shown in fig 5.6. Compared to the NHOI, the SHOI presents a significant strong variability higher than 100 years frequency.

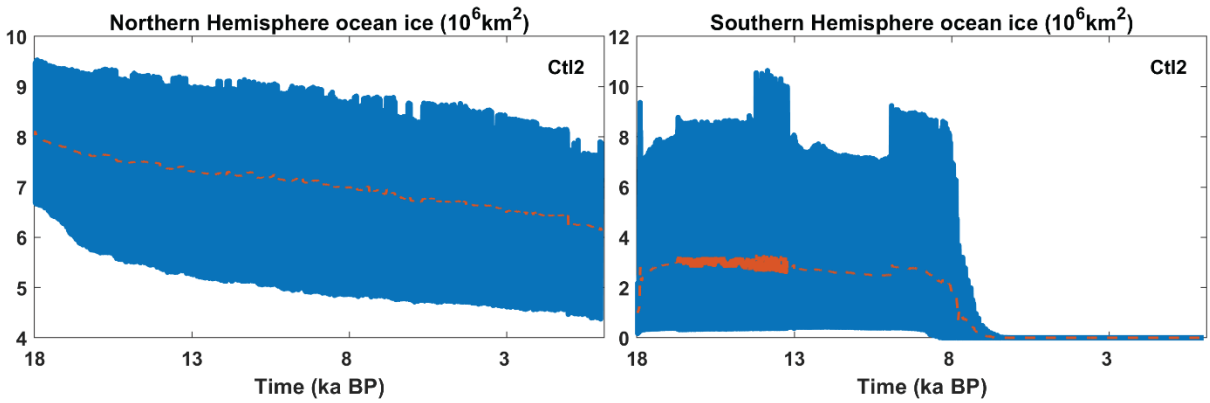

Figure 5.5 The Northern and Southern Hemisphere Ocean Ice from the Ctl 2 simulation, and the decadal moving mean in orange dashed line.

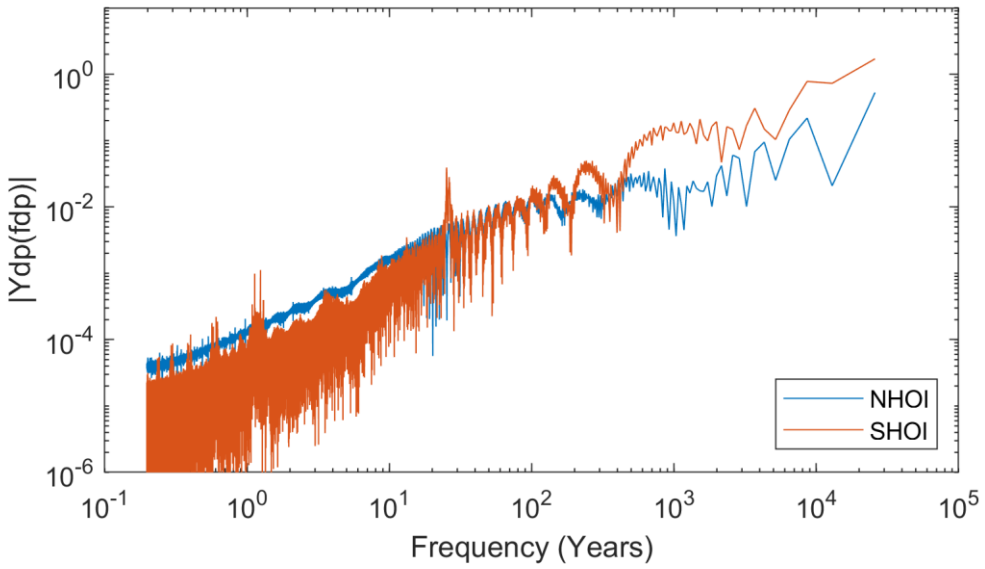

Figure 5.6 The FFT of the NHOI and SHOI from the Ctl 2 simulation.

The next section will consider in more detail the differences between the two Ctl experiments, and therefore what characteristics of Ctl2 are due to the change in insolation.

5.1.2 The Differences Between the Ctl 1 and 2 Simulations

The difference of the key thermohaline currents between the Ctl 1 and 2 simulations are considered for a clearer view of how the insolation variation affects the simulation. In this chapter, all the differences between the Ctl 1 and Ctl 2 are considered through taking the variables from the Ctl 2 simulation minus those from the Ctl 1 simulation. The flux differences are shown in Fig 5.7. The differenced ITF series presents a significant fluctuation. The biggest difference is about 4 Sv and appears at the end of the pre-spinup and about 2 ka BP. Between 18-8 ka BP, the ITF flux difference varies around 0, but after 8 ka BP, the range of the difference increases a lot. Comparing with the model's natural variability, the varying insolation makes the ITF smaller between ~5.5-2.8 ka BP and larger between 2.8 ka BP to 0.

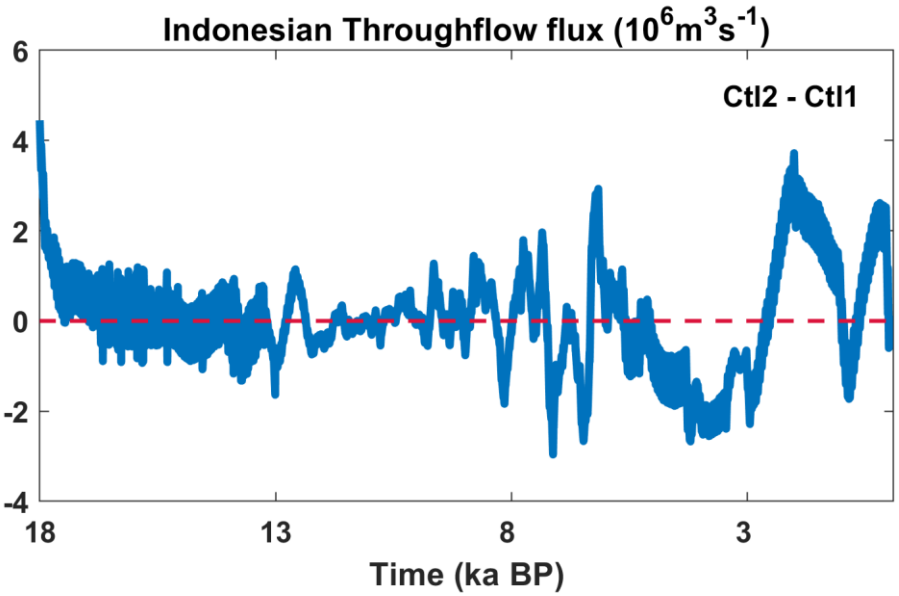

Figure 5.7 The ITF flux monthly difference between the Ctl 1 and 2 simulations. The dashed red line indicates the value of 0.

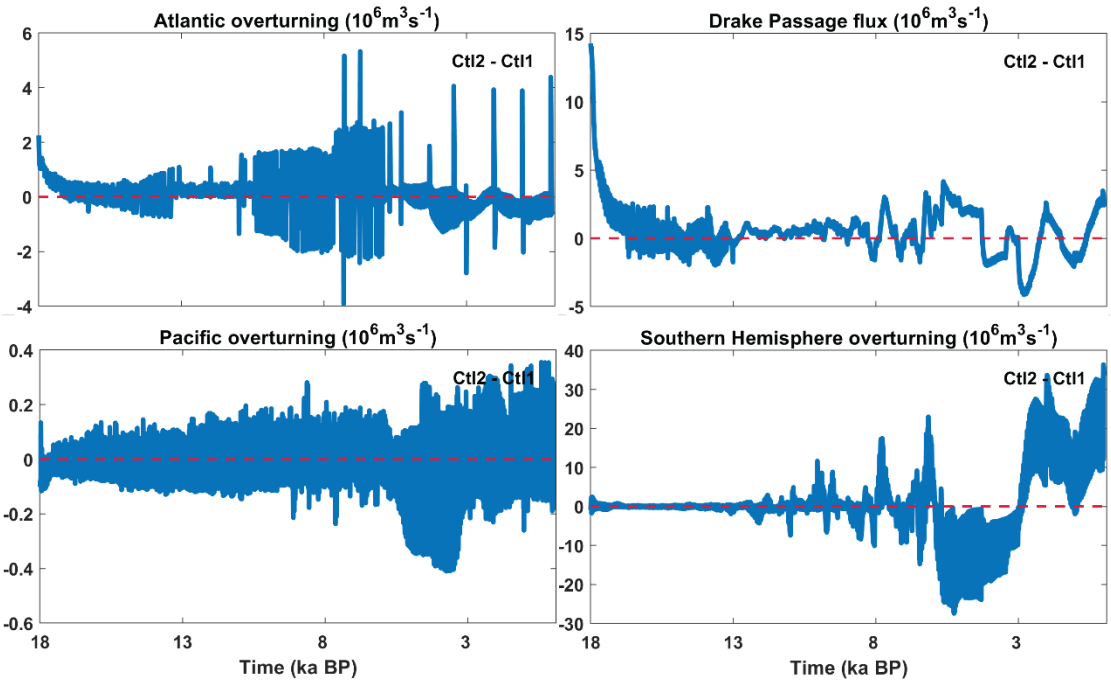

Figure 5.8 The fluxes monthly differences of the AMOC, Drake Passage, PMOC and the SHOC between the Ctl 1 and 2 simulations. The dashed red line indicates the value of 0.

For the AMOC, between 18-13 ka BP (fig 5.8), the insolation variation mostly affects the AMOC annual amplitude, but has less impact on the long-term scale; between 13-10 ka BP, the annual maximum is higher in the Ctl 2 than the Ctl1 simulation; the difference annual amplitude is about ± 2-4 Sv between 10 to 5 ka BP and the extreme difference values are about 5.3 Sv and -3.8 Sv, and appears ~6.7 ka BP and ~7.6 ka BP respectively; after 5 ka BP, the AMOC difference is mainly negative, although some individual years have a significant positive bias.

The Pacific Overturning responds to the varying insolation by increasing the range of its annual variation, but the mean difference is near 0. The Ctl 2 PMOC is relatively weaker than the Ctl 1 run during 6 to 3 ka BP comparing with other periods, and after 3 ka BP the Ctl 2 flux is generally stronger than the Ctl 1. Unlike the other 4 currents, the Southern Hemisphere Overturning does not respond to the end of pre-spinup significantly. During 18

to 13 ka BP, the SHOC is not sensitive to the insolation variation. The difference becomes much more noticeable between 13 to 8 ka BP and very strong afterwards. After 6 ka BP, the Ctl 2 SHOC is nearly 30 Sv less than in the Ctl 1 run and the difference increases to more than 35 Sv.

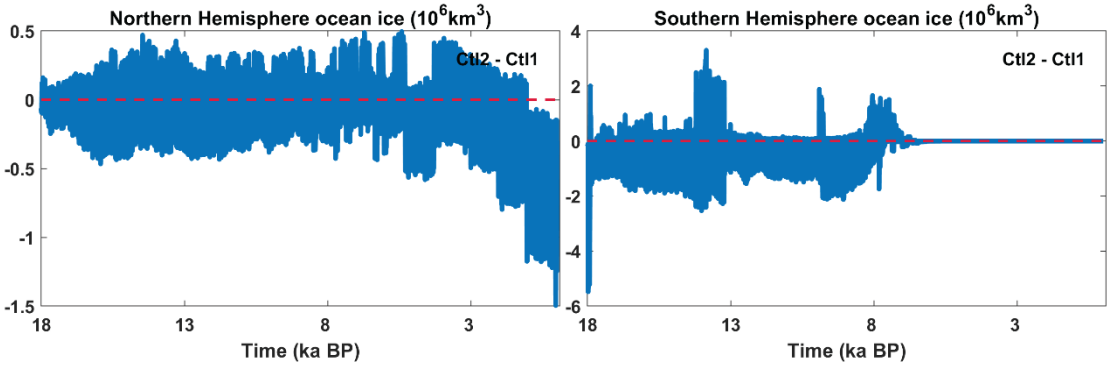

Figure 5.9 The fluxes differences of the NHOI and SHOI between the Ctl 1 and 2 simulations. The dashed red line indicates the value of 0.

The differences of the Northern and Southern Hemisphere Ocean Ice between the Ctl 1 and 2 runs are presented in fig 5.9. The insolation variation strengthens the NHOI annual variation by about ± 0.5 10^6 km^2, but the mean difference is near 0 between 18 to about 5.5 ka BP. After ~5.5 ka BP, the insolation makes the NHOI reduce by 1.5 10^6 km^2 eventually. The Southern Hemisphere Ocean Ice responds to the insolation at the pre-spin most significantly; before the ~8 ka BP, the Ctl 2 SHOI is smaller than the Ctl 1 in general, but at about 12, 10 and 8 ka BP, there are three peaks for the annual maxima. After 7 ka BP, due to the SHOI being essentially 0 in both runs, the difference maintains 0 also. Therefore, the FRUGAL's natural variability causes the Southern Hemisphere Ocean Ice to all melt after 8 ka BP.

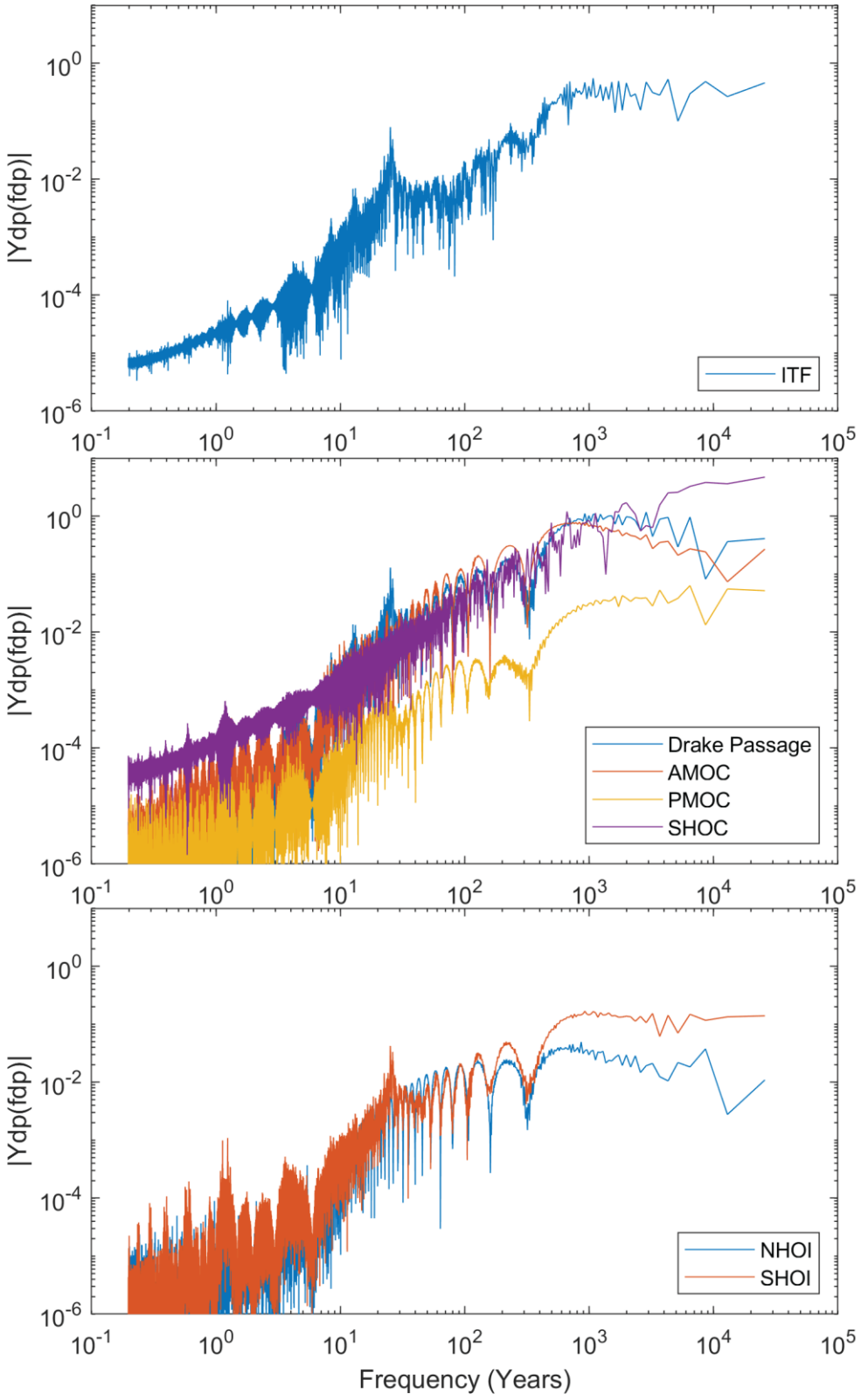

Figure 5.10 The FFT of the flux differences of the key currents, NHOI and SHOI between the Ctl 1 and 2 simulations

The FFT of the flux differences (fig 5.10) suggests that except for the Drake Passage and PMOC, the varying insolation mainly works on higher frequencies from annual to centennial scale, which matches the differences presented by the annual amplitude respectively (fig 5.7 and 5.8).

As a conclusion, within the varying insolation, the Ctl 2 presents quite periodic differences with the Ctl 1 simulation in the key currents of the thermohaline circulation. There are clearly three periods, 18-13 ka BP, 13-~6 ka BP and ~6 ka BP to 0. The Southern Ocean insolation variation reached maximum at 13 ka BP and dropped to minimum at 3 ka BP. This the potential reason might relate to the rapid strengthening of the Southern Hemisphere Overturning at about 8 ka BP.

5.2 The Impact of Insolation Variation on Global Oceanographic Characteristics

To study oceanic changes due to the insolation variation beyond those in the key currents, fig 5.11 shows the global current, vertical velocity, sea temperature and salinity differences at representative levels of surface, middle and deep layers. For the sea surface level (fig 5.11(a)), the Equatorial Pacific counter currents and the Antarctica Circumpolar Current are stronger, and the Equatorial Atlantic Current is weaker in the Ctl 2 run; the vertical velocity difference presents a downwelling tendency in most of the main ocean basins. In the temperature difference field (fig 5.11(b)), the Ctl 2 is generally cooler in the Indian Ocean, Pacific and Atlantic, especially in the North Atlantic, and warmer in both polar oceans, which suggests that the varying insolation makes the equator-pole temperature gradient smaller. The salinity from the Ctl 2 simulation is bigger than the Ctl 1 globally, especially in the Arctic and Southern Ocean (fig 5.11(c)).

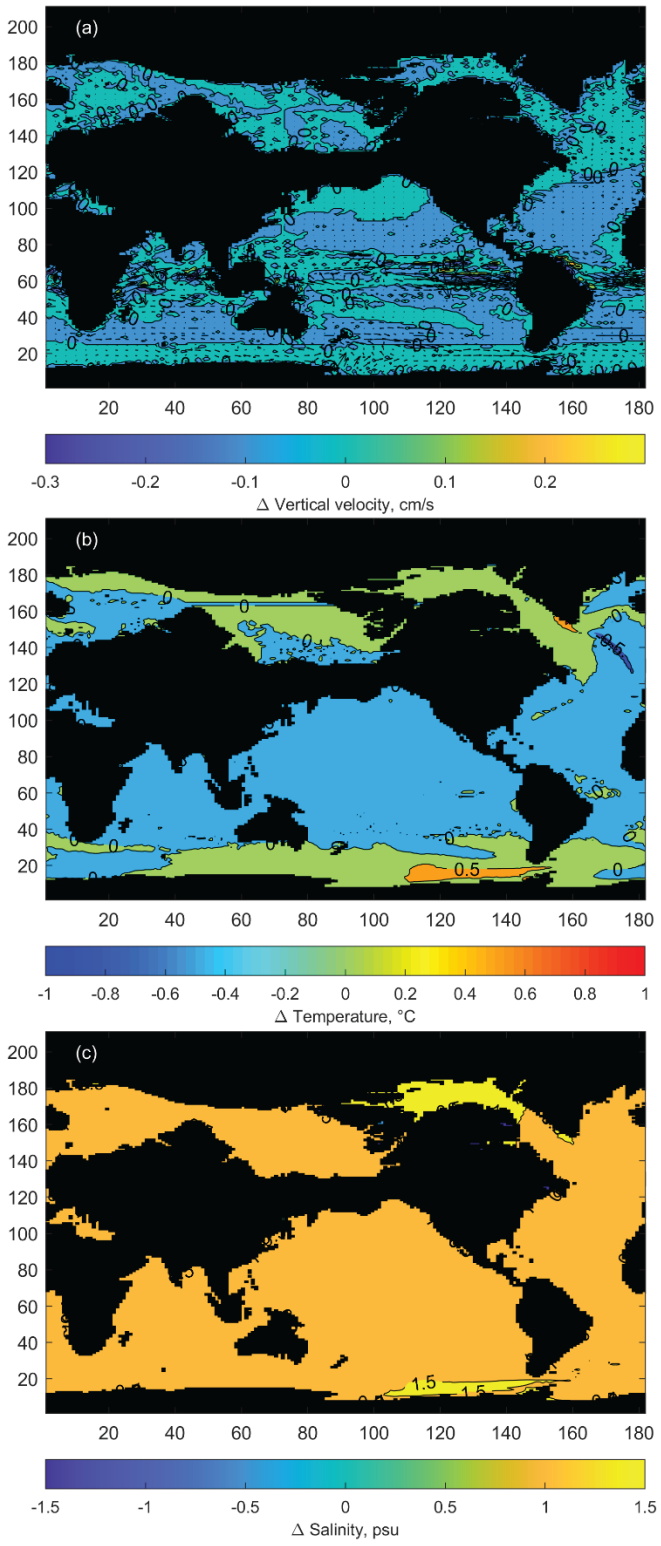

Figure 5.11 The annual January difference of (a): ocean current (in quiver) and vertical velocity (in contour, the upwelling in positive vice versa; cm/s); (b): sea temperature (°C) and (c): salinity (psu) of the level at 1 (surface) between the Ctl 1 and 2 simulations during 18 ka BP to 0.

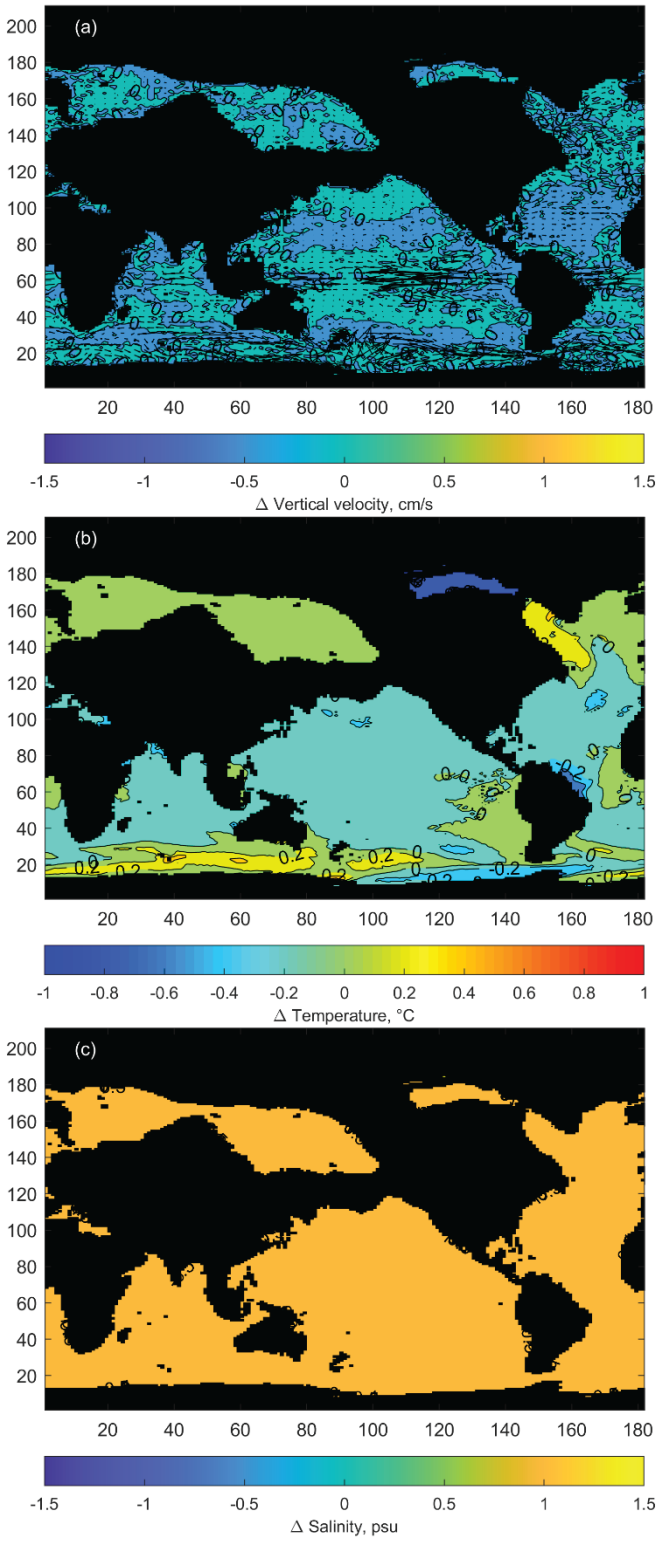

Figure 5.12 The annual January difference of (a): ocean current (in quiver) and vertical velocity (in contour, the upwelling in positive vice versa; cm/s); (b): sea temperature (°C) and (c): salinity (psu) of the level at 6 (depth: 450 m) between the Ctl 1 and 2 simulations during 18 ka BP to 0.

At level 6 (450 m; fig 5.12(a)), the Equatorial Pacific counter current is weaker, but the Equatorial Atlantic Current and ACC are stronger in the Ctl 2 run; in Ctl 2, more water flows from the Pacific into the Indian Ocean around the south of Australia, therefore that part of the ACC is weaker. Most of the basins, especially the Atlantic, present a negative tendency of the vertical velocity. In the sea temperature difference field for this level (fig 5.12(b)), under the effect of varying insolation, the Labrador Sea and most of the Southern Ocean is warmer, but the Arctic north of the North America Brazil coast and the Ross Sea to the Drake Passage is cooler. This warm bias in the South Indian Ocean might relate to there being more water flows into the Indian Ocean from the Pacific via here. Therefore, the Arctic-Labrador Sea temperature gradient is strengthened. At this depth, the Ctl 2 run is globally saltier than the Ctl 1 (fig 5.12(c)).

At level 10 (depth: 1600 m, fig 5.13(a)), the most noticeable differences are the eastward current at the west Equatorial Pacific, eastward current to the south of Australia and northward current in the East Atlantic. For the temperature difference distribution (fig 5.13 (b)), the Arctic and Labrador Sea are relatively warmer in the Ctl 2 simulation. Due to the strengthened transport from the Pacific and Indian Ocean via the south of Australia, the temperature is warmer there but cooler in the North Indian Ocean and the Ross Sea to the Drake Passage in the Ctl 2 simulation. The salinity difference is similar to that at level 6 - it is saltier globally, especially in the Arctic in Ctl 2 (fig 5.13(c)).

Therefore, for the currents, the Equatorial Pacific/Indian Ocean/Atlantic, and the Southern Ocean are very sensitive to the insolation variation, especially the Southern Ocean to the south of Australia. The temperature and salinity respond to the insolation changes most significantly at both polar oceans and globally are cooler and saltier.

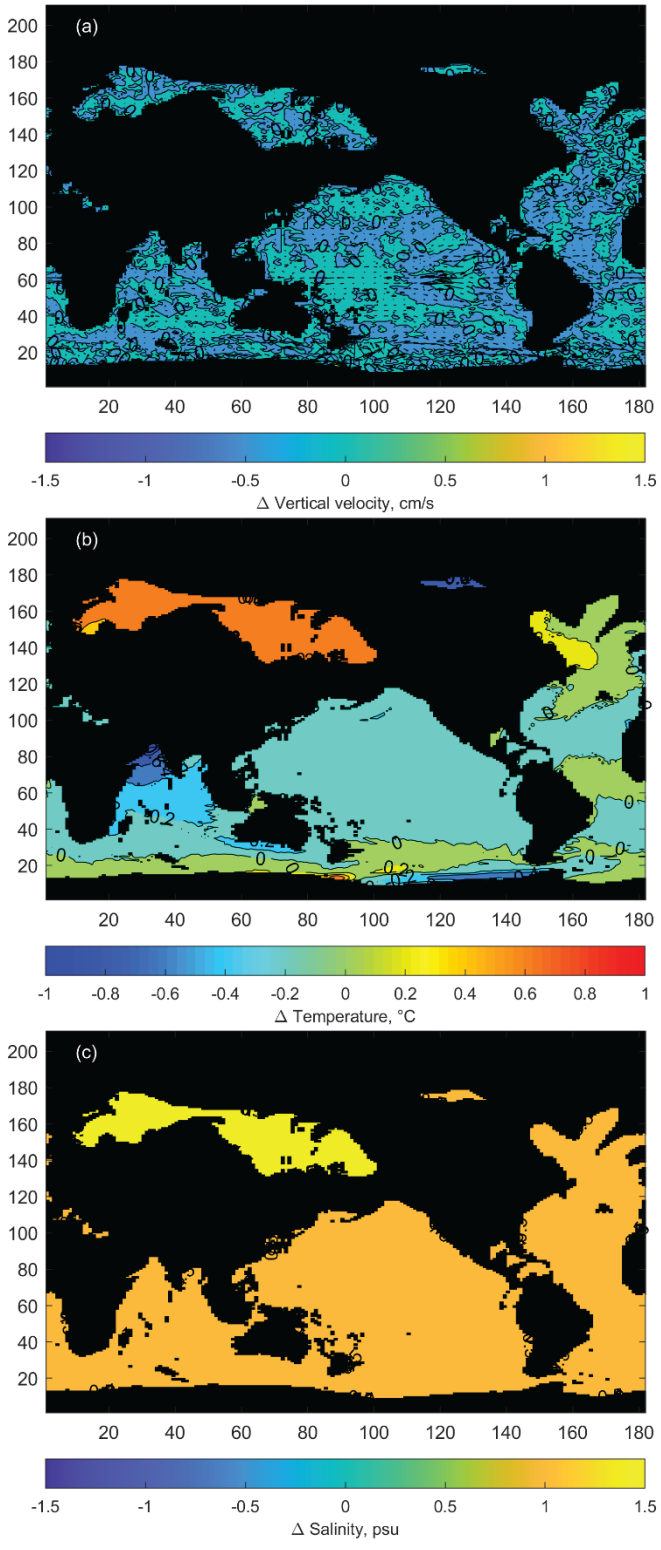

Figure 5.13 The annual January difference of (a): ocean current (in quiver) and vertical velocity (in contour, the upwelling in positive vice versa; cm/s); (b): sea temperature (°C) and (c): salinity (psu) of the level at 10 (depth: 1600 m) between the Ctl 1 and 2 simulations during 18 ka BP to 0.

5.3 The Impact of Insolation Variation on Sensitive Areas

According to the key elements of the difference fields between the Ctl 1 and 2 simulations (fig 5.11), to examine in detail the impact of varying the insolation a number of sensitive areas are selected (fig 5.14). Fig 5.15 presents salinity, temperature and density differences of the selected sensitive areas between the Ctl 1 and 2 simulations at level 1 (surface level). In salinity and density differences there is a significant tendency change at about 7 ka BP (fig 5.15).. Therefore, the following discussion focuses on the long term characteristics during the whole simulation period and before and after the significant gap at ~ 7 ka BP.

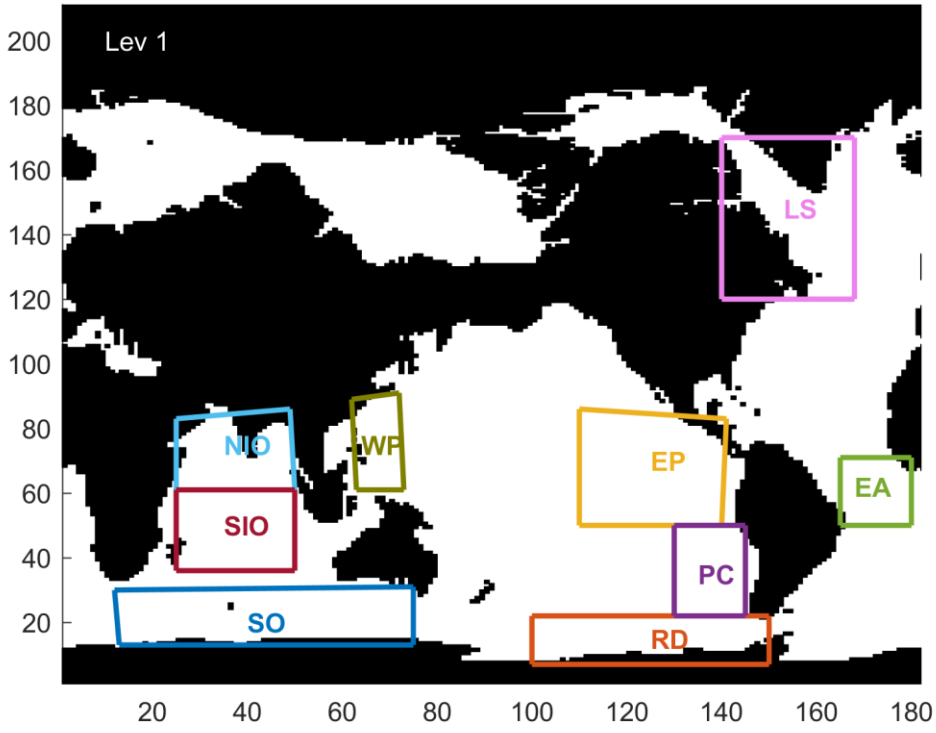

Figure 5.14 The insolation sensitive areas in FRUGAL topography. NIO: North Indian Ocean; SIO: South Indian Ocean; SO: Southern Ocean; WP: West Pacific; EP: Equatorial Pacific; PR: Peru Current; RD: Ross Sea to Drake Passage; LS: Labrador Sea; EA: Equatorial Atlantic.

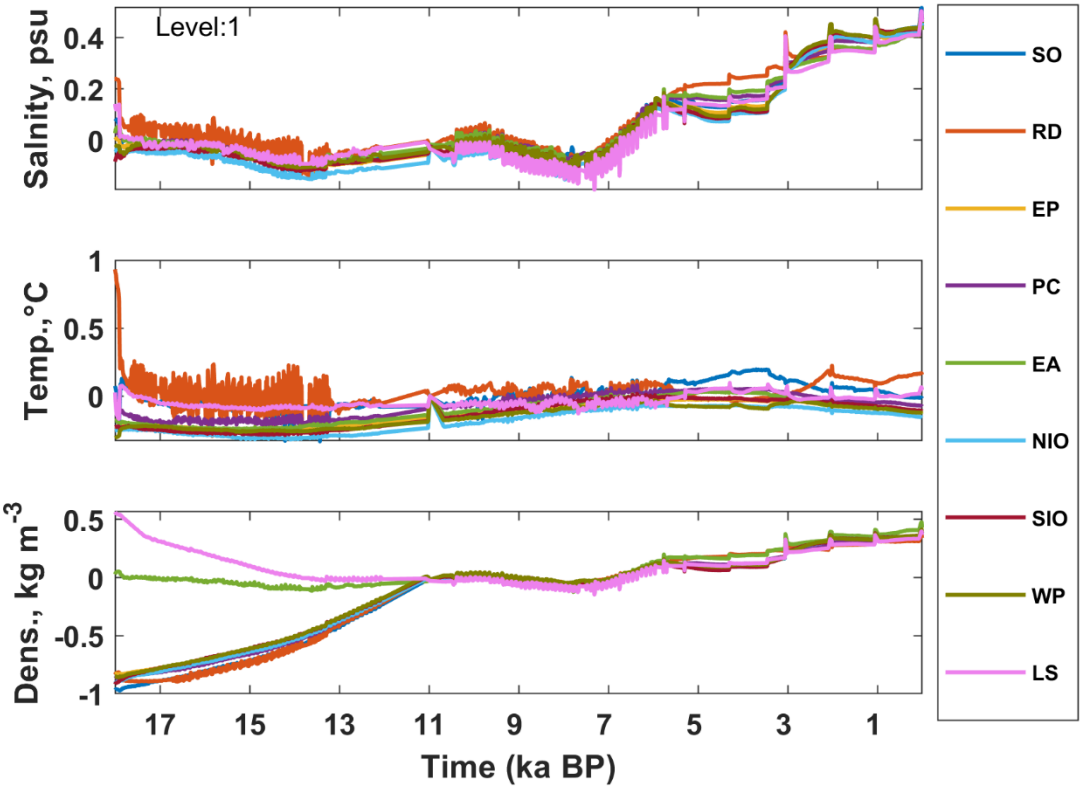

Figure 5.15 The key areas differences variation of salinity, temperature and density of the level 1 between the Ctl 1 and 2 simulations.

At level 1 (fig 5.15), over the entire simulation, all the areas are saltier in the Ctl 2 simulation, by about 0.05 psu. For the temperature differences, the Southern Ocean and Ross Sea to Drake Passage are warmer, and others are colder in Ctl 1, especially the Northern Indian Ocean (-0.17 ± 0.09 ℃). Except that the Equatorial Atlantic is 0.06 ± 0.15 kg m^{-3} denser, the rest of regions are less dense in the Ctl 2 than Ctl 1 simulation. Before ~7 ka BP, all the key areas present a negative bias in salinity differences, In the temperature difference, only the RD region is warmer (0.02 ± 0.13 ℃), and all the rest of the regions are colder in Ctl 1. The NIO, SIO and WP show a relatively strong cold difference -0.24 ± 0.07 ℃, -0.19 ± 0.09 ℃ and -0.2 ± 0.06 ℃ respectively. The Labrador Sea is denser, 0.07 ± 0.17 kg m^{-3}, than in Ctl 1, and the Equatorial Atlantic shows a relative weaker less dense difference (-0.05 ± 0.04 kg m^{-3}) during this period. Other key areas are less dense in Ctl 2 by about 0.36 kg m^{-3}.

After ~7 ka BP, all the regions are saltier in Ctl 2 by about 0.2 psu. During this period, the SO, RD and PC regions are warmer in Ctl 2 by about 0.09 ± 0.06 ℃, 0.05 ± 0.06 ℃ and 0.02 ± 0.04 ℃ respectively. For the density, all the areas are denser in the Ctl 2 simulation during this period.

At the middle layer (fig 5.16), during the whole simulation period, all the key areas are saltier than in the Ctl 1 run, especially the Ross Sea to Drake Passage (0.2 ± 0.11 psu). For the temperature, the Southern Ocean and Equatorial Atlantic are relatively warmer by about 0.11 ± 0.08 ℃ and 0.09 ± 0.14 ℃, and the Ross Sea to Drake Passage and the Peru Current are slightly warmer in the Ctl 2 than the Ctl 1 too. The rest of the regions are cooler in Ctl 2, especially the North Indian Ocean being 0.14 ± 0.03 ℃ cooler than the Ctl 1 run. Only the Equatorial Atlantic is slightly denser, by about 0.08 ± 0.14 kg m^{-3}, the others are less dense by about 1.8 kg m^{-3} in Ctl 2 than Ctl 1 simulation. Before about 7 ka BP, the RD region presents a positive bias in salinity difference, 0.16 ± 0.08 psu, all the other regions' salinity differences are negative. For the temperature, the North Indian Ocean, South Indian Ocean, West Pacific, Labrador Sea and East Pacific are colder, and the rest are warmer in Ctl 2. Among those areas, the NIO, SO and EA present relatively strong temperature differences about 0.12 ℃. As a result, the density of all the key areas is less dense than in the Ctl 1. During this period, the RD presents a more positive difference than other regions in salinity and density, and the EA presents a unique stable character in density difference. After~7 ka BP, all the regions present a saltier bias in similar strength, about 0.21 psu. The RD, EP, NIO, SIO and WP are still colder in this period, and the rest are warmer but to a smaller extent than before the gap. The RD presents a noticeable decrease in temperature difference after ~7 ka BP. Therefore, the density differences of all the key areas are positive and present an increasing trend.

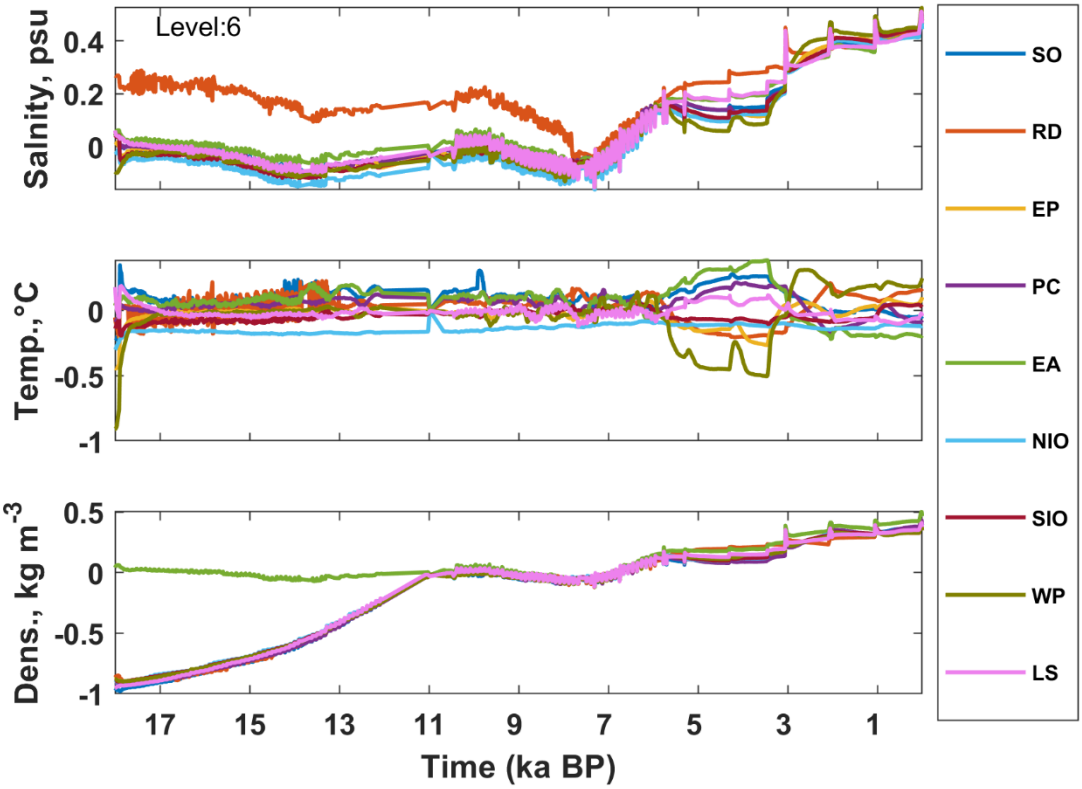

Figure 5.16 The key areas differences variation of salinity, temperature and density of the level 6 between the Ctl 1 and 2 simulations.

At level 10 (fig 5.17), the value of differences are much smaller than is the case for the shallower levels. Overall, the Ross Sea to Drake Passage presents a similar pattern in all variables as level 6. All the regions are saltier and warmer than Ctl 1 during the whole simulation. The Equatorial Atlantic is the only area that averagely is denser in Ctl 2. Before ~ 7 ka BP, all the regions still present a warmer bias, except the RD, the rest areas present a fresher bias; the density differences of all regions are larger than for the entire period. After ~ 7 ka BP, the mean salinity differences of all areas and temperature differences are positive. The North Indian Ocean presents an unique variation in this period: the NIO is cooler in Ctl 2 than Ctl 1 in about 5 ka BP, and the difference keeps increasing until the end of simulation. All the key areas present a denser bias in this period also. In general, except the early period of the EA area, all the areas present an increasing tendency in salinity and density difference.

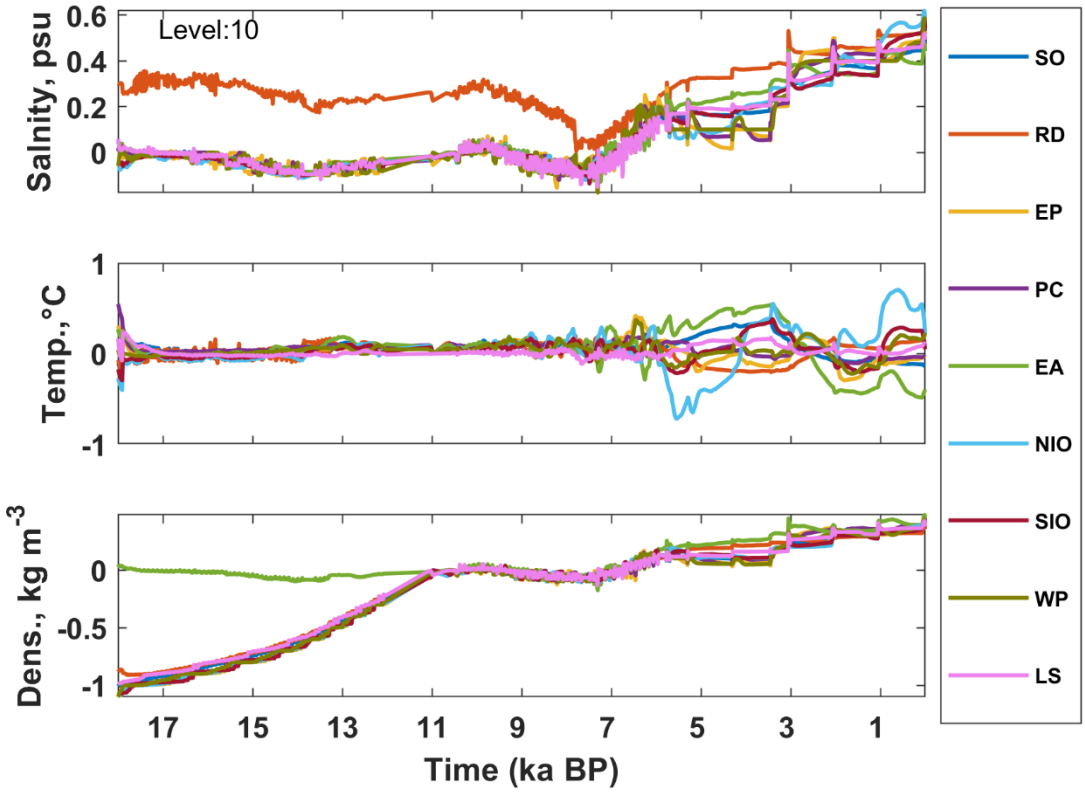

Figure 5.17 The key areas differences variation of salinity, temperature and density of the level 10 between the Ctl 1 and 2 simulations.

5.4 Discussion and Conclusions

With the varying insolation, the Ctl 2 simulation presents differences with the Ctl 1 run in the key currents of the thermohaline circulation, and presents three clearly different periods, 18-13 ka BP, 13-~6 ka BP and ~6 ka BP to 0. Among all the major fluxes, the Southern Ocean reacts to the insolation varying most sensitively. The Southern Ocean insolation variation reached a maximum at 13 ka BP and dropped to a minimum at 3 ka BP. Comparing the time frame of the key currents of the thermohaline circulation and insolation variation (fig 5.1), the insolation variation is the potential reason that caused the increase of the Southern Hemisphere Overturning annual minimum since 13 ka BP and the Southern Hemisphere Ocean ice melting at 8 ka BP.

In the horizontal distribution, the insolation variation influences on the currents at East Equatorial Pacific, Equatorial Atlantic and Southern Ocean, and strengthened the polar-tropical temperature and salinity gradient. Based on this, the varying insolation sensitive areas are located and they suggest that there is a significant difference time point during 18-0 ka BP at 8.79 ka BP. Among all the areas, those on the global thermohaline circulation path show a bigger amplitude, especially the Ross Sea to Drake Passage. Due to the surface forcing, the long-term tendency of variable differences is less obvious at level 1, but both level 6 and 10 present a similar trend. Except in the West Pacific, all the other areas have a fresher trend during 18-0 ka BP, although this trend has different strengths at different periods. After the gap at ~ 9 ka BP, the salinity and temperature difference of all the areas present a clear fresh/cool trend, and as a result, the density difference presents an increasing trend also, which might relate to the insolation variation decreasing processes.

Chapter 6 The Effects of the Closed ITF in the FRUGAL Palaeo Simulation

In chapter 5, the responses of varying insolation in the FRUGAL model are discussed. As the simulation plan shows in chapter 4, the sensitivity runs (Sen 1 and 2) are designed to examine the effect of a closed/semi-closed ITF on global oceanography. Both sensitivity runs were initialized with the restart file of the Ctl 1 simulation at 3800 years (17.2 ka BP). However, due to the resolution in FRUGAL, on the equator, the meridional space is about 1° and the zonal space is about 0.75°, and at the Southern Hemisphere the spatial resolution is coarser for the ITF region, which is about 1.5°. Therefore, the deep connections of the ITF key channels are blurred out in the bathymetry data, and resulted the raised bathymetry of both runs fully blocked all three inflows, therefore, only Sen 1 is discussed here.

In this chapter, the effect of the closed ITF in the FRUGAL palaeo-simulation will be studied. First, the impacts on the key currents of the global thermohaline circulation and ocean ice fluxes are discussed. The second discussion focuses on the effects of the closed ITF on the global oceanographic characteristics. Based on differences between the Ctl 1 and Sen2 simulations, section 6.3 focuses on the variation of hydrological characteristics of sensitive areas.

6.1 The Impact of Closed ITF on Thermohaline Circulation and Ocean Ice

Although, in the Sen 1 simulation, the Indonesian Seas are blocked, in FRUGAL the ITF flux is formally calculated by the volume difference between the volume transport from the Indonesian Seas to the Antarctica, and from Australia to the Antarctica (See 4.3). The ITF is the only tropical connection of the global thermohaline circulation, connecting the Pacific and Indian Ocean with mass and energy exchanging. Fig 6.1 shows the ITF fluxes from the Ctl 1 and Sen 1 simulations. However, as fig 6.1 shows, due to the fully shut inflows, the ITF

flux in Sen 1 is a purely local circulation that only results from local vertical circulation at the Timor Passage.

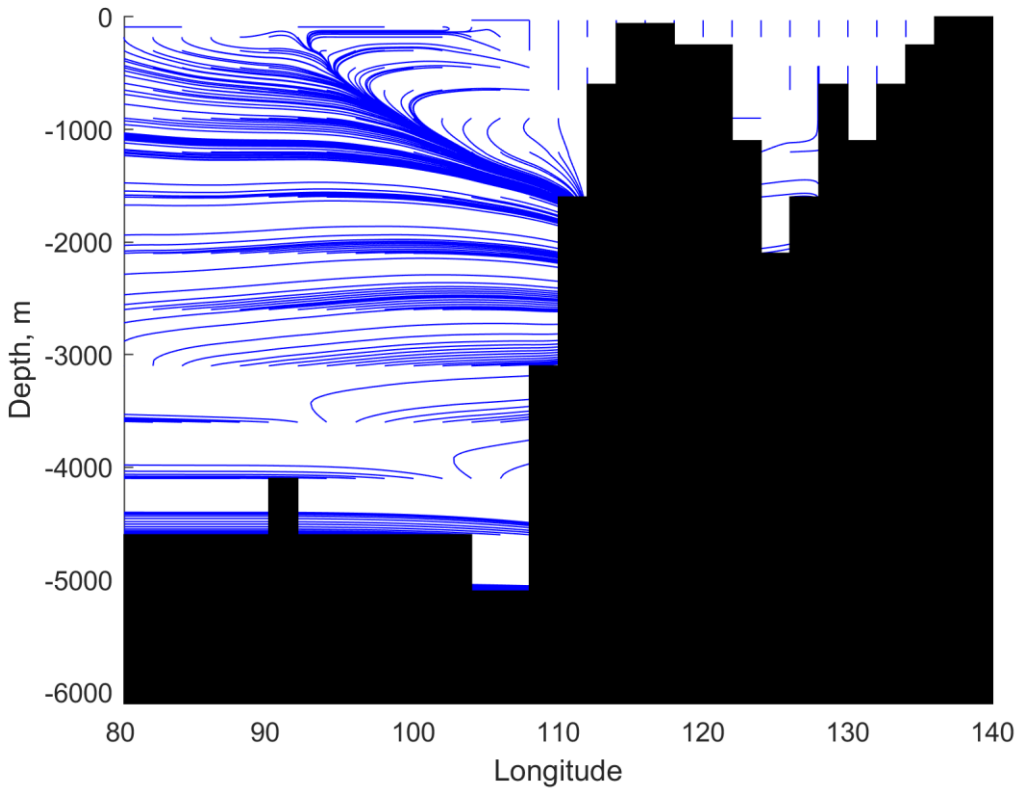

Figure 6.1 The vertical streamline through the Timor Passage (j = 50, i = 40–70; lat = 9.54°S, lon = 80-140° E) from the Sen 1 simulation.

Therefore, to quantify the effect of the ITF under the palaeoclimate background, it is essential to study the responses of other components of the global thermohaline circulation. In Sen 1 simulation, there is a spin-up about 1600 years, and this has been removed in following discussion. As fig 6.2 shows, the general strength of AMOC is noticeably weaker (mean: 16.7 ± 0.5 Sv) than in the Ctl 1 (19.7 ± 2.6 Sv); the annual variation is smaller also. The average annual maximum of AMOC is 17.3 ± 0.2 Sv, and the minimum is 15.6 ± 0.2 Sv from the Sen 1, which compares with 21.9 ± 2.4 Sv and 17.6 ± 2 Sv from the Ctl 1.

The Drake Passage flux initially responds to the closed ITF very strongly, increasing to more than 135 Sv, with a larger range of annual variation. There is then a further decline in

the annual range after ~ 13 ka BP. In contrast to the mild increasing trend in Ctl1, there is a weak decreasing trend in Sen 1. The average Drake Passage flux from the Sen 1 and Ctl 1 are 126.2 ± 8 Sv and 132.1 ± 4.5 Sv, the mean of annual maxima and minima are 131.1 ± 2.7 Sv and 122.1 ± 1.4 Sv.

The Pacific Overturning presents a stable trend, the annual maximum is close to that of the Ctl 1 run (mean of Sen 1 and Ctl 1 are 8.55 ± 2.75 Sv and 8.3 ± 3.2 Sv), but the minimum (mean: 4.3 ± 0.08 Sv) is higher in Sen 1 than Ctl 1 (mean: 3.7 ± 0.2 Sv). For the Southern Hemisphere Overturning, the amplitude is larger in Sen 1 than the Ctl 1 simulation. Comparing with the Ctl 1 run (34 ± 3.7 Sv and 11.9 ± 10 Sv), the mean of annual highest and lowest are 39.7 ± 0.3 Sv and 2.5 ± 0.2 Sv.

Fig 6.3 shows the FFT results of key currents. The Drake Passage flux presents the strongest variability, especially at multi-decadal periods; the AMOC and SHOC present similar patterns, the main periods are seasonal and annual; the PMOC shows relatively low variability, the main period being annual. Comparing with the results of Ctl 1 (fig 4.7), except the Drake Passage flux, the variability of the other fluxes is weaker in Sen 1; the SHOC is less varying in annual to multi-decadal periods in Sen 1 also. Therefore, the closed ITF weakens the Atlantic Overturning significantly and the variability of thermohaline circulation currents is affected at periods longer than seasonal cycles.

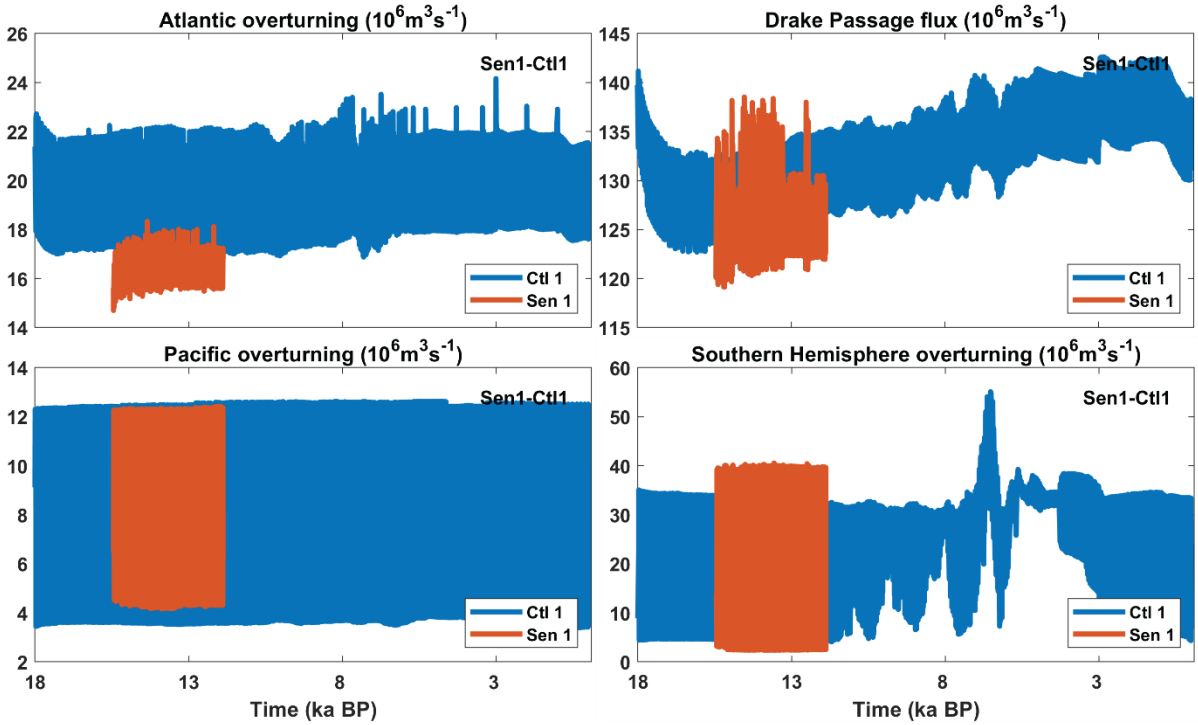

Figure 6.2 The monthly fluxes of Atlantic Overturning, Drake Passage, Pacific Overturning and Southern Hemisphere Overturning from the Ctl 1 (in blue) and Sen 1 (in orange) simulations. For the Sen 1, the spin-up has been removed, so does the fig 6.4.

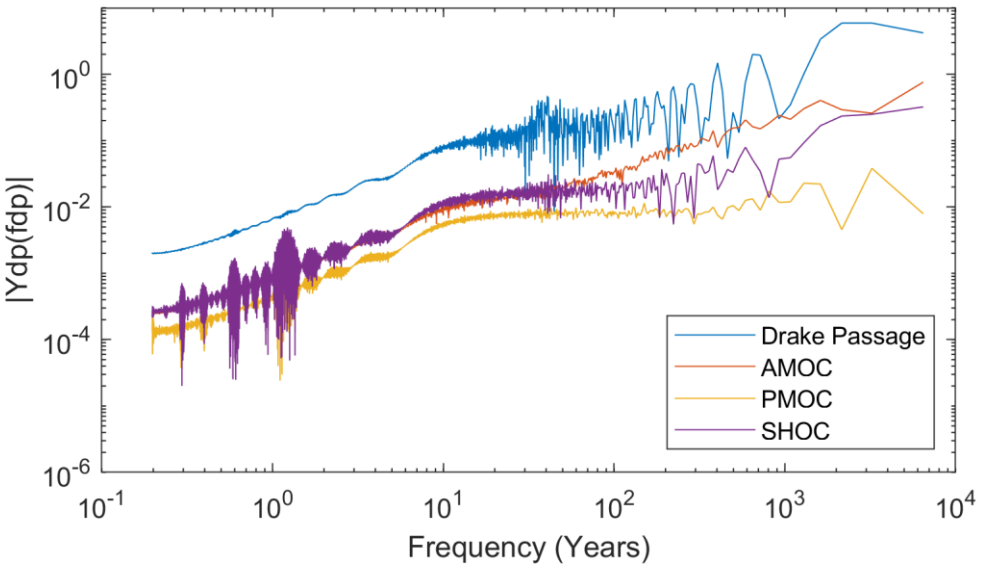

Figure 6.3 The FFT results of the Drake Passage, AMOC, PMOC and SHOC from the Sen 1 simulation.

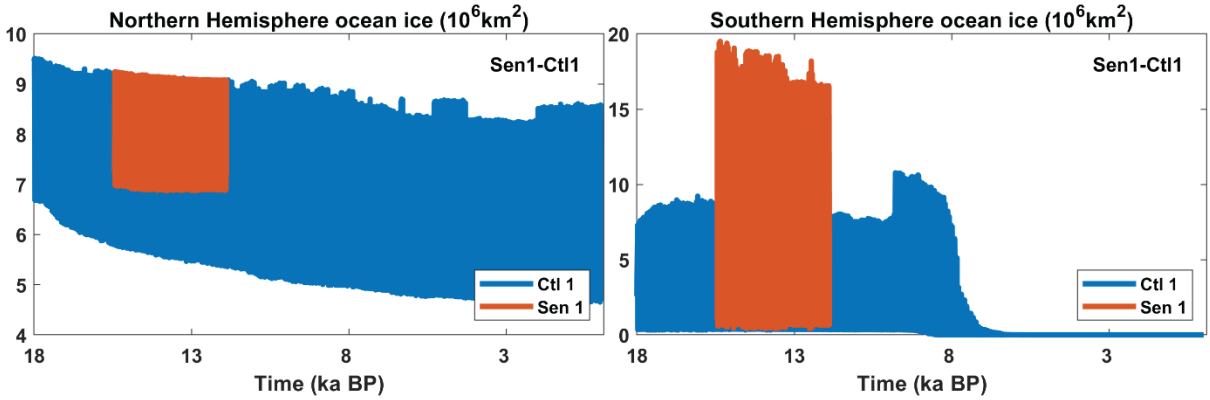

Figure 6.4 The fluxes of the Northern and Southern Hemisphere Ocean Ice from the Ctl 1 (in blue) and Sen 1 (in orange) simulations. The spin-up for Sen 1 has been removed.

Considering both hemisphere's ocean sea-ice (fig 6.4), the Northern Hemisphere Ocean Ice presents a stable trend, but unlike the Ctl 1, the annual variation is smaller, and the minimum only slightly decreases over time. The mean of the NHOI annual maximum is 9.1 ± 0.1 10^6 km^2, and the mean of the minimum is 6.9 ± 0.03 10^6 km^2. The Southern Hemisphere Ocean Ice is very different from the Ctl 1 run. The averaged SHOI is 5.8 ± 5.9 10^6 km^2 for the Sen 1 run, and the annual highest SHOI (mean: 16.2 ± 3.5 10^6 km^2) is much higher than the Ctl 1.. The annual lowest SHOI (mean: 0.6 ± 0.1 10^6 km^2) is slightly higher than in the case of the Ctl 1 simulation. Therefore, in Sen 1, the Southern Ocean is generally cooler than in the Ctl 1 simulation. In the FFT results (fig 6.5), as with fig 6.4, the variability of NHOI is very low; the SHOI presents a relatively strong variability, and the main periods of the SHOI are from seasonal to multi decadal. Comparing with the Ctl 1 simulation (fig 4.8), both of the variables present a lower variability background, especially the NHOI. The SHOI presents less variability at long periods but is strengthened at multi-decadal period.

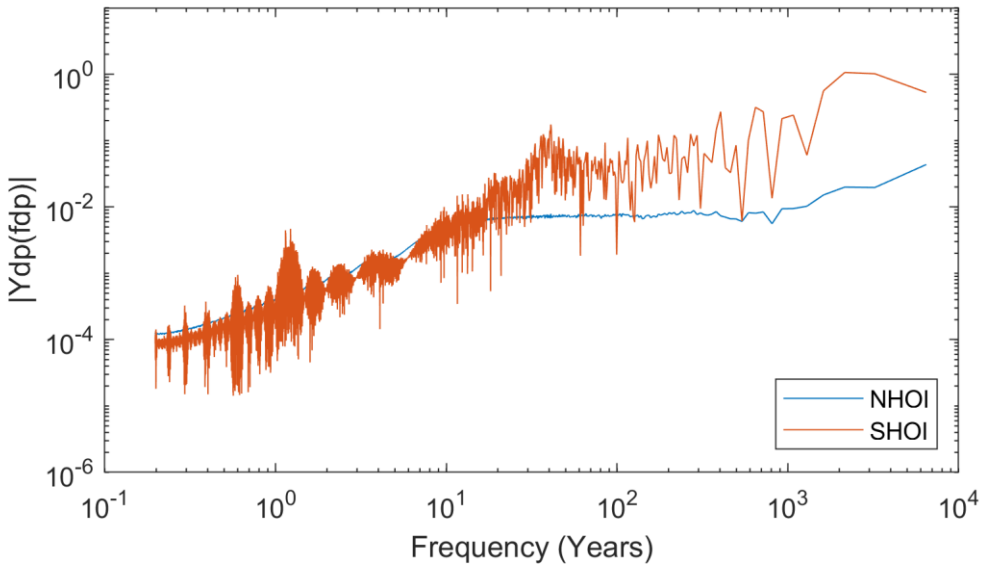

Figure 6.5 The FFT of the NHOI and SHOI from the Sen 1 simulation.

As a conclusion, in the major currents and both hemisphere's ocean sea-ice, the main effects of a closed ITF are a strongly decreased Atlantic Overturning, but a strengthened Southern Hemisphere Overturning. The Drake Passage flux and Southern Hemisphere Ocean Ice respond to the closed ITF very strongly. The annual maximum Southern Ocean ice coverage is largely increased, which suggest the closed ITF cools down the Southern Ocean.

6.2 The Impact of Closed ITF on Global Oceanographic Characteristics

As can be seen from the global thermohaline circulation response, the closed ITF affects the ocean globally. Fig 6.6 presents the global currents, sea temperature and salinity difference distributions between the Ctl 1 and Sen 1 simulations at FRUGAL's level 2, 30 m depth. For the horizontal current (fig 6.6(a)), the most significant differences are the strengthened Equatorial countercurrent in the East Pacific and weakened Atlantic Equatorial Current. Due to the closed ITF, the Equatorial West Pacific presents a weak eastwards bias, and the South Pacific Equatorial Current is forced to increase along the east coast of Australia, therefore, the Pacific part of the ACC is strengthened. There is a cyclonic trend in the Ross Sea instead of a westward current bias to the south of Australia. As a result, the

Indian Ocean has less supply from the Pacific at this level. The Indian Ocean Equatorial Current and the Agulhas current are weaker in Sen 1.

In the Atlantic Basin, the Labrador Sea allows more water into the Arctic and North Atlantic, the Mediterranean outflow is stronger, and the North Atlantic Equatorial Current is weaker but the South Atlantic flow is stronger in the Sen 1 run. The transport via the Drake Passage is slightly stronger in Sen 1 and there is a cyclonic trend at the Weddell Sea too. The North Pacific, South Indian Ocean, and the Equatorial and South Atlantic present a weak downwelling bias.

In the temperature difference distribution (fig 6.6(b)), except for part of the Arctic, Southern Ocean and Mediterranean, the temperature is warmer in Sen 1 run than Ctl 1. The North Atlantic is significantly warmer in the Sen 1 simulation, due to the reduced Atlantic Overturning bringing less deep cold water to the subsurface. As a result of the blocked ITF, the North Pacific is relative warmer than other areas also. As the ITF is blocked, due to the weakened Agulhas Current and a warm pool at the Southern Indian Ocean, the Indian Ocean is not able to output as much energy to the Atlantic as in Ctl 1. Moreover, the weakened AMOC suggests a weakened heat transport also. Therefore, the Indian Ocean is warmer in the Sen 1 simulation. For the Mediterranean, the increased outflow transports more heat into the North Atlantic, therefore, the Mediterranean sea temperature is colder in Sen 1.

In the salinity difference distribution (fig 6.6(c)), the Sen 2 is fresher than the Ctl 1 run globally, especially in the Mediterranean, Weddell Sea, Arctic and South Pacific. Comparing with the temperature difference distribution, the fresh bias areas relatively match the cool bias areas.

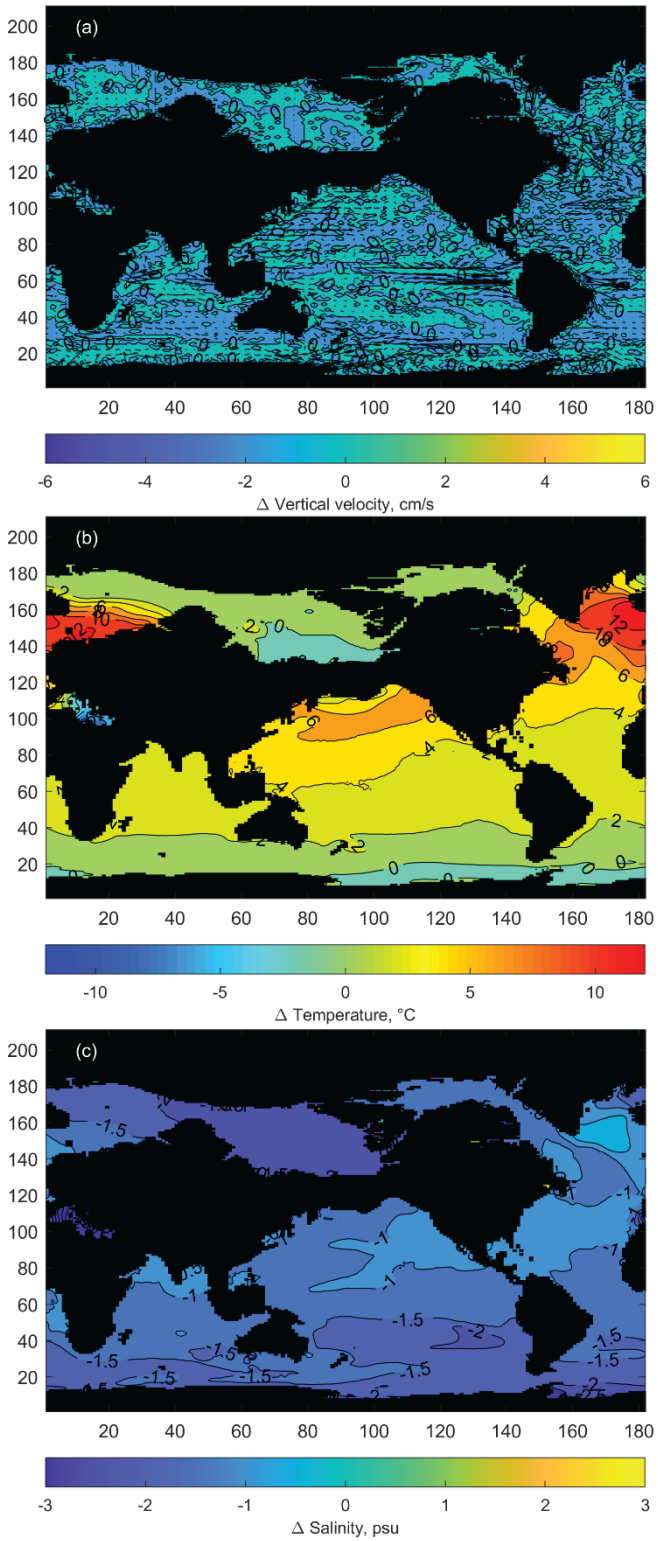

Figure 6.6 The difference distributions of (a) the horizontal currents (in vector) and vertical velocity (in contour; cm/s), (b) the sea temperature (°C) and (c) salinity (psu) between Ctl 1 and Sen 1 simulations at level 2 (depth:30 m).

For middle layers, level 6 (fig 6.7, depth: 450 m) is chosen as the representative level. In the horizontal current difference distribution (fig 6.7(a)), in the Pacific basin, in the Sen 1 run, the equatorial sub-countercurrent is stronger in the East and Central Pacific; due to the closed ITF, an eastwards current bias appears in the West Equatorial Pacific; the Antarctic Circumpolar Current and Antarctic Coast Current are stronger in the Southern Pacific. As a result of the closed ITF, the North and Equatorial Indian Ocean present an eastward bias.

In the Atlantic, the Northern Atlantic current presents a significant northward bias across the central to eastern region, and a southward current bias along the western boundary. A southward current difference appears at the South Atlantic eastern coast. Most of the North Atlantic presents a downwelling bias; the West and East Equatorial Pacific present downwelling and upwelling biases respectively.

In the temperature difference field (fig 6.7(b)), similar to the case at level 2, the Sen 2 simulation is globally warmer than the Ctl 1 run. Because of the closed ITF, heat is trapped in the North Pacific and the weakened Atlantic Overturning brings less cold water from deeper layers, as fig 6.2 shows. Therefore, in general, the temperature difference is higher in the Northern Hemisphere than the Southern Hemisphere: the Mediterranean, North Atlantic, Arctic and North Pacific.

For the salinity differences (fig 6.7(c)), the Sen 1 is globally fresher than the Ctl 1 simulation, especially the Southern Ocean and the South Pacific; the Equatorial and North Atlantic, Mediterranean, North Indian Ocean, and the Timor Sea is relatively close to the Ctl 1 result.

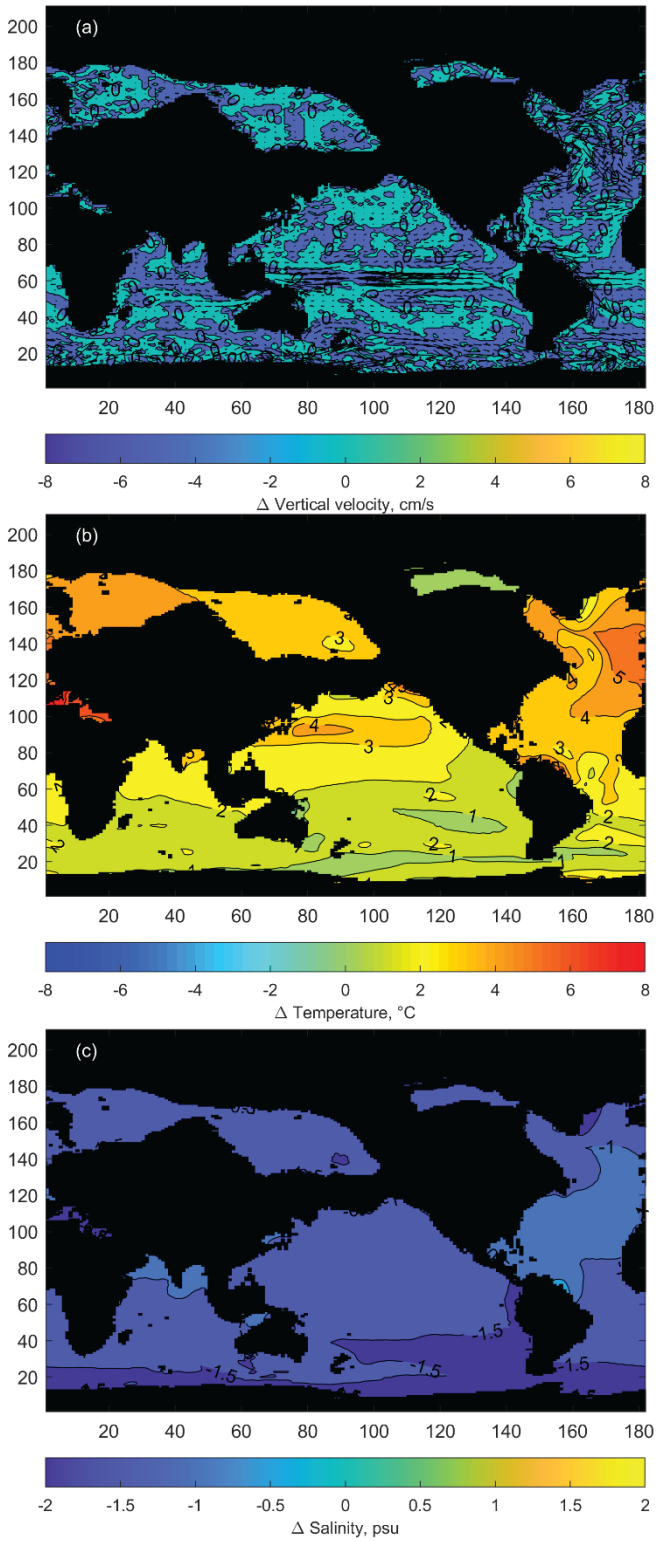

Figure 6.7 The difference distributions of (a) the horizontal currents (in vector) and vertical velocity (in contour; cm/s), (b) the sea temperature (°C) and (c) salinity (psu) between the Ctl 1 and Sen 1 simulations at level 6 (depth: 450 m).

To represent the deep layer, the difference distributions at level 10 (1600 m) are shown in fig 6.8. In fig 6.8(a), the westward and eastward current biases are found in the East Equatorial Pacific and north of it. The Ross Sea has a strong westward coastal current bias and relatively weak eastward ACC current bias. In the Atlantic, there is a mild northward trend along the Atlantic eastern boundary to the Labrador Sea and a strong southward trend from the Labrador Sea into the Northern Atlantic along the western boundary; there is also a weak eastward trend in the northern Equatorial Atlantic. The Weddell Sea presents a strong eastward coastal current bias too.

The temperature difference distribution (fig 6.8(b)) presents a global warmer trend at level 10 again, but with a smaller value. The Sen 1 temperature is closer to Ctl 1 in the Southern Ocean, especially the Ross Sea. The Mediterranean, Arctic and North Atlantic is much warmer in Sen 1 than Ctl 1. The warmer bias distribution matches the horizontal current distribution: there is more water sent to the Northern Atlantic along the east coast, which returns along the west coast. In the salinity difference fields (fig 6.9(c)), the Sen 1 is globally fresher than the Ctl 1, and the difference is larger in the Southern Hemisphere than the Northern.

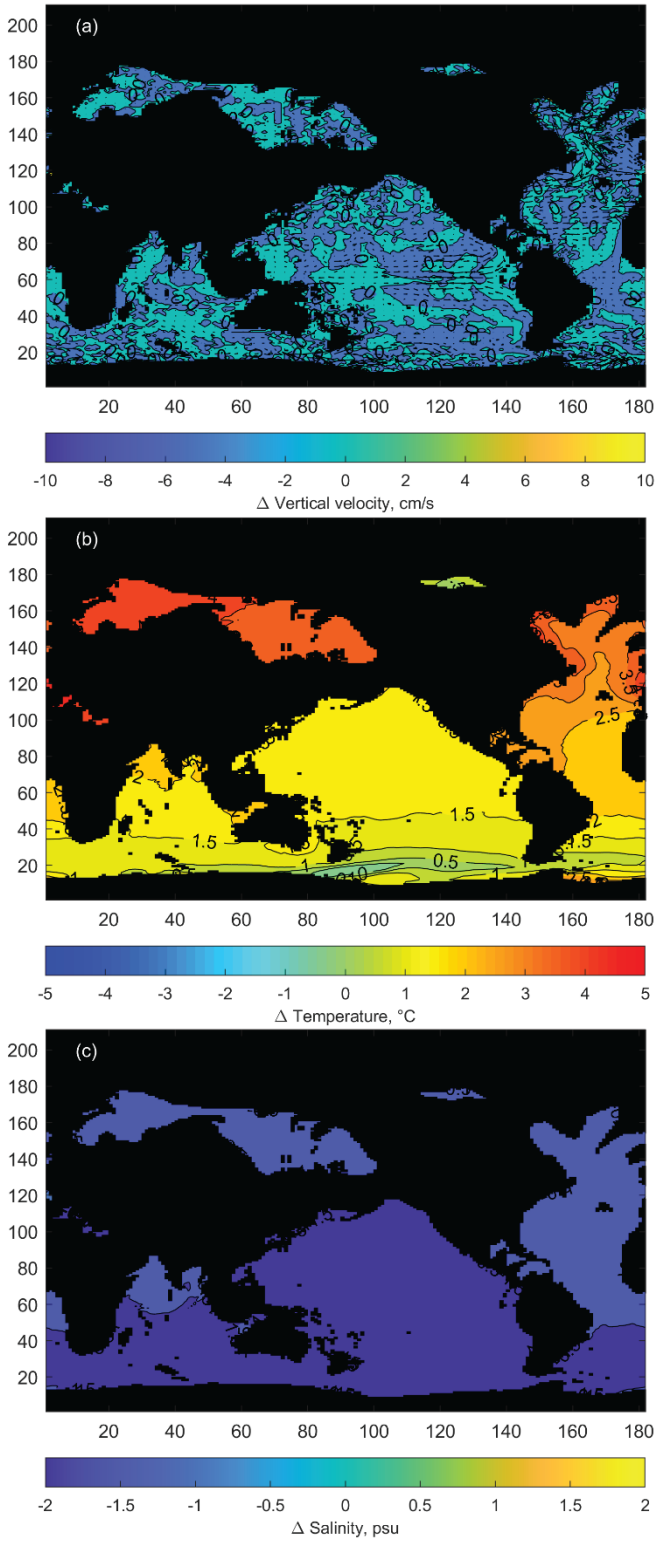

Figure 6.8 The difference distributions of (a) the horizontal currents (in vector) and vertical velocity (in contour; cm/s), (b) the sea temperature (°C) and (c) salinity (psu) between the Ctl 1 and Sen 1 simulations at level 10 (depth: 1600 m).

In general, in subsurface, middle and deep levels, the East Pacific, North Atlantic, Mediterranean and Southern Ocean respond to the closed ITF most significantly. The West Pacific is most sensitive to the closed ITF at the middle layer. Because of the reduced Agulhas Current, heat is trapped in the Indian Ocean, causing a warming trend. The closed ITF weakens the Atlantic Overturning, and so the Atlantic reacts strongly in both current and temperature difference distributions. The Pacific part of the Southern Ocean is responsible for compensating for the shut ITF, therefore showing high sensitivity. In the following section, these areas will be focused on studying the responses to the closed ITF over time.

6.3 The Impact of Closed ITF on Sensitive Areas

Based on the difference fields of subsurface, middle and deep layers, the sensitive areas to a closed ITF are selected and presented in fig 6.9.

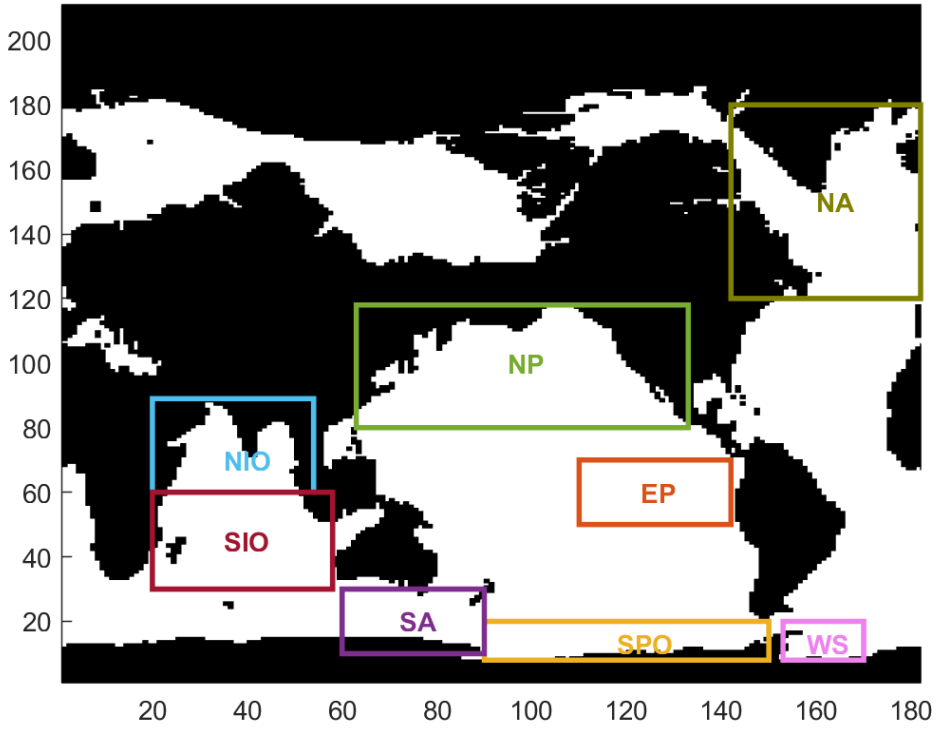

Figure 6.9 The sensitive areas of closed ITF in Sen 1 simulation topography. NP: North Pacific; NA: North Atlantic; NIO: North Indian Ocean; SIO: South Indian

Ocean; EP: East Pacific; SA: Southern Ocean Australia; SPO: Southern Pacific Ocean; WS: Weddell Sea. The areas are decided based on the result in section 6.2, and different from chapter 5.

Fig 6.10 shows the regional differences of salinity, temperature and density between the Ctl 1 and Sen 1 simulations at Level 2 (depth: 30 m), averaged over the Sen 1 simulation period. For the salinity, all the regions present a decreasing trend in salinity difference. Except for the North Pacific and the South Indian Ocean, which are slightly saltier about 0.56 ± 0.14 psu and 0.1 ± 0.11 psu in Sen 1 run overall, the other areas are fresher in Sen 1 at this level. There is an increased salinity difference at ~13.5-13 ka BP in the Weddell Sea only, from about -0.7 psu to -0.14 psu, and a decreasing trend after 12.5 ka BP is milder than the others also. Among all the regions, the closed ITF make the North Indian Ocean and Weddell Sea cooler (-4.95 ± 0.1 ℃ and -0.02 ± 0.4 ℃), and the rest warmer. The result of the Indian Ocean cooling corresponds to modelling results under present-day climate (Santoso et al., 2011; Song et al., 2007). The North Atlantic and East Pacific are warmed most by the closed ITF, at 4.66 ± 0.25 ℃ and 3.3 ± 0.16 ℃ in general. The temperature difference of the Weddell Sea presents a similar trend between ~13.5-12.5 ka BP but this is less noticeable than the salinity difference The density differences of all the areas show a decreasing trend. Within all the areas, only the North Indian Ocean is slightly less dense, the rest are denser in Sen 1 than Ctl 1.

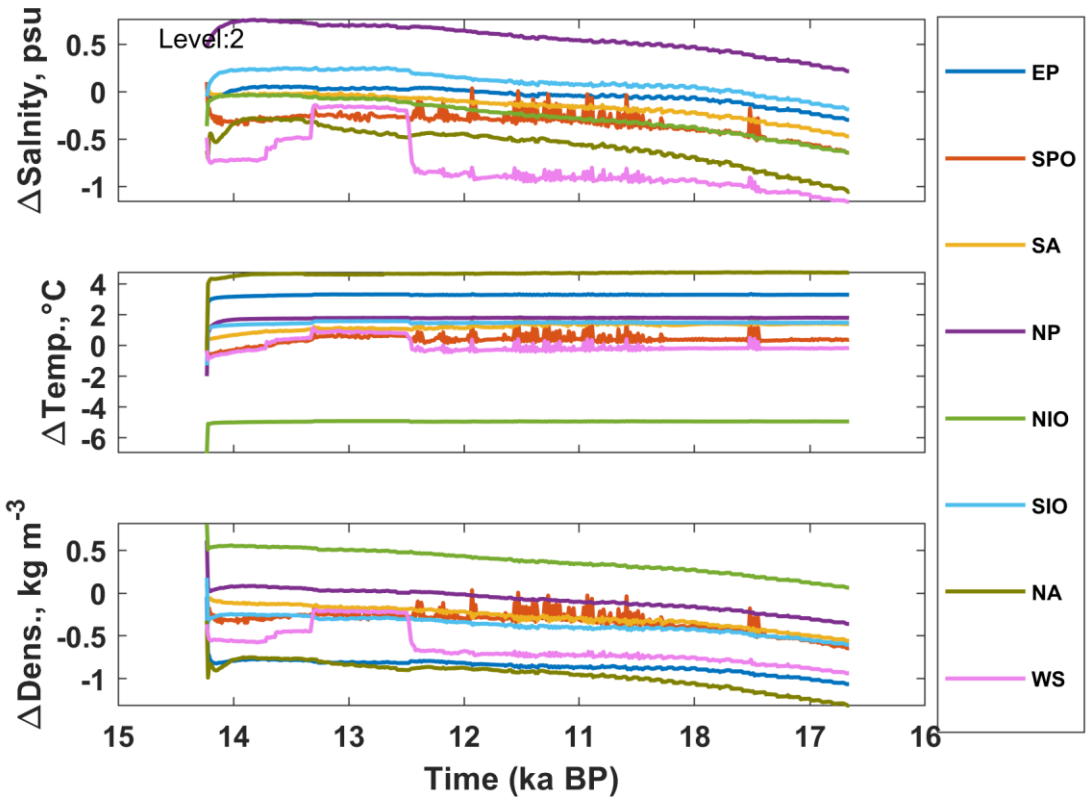

Figure 6.10 The key areas differences variation of salinity, temperature and density of the level 2 (depth: 30 m) between the Ctl 1 and Sen 1 simulations.

At the middle level (fig 6.11), for the salinity difference, besides the sudden change from the Ctl 1 simulation, there is a mild but noticeable decreasing tendency in all regions. The South Indian Ocean and Weddell Sea show a very small increase during ~13.5-12.5 ka BP. The average salinity of most areas is slightly smaller (~0.1 psu) in Sen 1, but the North Indian Ocean (-0.56 ± 0.18 psu) is relatively much fresher in Sen 1. The North Pacific is generally saltier at this level in Sen 1 (0.39 ± 0.14 psu). For the temperature difference, the North Indian Ocean is cooler in Sen 1 (about 5.44 ± 0.1 ℃); the remaining areas are slightly warmer in Sen 1. Similar to the case at level 2, the temperature difference presents a stable long term variation, except for a gentle valley between ~13.8-12.5 ka BP in the Weddell Sea. Therefore, at level 6, the density differences of key areas presents a decreasing tendency. The

North Pacific and North Indian Ocean are denser in Sen 1 in the middle layer, and the other region s are less dense.

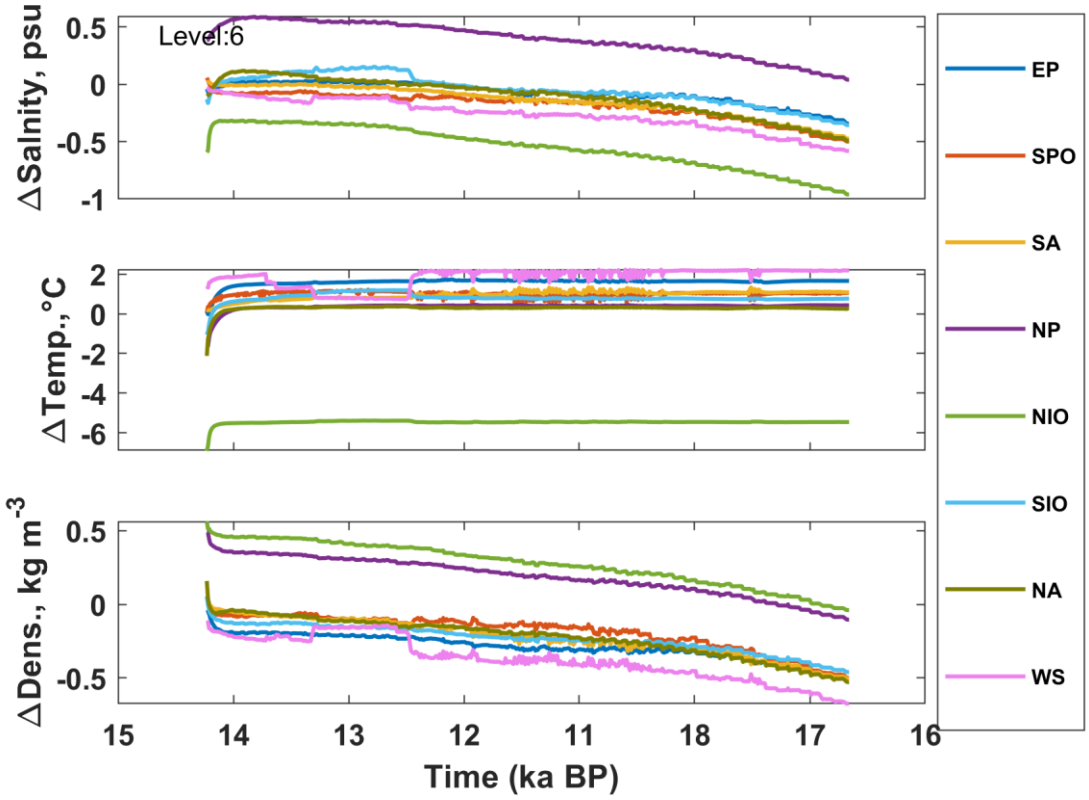

Figure 6.11 The key areas differences variation of salinity, temperature and density of the level 6 (depth: 450 m) between the Ctl 1 and Sen 1 simulations.

In the deep layer (fig 6.12), the scales of all differences are smaller than at the subsurface and middle layers. Among all the regions, the North Indian Ocean (-0.42 ± 0.18 psu) and North Atlantic (-0.33 ± 0.17 psu) are relatively more fresher than other areas in Sen 1. For temperature differences, the North Indian Ocean (-2.87 ± 0.24 ℃), North Atlantic (-1.12 ± 0.2 ℃) and North Pacific (-0.28 ± 0.25 ℃) are colder in Sen 1 at level 10, the rest are warmer. The decreasing trend is more obvious in density differences. All the regions are less dense in Sen 1 than Ctl 1 at this level.

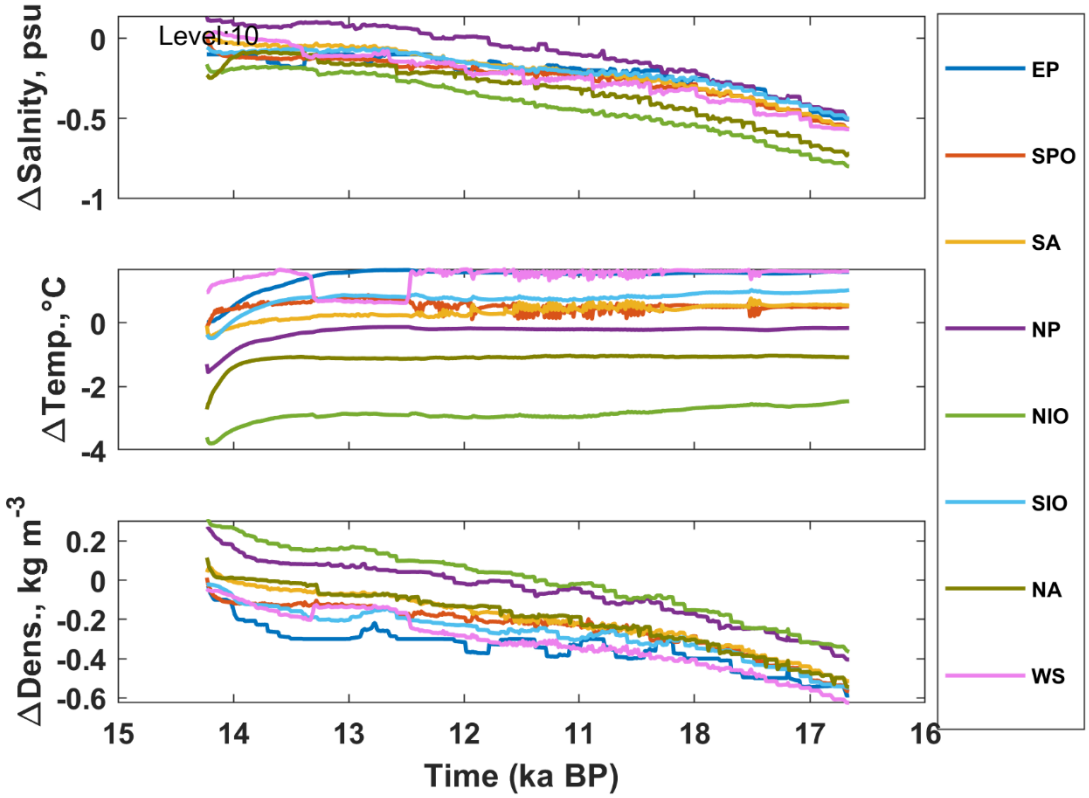

Figure 6.12 The key areas differences variation of salinity, temperature and density of the level 10 between the Ctl 1 and Sen 1 simulations.

6.4 Discussion and Conclusions

After the ITF is closed, the global thermohaline circulation reacts strongly. The local ITF flux is not zero in Sen 1 simulation, due to the local vertical circulation at the Timor Sea. However, comparing with the Ctl 1 simulation, the Atlantic Overturning weakened significantly; the Drake Passage flux responds to the sudden closure of ITF strongly also; the seasonal variation weakened in Pacific Overturning but strengthened in Southern Hemisphere Overturning. As a result, the Northern Hemisphere Ocean sea-ice shows a smaller seasonal change, but the Southern Hemisphere Ocean sea-ice presents a negative variation, linked with the Drake Passage flux. This suggests that the Southern Ocean responds to the ITF supply very sensitively.

For different levels of the global ocean, the closed ITF shows important local and remote influence under the palaeo-background (fig 6.13). The east and west Equatorial Pacific present opposite current differences due to the closure of the ITF, as the eastward branch at the Equatorial Pacific in fig 6.13(b). Without the direct tropical connection, the North Pacific accumulates heat and becomes warmer in Sen 1 than Ctl 1, while the North Indian Ocean is cooler. As a compensation, there is a westward current bias in the Southern Ocean south of Australia at all the subsurface to deep levels, fig 6.13(b), to transport mass and heat from the Pacific to the Indian Ocean. Therefore, the Southern Indian Ocean is warmer in the Sen 1 than Ctl 1 simulation. However, as fig 6.13 shows, the Agulhas Current is weaker in Sen 1 also, and causes a weaker transport to the Atlantic, which lets the Southern Indian Ocean trap more heat and gives rise to a generally warmer tendency in fig 6.6-6.8. This also is the reason for the reduced Atlantic Overturning. The Southern Ocean, especially the Southern Pacific Ocean, and North Atlantic reflect the change of ITF strongly in horizontal current and temperature fields also. The general north-south difference in both temperature and salinity difference distributions might be due to the FRUGAL grid resolution, which is finer in the Northern Hemisphere than Southern (fig 4.1). For the time variation, the closed ITF is freshening and lightening all the sensitive areas slowly but the temperature difference presents a stable variability. In the vertical, the shallower levels presents larger differences than the deep.

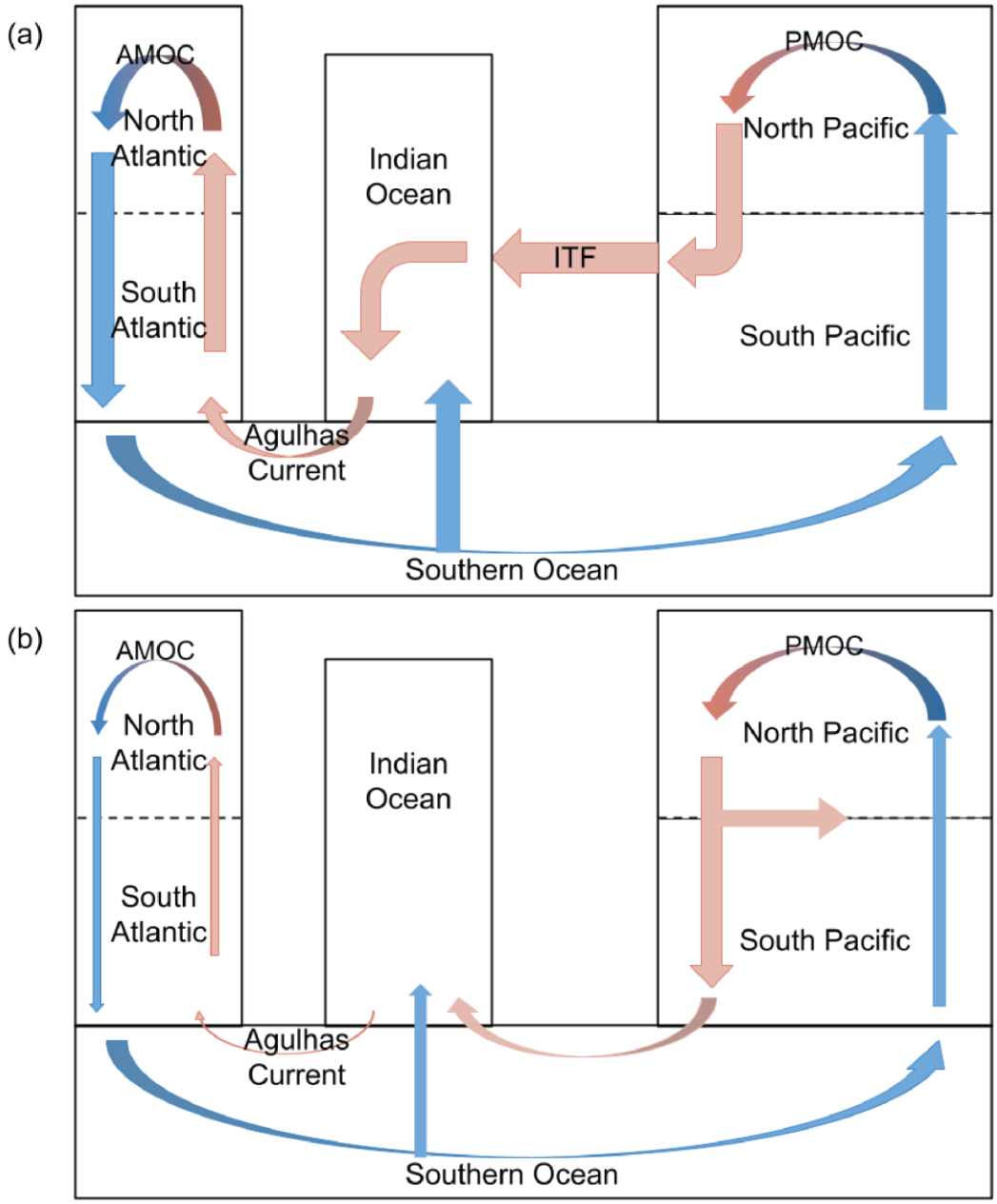

Figure 6.13 The diagram of the global thermohaline circulation (a) with the ITF as Ctl 1 simulation and (b) without the ITF as the Sen 1. The red arrows indicate the warm path, and blue for the cold path. AMOC: Atlantic Meridional Overturning Current; PMOC: Pacific Meridional Overturning Current.

The next chapter is the summary of the completed thesis. In chapter 7, the main conclusions of each work will be summed up, and the connection between them will be discussed. The considered limitations and potential further work will be discussed also.

Chapter 7 Summary

This thesis studies the ITF in both the modern and palaeo background. In the contemporary mode, the interannual variability of the ITF and the behaviour of the local flows is investigated. This developed into study of the vertical structure of the ITF transport and the potential factors that affect it. The long term, and geographically distant, influences of the ITF on the global thermohaline circulation are investigated in the palaeoclimate background.

7.1 The Summary of the Contemporary Research

Using the SODA reanalysis dataset, the ITF volume transport was calculated by the sum of the three main inflows to it: the Makassar Strait, Lifamatola Strait and Karimata Strait. The mean ITF transport during 1980 to 2016 was 12.76 ± 2.74 Sv. This result can be compared with the mean ITF transport as found by various observation programmes. From INSTANT (Sprintall et al., 2009) the ITF mean is 15.07 Sv, using mooring observation at the three main outflows (Lombok, Ombai and Timor Straits). The mean transport via the Makassar Strait from the MITF program (Gordon et al., 2012) is 10.52 Sv, 10.1 Sv, 8.63 Sv and 10.16 Sv respectively for the four periods monitored. In addition, a proxy calculated by satellite data (Susanto and Song, 2015) has an average ITF transport of 11.51 Sv. The ITF volume transport calculated in this thesis is slightly smaller than the INSTANT due to its extreme values, but higher than MITF, because the MITF only collected the mooring results from the Makassar Strait, and is similar to the proxy data in general (fig 7.1). The ITF transport in this thesis is longest in time scale among all the data listed in fig 7.1. The variation of ITF transport in annual and sub-decadal is significant, but there is not a long term trend of the magnitude.

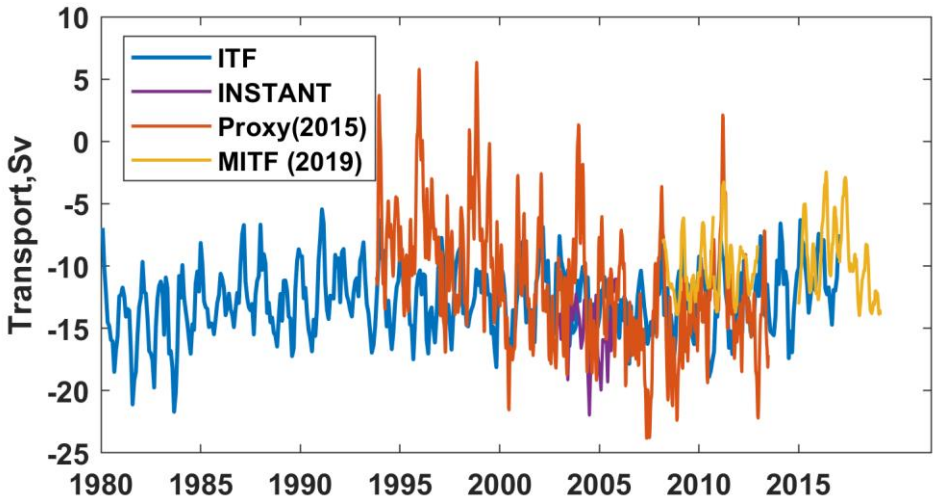

Figure 7.1 The monthly ITF transport variation (unit: Sv). The SODA reanalysis data in blue and the INSTANT data in purple, proxy data in orange and MITF data in yellow.

The relationship between the ITF and ENSO was investigated by composite analysis. The results suggest that in the El Niño years the wind field constrains the water supply into the Indonesian Seas by weakening both the Mindanao Current and the New Guinea Coastal Current (NGCC) from the North and South Pacific respectively. Consequently, the ITF transport is weaker in El Niño than La Niña.

The surface sea salinity and temperature over the ITF region are significantly positively correlated with the Nino 3.4 index, which suggests that the combinations of warm and saltier water or cold and fresher water appears at the ITF region at the same time. This result matches with the hypothesis that there are two main water sources for the ITF: the North Pacific water via the Mindanao Retroflection and the South Pacific water from the Halmahera Retroflection (Gordon and Fine, 1996; Koch-Larrouy et al., 2008; Valsala et al., 2010).

Beyond the seasonal variation, the most significant transport pathway prevailing over the whole year in the Indonesian Seas is from the Mindanao Current to the Celebes Sea and

via the Makassar Strait to the Lombok Strait. The second main pathway is from the New Guinea Costal Current to the ITF via the Lifamatola Strait, and the third inflow path is from the South China Sea to the Java Sea via the Karimata Strait. The NGCC is relatively stronger in the boreal spring and autumn than in the other two seasons. Due to the strong winter monsoon, the flow via the Karimata Strait strengthens and the Lifamatola Strait becomes the secondary inflow. The interannual transport variation match the monsoon field variation well (see section 2.3.2, fig 2.7).

The vertical structure of the ITF horizontal transport was studied and a shift was found during the 1990s. This was identified as occurring in the Banda Sea. This change was investigated with a box model of the Banda Sea basin. As an ideal physical ocean model, this model achieves a steady state on a decadal time scale. A set of sensitivity simulations were carried out. The results indicate that the water source of the Banda Sea plays an essential role in the vertical distribution of the horizontal transport. The water supply of the Banda Sea, namely the ITF, is constructed by the Mindanao Current from the North Equatorial Pacific, the New Guinea Coastal Current from the South Equatorial Pacific, and the South China Sea inflow (fig 7.2). The box model results suggest that the increased water supply from the South China Sea to the Banda Sea would change the vertical structure of the horizontal transport with a prolonged effect. Although the potential reason of this shift is analysed in this thesis, the reason of the change in water supply ratio is not certain. The possible explanation might be the rapid alternating change of ENSO phase during the same period of the 1990s.

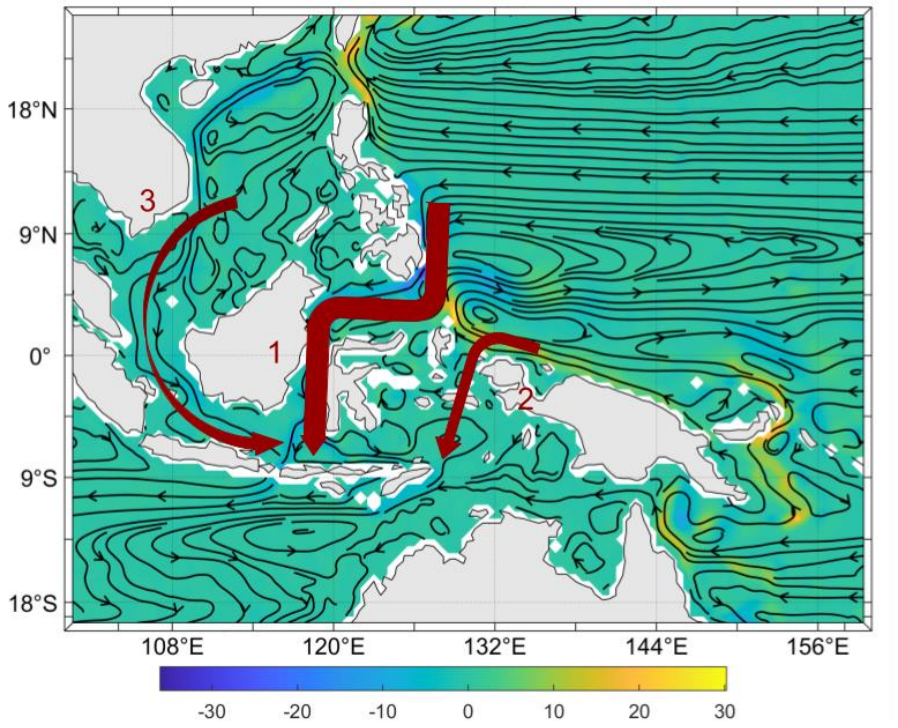

Figure 7.2 The average current (in streamline) and volume transport (in contour; unit: Sv) calculated from SODA reanalysis dataset. The paths of the ITF inflows: (1) Mindanao Current- Makassar Strait-Java Sea; (2) South China Sea-Karimata Strait-Java Sea; (3) New Guinea Coastal Current-Lifamatola Strait-Banda Sea.

7.2 The Summary of Palaeo Modelling

The portion of this thesis within a modern climate background focuses on the characteristics of ITF itself, but the palaeo-research emphasises the ITF's global effects. The FRUGAL model was chosen here, as it has been used for palaeo-modelling in many palaeo studies (Bigg and Wadley, 2001; Wadley and Bigg, 2002; Bigg et al., 2012; Starr et al., 2021; McCarron et al., 2021). Comparing with other ocean general circulation models, the North Pole is located in central Greenland instead of the Arctic. Therefore, FRUGAL has a finer spatial resolution in the Northern Hemisphere and Equatorial regions with a better simulating capacity of essential elements, such as the AMOC and ITF, and a relatively efficient

simulation speed. There are two LGM control runs: the Ctl 1 simulated the natural variability in FRUGAL, and the Ctl 2 simulated the insolation-related component of the deglacial process. By comparing the Ctl 1 and 2 simulations, it was seen that the varying insolation is likely to have caused the strengthening of the Southern Hemisphere Overturning at about 8 ka BP, which is consistent with proxy data from ocean core (fig 3c in Anderson et al., 2009). Considering the upper ocean horizontal current distribution, the insolation variation of Ctl 2 affects the currents of the East Equatorial Pacific, Equatorial Atlantic and Southern Ocean, and strengthened the polar-tropical temperature and salinity gradient. After 9 ka BP, the varying insolation freshens and cools all the insolation-sensitive areas. The variation of Southern Ocean and sensitive is consistent with the insolation variation.

Sensitivity runs were carried out to understand the impact on the global circulation of the shallowing of the Indonesian Seas during the glacial and early deglacial period. In simulation Sen 1, the bathymetry was uplifted by 2 vertical levels for all the grids within the Indonesian Sea, and further changed to dry land in simulation Sen 2. However, both of these runs leave the ITF inflows fully blocked. Therefore only the Sen 1 result is discussed in this thesis.

Although the ITF is fully closed, the local vertical circulation in the Timor Sea makes the local ITF flux appear non-zero. By comparing the Ctl 1 and Sen 1 simulations, several important ocean changes were observed. The closure of the ITF highly reduced the Atlantic Overturning by forcing the Pacific feeding the Indian Ocean via the Southern Ocean and weakening the Agulhas Current; the Drake Passage presents a significant response to the sudden closure of ITF; the seasonal variation weakened in Pacific Overturning but strengthened in Southern Hemisphere Overturning. In addition, the Northern Hemisphere Ocean sea-ice coverage shows a reduced annual change. The coverage of Southern

Hemisphere Ocean sea-ice shows a negative relationship with the Drake Passage flux, which suggests the Southern Ocean is highly sensitive to the ITF connection.

Under the palaeo-climate background, the closed ITF leads to other impacts also. Due to losing the ITF connection, the East and West Equatorial Pacific presents opposite current trends, and there is forced water flow into the Indian Ocean via the Southern Ocean south of Australia. As a result, the Southern Ocean is warmer after the ITF closed. In addition, the Agulhas Current is weaker, and therefore, the Indian Ocean traps more heat in Sen 1 than in the Ctl 1 run. The reduced supply from the Indian Ocean to Atlantic leads to a decline in the Atlantic Overturning, and decreases the deep cold water upwelling to the surface and generated a warmer bias in the Northern Atlantic (fig 6.13).

According to the reconstructed sea level from palaeo-data, both the Sunda and Sahul shelf were exposed at the LGM (Di Nezio et al., 2016). As fig 1.5 shows, the ITF was restricted to flow through the Makassar Strait and Timor Passage. Thus, due to the globally sea level drop (Peltier and Fairbanks, 2006; Yokoyama et al., 2000), the ITF transport was highly reduced but not fully shut down during the LGM (Xu, 2014; Di Nezio et al., 2016; Fan et al., 2018). The LGM simulation suggests that the ITF volume transport is reduced by 20 % (Shin et al., 2003), or 1.5 Sv by only the Indonesian Seas' bathymetry adapting to LGM (Di Nezio et al., 2016). The sensitivity simulations carried out here, therefore, are likely to be an extreme case, although compatible with the model horizontal resolution. However similar to what was found in the Sen 1 results, both modelling (Zhang and Prange,2020) and palaeoceangraphic data (Oppo et al., 2015), suggest the Atlantic Overturning weakened but remained active during the LGM. Moreover, the sediment datasets (Franzese et al., 2006) suggests the Agulhas Current weakened at the LGM also. Furthermore, modelling has suggested the increased mass transport from the Indian Ocean to the Atlantic associated with the beginning of the flooding of the Indonesian Seas triggered the deglaciation (Knorr and

Lohmann, 2003). By adapting the LGM bathymetry in ITF region, the modelling studies suggests a warmer condition at the west Indian Ocean and cooler at east Indian Ocean (Di Nezio et al., 2016). The glacial simulation with LGM boundary results show that the thermohaline circulation was shallower and weaker globally, and the Antarctic Circumpolar Current was more than 50% stronger in LGM than present (Shin et al., 2003). Other LGM modelling results agree with the weaker AMOC and fresher North Atlantic also (Kim et al., 2002; Menviel et al., 2011; Zhang and Prange, 2020).

7.3 the Limitations

The challenge of this work includes the natural complicated bathymetry of the Indonesian Seas. This increases the difficulty of numerical simulations. The topography in most models is not detailed and realistic enough compared with reality. On the other hand, there are plenty of observational datasets for the ITF (Gordon et al, 1999, 2003, 2008; Kashino et al., 1999; Susanto and Song, 2015), but most of them are collected from moorings deployed for only a few years, or calculated by satellite data which are constrained to a surface view. Although, the reanalysis dataset chosen in this thesis combined both modelling and observational results, the reliability can be improved if a long term observation dataset was available.

Another challenge in this work is the time cost of the palaeo-modelling. Although the grid resolution in FRUGAL helps resolve the key circulation components, the simulation computational time of the control runs still costs more than three years of real time. Therefore, there was not a second chance to adjust the control run, and end with a relatively long spinup. The sensitivity simulations could have been expanded but they had to be initialised before the control run end.

7.4 Future Work

The possible future work includes a further study of the specific mechanisms that control the ITF water sources and their division. The potential reason that led to the increasing water supply from the Southern China Sea to the ITF during 1993 to 2000, could be the rapid alternating ENSO phase. If the link between the ENSO phase to the ITF water source could be clarified, it could lead to a new understanding of the ENSO influence and the hydrological relationship between the different basins in the Indonesian Seas. To achieve this, the ITF needs further monitoring also, but currently observation of the ITF relies on short term projects. One approach is observing the ITF by satellite, but the limitation of neglecting deeper hydrology is difficult to overcome. In the palaeo simulation, the Sen 2 has the same performance as the Sen 1 run, due to the difference between real and model bathymetry. I believe that improving the reconstructed LGM bathymetry precision would benefit the design of sensitivity simulations, and allow a simulation with the narrow ITF of the LGM sea level.

References

Ahmad, A. L., Syamsuddin, M. L., Purba, N. P., & Sunarto. (2019). Thermal front condition through El Ni?o and Indonesian throughflow phase in southern sea of East Java and Bali on the east monsoon. *IOP Conference Series: Earth and Environmental Science*, *303*(1). https://doi.org/10.1088/1755-1315/303/1/012002

Anderson, R. F., Ali, S., Bradtmiller, L. I., Nielsen, S. H. H., Fleisher, M. Q., Anderson, B. E., & Burckle, L. H. (2009). Wind-driven upwelling in the southern ocean and the deglacial rise in atmospheric CO2. *Science*, *323*(5920), 1443–1448. https://doi.org/10.1126/science.1167441

Australian Bureau of Meteorology, Indian Ocean influences on Australian climate. http://www.bom.gov.au/climate/influences/images/map-indices.png

Berger, A. (1978). Long-Term Variations of Daily Insolation and Quaternary Climatic Changes. Journal of Atmospheric Sciences, 35(12), 2362–2367. https://doi.org/10.1175/1520-0469(1978)035<2362:LTVODI>2.0.CO;2

Bigg, G. R., & Wadley, M. R. (2001). Millennial-scale variability in the oceans: An ocean modelling view. Journal of Quaternary Science, 16(4), 309–319. https://doi.org/10.1002/jqs.599

Bigg, G. R., Clark, C. D., Greenwood, S. L., Haflidason, H., Hughes, A. L. C., Levine, R. C., Nygård, A., & Sejrup, H. P. (2012). Sensitivity of the North Atlantic circulation to break-up of the marine sectors of the NW European ice sheets during the last Glacial: A synthesis of modelling and palaeoceanography. *Global and Planetary Change*, *98–99*, 153–165. https://doi.org/10.1016/j.gloplacha.2012.09.004

Cane, M., Molnar, P. Closing of the Indonesian seaway as a precursor to east African aridification around 3–4 million years ago. Nature 411, 157–162 (2001). https://doi.org/10.1038/35075500

Chikamoto, M. O., Menviel, L., Abe-Ouchi, A., Ohgaito, R., Timmermann, A., Okazaki, Y., Harada, N., Oka, A., & Mouchet, A. (2012). Variability in North Pacific intermediate and deep water ventilation during Heinrich events in two coupled climate models. *Deep-Sea Research Part II: Topical Studies in Oceanography*, *61–64*, 114–126. https://doi.org/10.1016/j.dsr2.2011.12.002

Copernicus Climate Change Service (C3S) (2017): ERA5: Fifth generation of ECMWF atmospheric reanalyses of the global climate . Copernicus Climate Change Service Climate Data Store (CDS), date of access. https://cds.climate.copernicus.eu/cdsapp#!/home

Cutler, K. B., Edwards, R. L., Taylor, F. W., Cheng, H., Adkins, J., Gallup, C. D., Cutler, P. M., Burr, G. S., & Bloom, A. L. (2003). Rapid sea-level fall and deep-ocean temperature change since the last interglacial period. *Earth and Planetary Science Letters*, *206*(3–4), 253–271. https://doi.org/10.1016/S0012-821X(02)01107-X

De Vleeschouwer, D., Auer, G., Smith, R., Bogus, K., Christensen, B., Groeneveld, J., Petrick, B., Henderiks, J., Castañeda, I. S., O'Brien, E., Ellinghausen, M., Gallagher, S. J., Fulthorpe, C. S., & Pälike, H. (2018). The amplifying effect of Indonesian Throughflow heat transport on Late Pliocene Southern Hemisphere climate cooling. *Earth and Planetary Science Letters*, *500*, 15–27. https://doi.org/10.1016/j.epsl.2018.07.035

Di Nezio, P. N., Timmermann, A., Tierney, J. E., Jin, F. F., Otto-Bliesner, B., Rosenbloom, N., Mapes, B., Neale, R., Ivanovic, R. F., & Montenegro, A. (2016). The climate response of the Indo-Pacific warm pool to glacial sea level. *Paleoceanography*, *31*(6), 866–894. https://doi.org/10.1002/2015PA002890

Ding, X., Bassinot, F., Guichard, F., & Fang, N. Q. (2013). Indonesian Throughflow and monsoon activity records in the Timor Sea since the last glacial maximum. *Marine Micropaleontology*, *101*, 115–126. https://doi.org/10.1016/j.marmicro.2013.02.003

England, M. (1993) 'Representing the global-scale water masses in ocean general circulation models', Journal of physical oceanography, 23(7), pp. 1523–1552. doi:10.1175/1520-0485(1993)0232.0.CO;2.Green, C. L., Bigg, G. R., & Green, J. A. M. (2010). Deep draft icebergs from the Barents Ice Sheet during MIS 6 are consistent with erosional evidence from the Lomonosov Ridge, central Arctic. Geophysical Research Letters, 37(23), 4–7. https://doi.org/10.1029/2010GL045299

Fan, W., Jian, Z., Chu, Z., Dang, H., Wang, Y., Bassinot, F., Han, X., & Bian, Y. (2018). Variability of the Indonesian Throughflow in the Makassar Strait over the Last 30 ka. *Scientific Reports*, *8*(1), 1–8. https://doi.org/10.1038/s41598-018-24055-1

Fanning, Augustus F. and Andrew J. Weaver. "An atmospheric energy-moisture balance model: Climatology, interpentadal climate change, and coupling to an ocean general circulation model." Journal of Geophysical Research 101 (1996): 15111-15128.

Feng, M., Zhang, N., Liu, Q., & Wijffels, S. (2018). The Indonesian throughflow, its variability and centennial change. *Geoscience Letters*, *5*(1). https://doi.org/10.1186/s40562-018-0102-2

Feng, R., & Duan, W. (2018). *The role of initial signals in the tropical Pacific Ocean in*.

Fine, R. A. (1985). Direct evidence using tritium data for throughflow from the Pacific into the Indian Ocean. *Nature*, *315*(6019), 478–480. https://doi.org/10.1038/315478a0

Franzese, A. M., Hemming, S. R., Goldstein, S. L., & Anderson, R. F. (2006). Reduced Agulhas Leakage during the Last Glacial Maximum inferred from an integrated provenance and flux study. *Earth and Planetary Science Letters*, *250*(1–2), 72–88. https://doi.org/10.1016/j.epsl.2006.07.002

Fu, L.-L. (1986). Mass, Heat and Freshwater Fluxes in the South Indian Ocean. *Journal of Physical Oceanography*, *16*(10), 1683–1693. https://doi.org/10.1175/1520-0485(1986)016<1683:MHAFFI>2.0.CO;2

Gill, A. E. Atmosphere-ocean Dynamics. New York ; London: Academic, 1982. Print. International Geophysics Ser. ; 601pp.

Godfrey, J. S. (1989). A Sverdrup model of the depth-integrated flow for the world ocean allowing for island circulations. *Geophysical & Astrophysical Fluid Dynamics*, *45*(1–2), 89–112. https://doi.org/10.1080/03091928908208894

Godfrey, J. S., & Golding, T. J. (1981). The Sverdrup Relation in the Indian Ocean, and the Effect of Pacific-Indian Ocean Throughflow on Indian Ocean Circulation and on the East Australian Current. In *Journal of Physical Oceanography* (Vol. 11, Issue 6, pp. 771–779). https://doi.org/10.1175/1520-0485(1981)011<0771:tsriti>2.0.co;2

Gordon, A. L. (1986). Interocean exchange of thermocline water. *Journal of Geophysical Research: Oceans*, *91*(C4), 5037–5046. https://doi.org/10.1029/JC091iC04p05037

Gordon, A. L., & Fine, R. A. (1996). Pathways of water between the Pacific and Indian oceans in the Indonesian seas. *Nature*, *379*(6561), 146–149. https://doi.org/10.1038/379146a0

Gordon, A. L., Giulivi, C. F., & Ilahude, A. G. (2003). Deep topographic barriers within the Indonesian seas. *Deep-Sea Research Part II: Topical Studies in Oceanography*, *50*(12–13), 2205–2228. https://doi.org/10.1016/S0967-0645(03)00053-5

Gordon, A. L., Susanto, R. D., Ffield, A., Huber, B. A., Pranowo, W., and Wirasantosa, S. (2008), Makassar Strait throughflow, 2004 to 2006, Geophys. Res. Lett., 35, L24605, doi:10.1029/2008GL036372.

Gordon, A. L., Huber, B. A., Metzger, E. J., Susanto, R. D., Hurlburt, H. E., & Adi, T. R. (2012). South China Sea throughflow impact on the Indonesian throughflow. *Geophysical Research Letters*, *39*(11), 1–7. https://doi.org/10.1029/2012GL052021

Gordon, A. L., Susanto, R. D., & Ffield, A. (1999). Throughflow within Makassar Strait. *Geophysical Research Letters*, *26*(21), 3325–3328. https://doi.org/https://doi.org/10.1029/1999GL002340

Green, C. L., Bigg, G. R., & Green, J. A. M. (2010). Deep draft icebergs from the Barents Ice Sheet during MIS 6 are consistent with erosional evidence from the Lomonosov Ridge, central Arctic. *Geophysical Research Letters*, *37*(23), 4–7. https://doi.org/10.1029/2010GL045299

Griffies, S. M., Gnanadesikan, A., Pacanowski, R. C., Larichev, V. D., Dukowicz, J. K., & Smith, R. D. (1998). Isoneutral diffusion in a z-coordinate ocean model. *Journal of Physical Oceanography*, *28*(5), 805–830. https://doi.org/10.1175/1520-0485(1998)028<0805:IDIAZC>2.0.CO;2

Hamada, J. I., Yamanaka, M. D., Matsumoto, J., Fukao, S., Winarso, P. A., & Sribimawati, T. (2002). Spatial and temporal variations of the rainy season over Indonesia and their link to ENSO. *Journal of the Meteorological Society of Japan*, *80*(2), 285–310. https://doi.org/10.2151/jmsj.80.285

He, S., & Wang, H. (2013). Oscillating relationship between the East Asian Winter Monsoon and ENSO. *Journal of Climate*, *26*(24), 9819–9838. https://doi.org/10.1175/JCLI-D-13-00174.1

Hendrizan, M., Kuhnt, W., & Holbourn, A. (2017). Variability of Indonesian Throughflow and Borneo Runoff During the Last 14 kyr. *Paleoceanography*, *32*(10), 1054–1069. https://doi.org/10.1002/2016PA003030

Hirst, A. C., & Godfrey, J. S. (1993). The Response to a Sudden Change in Indonesian Throughflow in a Global Ocean GCM. In *Journal of Physical Oceanography* (Vol. 24, Issue 9, pp. 1895–1910). https://doi.org/10.1175/1520-0485(1994)024<1895:trtasc>2.0.co;2

Horhoruw, S. M., Atmadipoera, A. S., Nanlohy, P., & Nurjaya, I. W. (2017). Anomaly of surface circulation and Ekman transport in Banda Sea during "Normal" and ENSO episode (2008-2011). *IOP Conference Series: Earth and Environmental Science*, *54*(1), 12041. https://doi.org/10.1088/1755-1315/54/1/012041

Hughes, T. M. C., Weaver, A. J., & Godfrey, J. S. (1992). Thermohaline forcing of the Indian Ocean by the Pacific Ocean. *Deep Sea Research Part A, Oceanographic Research Papers*, *39*(6), 965–995. https://doi.org/10.1016/0198-0149(92)90035-R

Jin, F.-F. (1997). An Equatorial Ocean Recharge Paradigm for ENSO. Part II: A Stripped-Down Coupled Model. *Journal of the Atmospheric Sciences*, *54*(7), 830–847. https://doi.org/10.1175/1520-0469(1997)054<0830:AEORPF>2.0.CO;2

Kahana, R., Bigg, G. R., & Wadley, M. R. (2004). Global ocean circulation modes derived from a multiple box model. *Journal of Physical Oceanography*, *34*(8), 1811–1823. https://doi.org/10.1175/1520-0485(2004)034<1811:GOCMDF>2.0.CO;2

Kalnay, E., Kanamitsu, M., Kistler, R., Collins, W., Deaven, D., Gandin, L., Iredell, M., Saha, S., White, G., Woollen, J., Zhu, Y., Chelliah, M., Ebisuzaki, W., Higgins, W., Janowiak, J., Mo, K. C., Ropelewski, C., Wang, J., Leetmaa, A., … Joseph, D. (1996). The NCEP/NCAR 40-year reanalysis project. In *Bulletin of the American Meteorological Society* (Vol. 77, Issue 3, pp. 437–471). https://doi.org/10.1175/1520-0477(1996)077<0437:TNYRP>2.0.CO;2

Kashino, Y., Watanabe, H., Herunadi, B., Aoyama, M., & Hartoyo, D. (1999). Current variability at the Pacific entrance of the Indonesian Throughflow. *Journal of Geophysical Research: Oceans*, *104*(C5), 11021–11035. https://doi.org/10.1029/1999JC900033

Kim, S. J., Flato, G. M., Boer, G. J., & McFarlane, N. A. (2002). A coupled climate model simulation of the Last Glacial Maximum, part 1: Transient multi-decadal response. *Climate Dynamics*, *19*(5–6), 515–537. https://doi.org/10.1007/s00382-002-0243-y

Knorr, G., & Lohmann, G. (2003). Southern ocean origin for the resumption of Atlantic thermohaline circulation during deglaciation. *Nature*, *424*(6948), 532–536. https://doi.org/10.1038/nature01855

Koch-Larrouy, A., Madec, G., Iudicone, D., Atmadipoera, A., & Molcard, R. (2008). Physical processes contributing to the water mass transformation of the Indonesian throughflow. *Ocean Dynamics*, *58*(3–4), 275–288. https://doi.org/10.1007/s10236-008-0154-5

Krebs, U., Park, W., & Schneider, B. (2011). Pliocene aridification of Australia caused by tectonically induced weakening of the Indonesian throughflow. *Palaeogeography, Palaeoclimatology, Palaeoecology*, *309*(1–2), 111–117. https://doi.org/10.1016/j.palaeo.2011.06.002

Kuhnt, W., Holbourn, A., Hall, R., Zuvela, M., & Käse, R. (2004). Neogene history of the indonesian throughflow. *Geophysical Monograph Series*, *149*, 299–320. https://doi.org/10.1029/149GM16

Levine, R. C., & Bigg, G. R. (2008). Sensitivity of the glacial ocean to Heinrich events from different iceberg sources, as modeled by a coupled atmosphere-iceberg-ocean model. *Paleoceanography*, *23*(4), 1–16. https://doi.org/10.1029/2008PA001613

Liang, L., Xue, H., & Shu, Y. (2019). The Indonesian Throughflow and the Circulation in the Banda Sea: A Modeling Study. *Journal of Geophysical Research: Oceans*, *124*(5), 3089–3106. https://doi.org/10.1029/2018JC014926

Linsley, B. K., Wu, H. C., Rixen, T., Charles, C. D., Gordon, A. L., & Moore, M. D. (2017). SPCZ zonal events and downstream influence on surface ocean conditions in the Indonesian Throughflow region. *Geophysical Research Letters*, *44*(1), 293–303. https://doi.org/10.1002/2016GL070985

Liu, Z., Shin, S.-I., Otto-Bliesner, B., Kutzbach, J. E., Brady, E. C., & Lee, D. (2002). Tropical cooling at the last glacial maximum and extratropical ocean ventilation 1 . *Geophysical Research Letters*, *29*(10), 48-1-48–4. https://doi.org/10.1029/2001gl013938

Marotzke, J. (2000). Abrupt climate change and thermohaline circulation: Mechanisms and predictability. *Proceedings of the National Academy of Sciences of the United States of America*, *97*(4), 1347–1350. https://doi.org/10.1073/pnas.97.4.1347

Masumoto, Y., & Yamagata, T. (1993). Simulated seasonal circulation in the Indonesian seas. *Journal of Geophysical Research*, *98*(C7), 12501. https://doi.org/10.1029/93jc01025

McCarron, A. P., Bigg, G. R., Brooks, H., Leng, M. J., Marshall, J. D., Ponomareva, V., Portnyagin, M., Reimer, P. J., & Rogerson, M. (2021). Northwest Pacific ice-rafted debris at 38°N reveals episodic ice-sheet change in late Quaternary Northeast Siberia. *Earth and Planetary Science Letters*, *553*, 116650. https://doi.org/10.1016/j.epsl.2020.116650

Menviel, L., Timmermann, A., Timm, O. E., & Mouchet, A. (2011). Deconstructing the Last Glacial termination: The role of millennial and orbital-scale forcings. *Quaternary Science Reviews*, *30*(9–10), 1155–1172. https://doi.org/10.1016/j.quascirev.2011.02.005

Meyers, G. (1996). Variation of Indonesian throughflow and the El Niño-Southern Oscillation. *J. Geophys. Res.*, *101*(C5), 12255–12264.

Meyers, G., Bailey, R. J., & Worby, A. P. (1995). Geostrophic transport of Indonesian throughflow. *Deep-Sea Research Part I*, *42*(7), 1163–1174. https://doi.org/10.1016/0967-0637(95)00037-7

Miyama, T., Awaji, T., Akitomo, K., & Imasato, N. (1995). Study of seasonal transport variations in the indonesian seas. *Journal of Geophysical Research: Oceans*, *100*(C10), 20,517-20,541. https://doi.org/10.1029/95JC01667

Molcard, R., Fieux, M., Swallow, J. C., Ilahude, A. G., & Banjarnahor, J. (1994). Low frequency variability of the currents in Indonesian channels (Savu-Roti and Roti-Ashmore Reef). *Deep-Sea Research Part I*, *41*(11–12), 1643–1661. https://doi.org/10.1016/0967-0637(94)90066-3

Molcard, R., Fieux, M., & Syamsudin, F. (2001). The throughflow within Ombai Strait. *Deep-Sea Research Part I: Oceanographic Research Papers*, *48*(5), 1237–1253. https://doi.org/10.1016/S0967-0637(00)00084-4

Müller, A., & Opdyke, B. N. (2000). Glacial-interglacial changes in nutrient utilization and paleoproductivity in the Indonesian Throughflow sensitive Timor Trough, easternmost Indian Ocean. *Paleoceanography*, *15*(1), 85–94. https://doi.org/10.1029/1999PA900046

Muller, J., McManus, J. F., Oppo, D. W., & Francois, R. (2012). Strengthening of the Northeast Monsoon over the Flores Sea, Indonesia, at the time of Heinrich event 1. *Geology*, *40*(7), 635–638. https://doi.org/10.1130/G32878.1

Murray, S. P., & Arief, D. (1988). Throughflow into the Indian Ocean through the Lombok Strait, January 1985-January 1986. *Nature*, *333*(6172), 444–447. https://doi.org/10.1038/333444a0

Murray, S. P., & Arief, D. (1988). Throughflow into the Indian Ocean through the Lombok Strait, January 1985-January 1986. *Nature*, *333*(6172), 444–447. https://doi.org/10.1038/333444a0

Okazaki, Y., Timmermann, A., Menviel, L., Harada, N., Abe-Ouchi, A., Chikamoto, M. O., Mouchet, A., & Asahi, H. (2010). Deepwater Formation in the North Pacific During the Last Glacial Termination. *Science*, *329*(5988), 200–204. https://doi.org/10.1126/science.1190612

Oppo, D. W., Curry, W. B., & McManus, J. F. (2015). What do benthic δ13C and δ18O data tell us about Atlantic circulation during Heinrich Stadial 1? *Paleoceanography*, *30*(4), 353–368. https://doi.org/10.1002/2014PA002667

Osman, M. B., Tierney, J. E., Zhu, J., Tardif, R., Hakim, G. J., King, J., & Poulsen, C. J. (2021). *Globally resolved surface temperatures since the Last Glacial Maximum*. *599*(March), 2–53. https://doi.org/10.31223/X5S31Z

Paul, A., & Schäfer-Neth, C. (2003). Modeling the water masses of the Atlantic Ocean at the last glacial maximum. *Paleoceanography*, *18*(3). https://doi.org/10.1029/2002pa000783

Petukhova, a, Kumacheva, E., Solomon, M. J., Dittmer, J. J., Alivisatos, a P., Mclellan, J. M., Xia, Y., Kotov, N. a, Giersig, M., Mermet, A., Albouy, P. a, Duval, E., Pileni, M. P., Baudry, J., Pine, D., Chaikin, P., Bibette, J., Ohtsu, M., Yatsui, T., … Tang, Z. (2010). Deepwater Formation in the North Pacific During the last Glacial Terminatin. *Science*, *329*(July), 200–204.

Peltier, W. R., & Fairbanks, R. G. (2006). Global glacial ice volume and Last Glacial Maximum duration from an extended Barbados sea level record. *Quaternary Science Reviews*, *25*(23–24), 3322–3337. https://doi.org/10.1016/j.quascirev.2006.04.010

Peltier, W. R. (1994). Ice age paleotopography. *Science*, *265*(5169), 195–201. https://doi.org/10.1126/science.265.5169.195

Piola, A. R., & Gordon, A. L. (1984). Pacific and Indian Ocean Upper-Layer Salinity Budget. *Journal of Physical Oceanography*, *14*(4), 747–753. https://doi.org/10.1175/1520-0485(1984)014<0747:PAIOUL>2.0.CO;2

Potemra, J. T. (1999). Seasonal variations of upper ocean transport from the Pacific to the Indian Ocean via Indonesian Straits. *Journal of Physical Oceanography*, *29*(11), 2930–2944. https://doi.org/10.1175/1520-0485(1999)029<2930:SVOUOT>2.0.CO;2

Qu, T., Du, Y., Meyers, G., Ishida, A., & Wang, D. (2005). Connecting the tropical Pacific with Indian Ocean through South China Sea. *Geophysical Research Letters*, *32*(24), 1–4. https://doi.org/10.1029/2005GL024698

Rea, B. R., Newton, A. M. W., Lamb, R. M., Harding, R., Bigg, G. R., Rose, P., Spagnolo, M., Huuse, M., Cater, J. M. L., Archer, S., Buckley, F., Halliyeva, M., Huuse, J., Cornwell, D. G., Brocklehurst, S. H., & Howell, J. A. (2018). Extensive marine-terminating ice sheets in Europe from 2.5 million years ago. *Science Advances*, *4*(6). https://doi.org/10.1126/sciadv.aar8327

Rippert, N., Baumann, K. H., & Pätzold, J. (2015). Thermocline fluctuations in the western tropical Indian Ocean during the past 35 ka. *Journal of Quaternary Science*, *30*(3), 201–210. https://doi.org/10.1002/jqs.2767

Risebrobakken, B., Dokken, T., Otterå, O. H., Jansen, E., Gao, Y., & Drange, H. (2007). Inception of the Northern European ice sheet due to contrasting ocean and insolation forcing. *Quaternary Research*, *67*(1), 128–135. https://doi.org/10.1016/j.yqres.2006.07.007

Robinson, A., & Goelzer, H. (2014). The importance of insolation changes for paleo ice sheet modeling. *Cryosphere*, *8*(4), 1419–1428. https://doi.org/10.5194/tc-8-1419-2014

Santoso, A., England, W. C., & Phipps, S. J. (2011). The role of the Indonesian throughflow on ENSO dynamics in a coupled climate model. *Journal of Climate*, *24*(3), 585–601. https://doi.org/10.1175/2010JCLI3745.1

Susanto, R. D., and Song, Y. T. (2015), Indonesian throughflow proxy from satellite altimeters and gravimeters, J. Geophys. Res. Oceans, 120, 2844– 2855, doi:10.1002/2014JC010382

Sarnthein, M., Grunert, P., Khélifi, N., Frank, M., & Nürnberg, D. (2018). Interhemispheric teleconnections: Late Pliocene change in Mediterranean outflow water linked to changes in Indonesian Through-Flow and Atlantic Meridional Overturning Circulation, a review and update. *International Journal of Earth Sciences*, *107*(2), 505–515. https://doi.org/10.1007/s00531-017-1505-6

Schröder, J. F., Holbourn, A., Kuhnt, W., & Küssner, K. (2016). Variations in sea surface hydrology in the southern Makassar Strait over the past 26 kyr. *Quaternary Science Reviews*, *154*, 143–156. https://doi.org/10.1016/j.quascirev.2016.10.018

Shin, S. I., Liu, Z., Otto-Bliesner, B., Brady, E. C., Kutzbach, J. E., & Harrison, S. P. (2003). A simulation of the last glacial maximum climate using the NCAR-CCSM. *Climate Dynamics*, *20*(2–3), 127–151. https://doi.org/10.1007/s00382-002-0260-x

Song, Q., Vecchi, G. A., & Rosati, A. J. (2007). The role of the Indonesian throughflow in the Indo-Pacific climate variability in the GFDL coupled climate model. *Journal of Climate*, *20*(11), 2434–2451. https://doi.org/10.1175/JCLI4133.1

Sprintall, J., Gordon, A. L., Koch-Larrouy, A., Lee, T., Potemra, J. T., Pujiana, K., & Wijffels, S. E. (2014). The Indonesian seas and their role in the coupled ocean-climate system. *Nature Geoscience*, *7*(7), 487–492. https://doi.org/10.1038/ngeo2188

Sprintall, J., Wijffels, S. E., Molcard, R., & Jaya, I. (2009). Direct estimates of the indonesian throughflow entering the indian ocean: 2004-2006. *Journal of Geophysical Research: Oceans*, *114*(7), 1–19. https://doi.org/10.1029/2008JC005257

Starr, A., Hall, I. R., Barker, S., Rackow, T., Zhang, X., Hemming, S. R., van der Lubbe, H. J. L., Knorr, G., Berke, M. A., Bigg, G. R., Cartagena-Sierra, A., Jiménez-Espejo, F. J., Gong, X., Gruetzner, J., Lathika, N., LeVay, L. J., Robinson, R. S., Ziegler, M., Brentegani, L., … Zhang, H. (2021). Antarctic icebergs reorganize ocean circulation during Pleistocene glacials. *Nature*, *589*(7841), 236–241. https://doi.org/10.1038/s41586-020-03094-7

Toole, J. M., & Warren, B. A. (1993). A hydrographic section across the subtropical South Indian Ocean. *Deep-Sea Research Part I*, *40*(10), 1973–2019. https://doi.org/10.1016/0967-0637(93)90042-2

Valsala, V., Maksyutov, S., & Murtugudde, R. (2010). Possible interannual to interdecadal variabilities of the Indonesian throughflow water pathways in the Indian Ocean. *Journal of Geophysical Research: Oceans*, *115*(10), 1921–1940. https://doi.org/10.1029/2009JC005735

Van Sebille, E., Sprintall, J., Schwarzkopf, F. U., Sen Gupta, A., Santoso, A., England, M. H., Biastoch, A., & Böning, C. W. (2014). Pacific-to-Indian Ocean connectivity: Tasman leakage, Indonesian Throughflow, and the role of ENSO. *Journal of*

Geophysical Research: Oceans, *119*(2), 1365–1382. https://doi.org/10.1002/2013JC009525

Vranes, K., & Gordon, A. L. (2005). Comparison of Indonesian Throughflow transport observations, Makassar Strait to eastern Indian Ocean. *Geophysical Research Letters*, *32*(10), 1–5. https://doi.org/10.1029/2004GL022158

Wadley, M. R., & Bigg, G. R. (2002). Impact of flow through the Canadian Archipelago and Bering Strait on the North Atlantic and Arctic circulation: An ocean modelling study. *Quarterly Journal of the Royal Meteorological Society*, *128*(585 PART A), 2187–2203. https://doi.org/10.1256/qj.00.35

Wang, L., & Wu, R. (2012). In-phase transition from the winter monsoon to the summer monsoon over East Asia: Role of the Indian Ocean. *Journal of Geophysical Research Atmospheres*, *117*(11). https://doi.org/10.1029/2012JD017509

Webster, P. J., Magaña, V. O., Palmer, T. N., Shukla, J., Tomas, R. A., Yanai, M., & Yasunari, T. (1998). Monsoons: Processes, predictability, and the prospects for prediction. *Journal of Geophysical Research: Oceans*, *103*(C7), 14451–14510. https://doi.org/10.1029/97JC02719

Webster, P. J., & Yang, S. (1992). Monsoon and Enso: Selectively Interactive Systems. In *Quarterly Journal of the Royal Meteorological Society* (Vol. 118, Issue 507). https://doi.org/10.1002/qj.49711850705

Wu, S., Lembke-Jene, L., Lamy, F., Arz, H. W., Nowaczyk, N., Xiao, W., Zhang, X., Hass, H. C., Titschack, J., Zheng, X., Liu, J., Dumm, L., Diekmann, B., Nürnberg, D., Tiedemann, R., & Kuhn, G. (2021). Orbital- and millennial-scale Antarctic Circumpolar Current variability in Drake Passage over the past 140,000 years. *Nature Communications*, *12*(1), 1–9. https://doi.org/10.1038/s41467-021-24264-9

Wunsch, C., Hu, D., & Grant, B. (1983). Mass, Heat, Salt and Nutrient Fluxes in the South Pacific Ocean. *Journal of Physical Oceanography*, *13*(5), 725–753. https://doi.org/10.1175/1520-0485(1983)013<0725:mhsanf>2.0.co;2

Wyrtki K (1961) Physical oceanography of the southeast Asian waters. University of California, NAGA Rept., No. 2, 195 pp

Xu, J. (2014). Change of Indonesian Throughflow outflow in response to East Asian monsoon and ENSO activities since the Last Glacial. *Science China Earth Sciences*, *57*(4), 791–801. https://doi.org/10.1007/s11430-014-4845-0

Xu, Y., Wang, L., Yin, X., Ye, X., Li, D., Liu, S., Shi, X., Troa, R. A., Zuraida, R., Triarso, E., & Hendrizan, M. (2017). The influence of the Sunda Strait opening on paleoenvironmental changes in the eastern Indian Ocean. *Journal of Asian Earth Sciences*, *146*(June), 402–411. https://doi.org/10.1016/j.jseaes.2017.06.014

Yin, Q. (2013). Insolation-induced mid-Brunhes transition in Southern Ocean ventilation and deep-ocean temperature. *Nature*, *494*(7436), 222–225. https://doi.org/10.1038/nature11790

Yokoyama, Y., Lambeck, K., De Deckker, P., Johnston, P., & Fifield, L. K. (2000). Timing of the Last Glacial Maximum from observed sea-level minima. *Nature*, *406*(6797), 713–716. https://doi.org/10.1038/35021035

Yu, Y., Zhang, X., & Guo, Y. (2004). Global coupled ocean-atmosphere general circulation models in LASG/IAP. *Advances in Atmospheric Sciences*, *21*(3), 444–455. https://doi.org/10.1007/bf02915571

Zhang, P., Xu, J., Schröder, J. F., Holbourn, A., Kuhnt, W., Kochhann, K. G. D., Ke, F., Wang, Z., & Wu, H. (2018). Variability of the Indonesian Throughflow thermal profile over the last 25-kyr: A perspective from the southern Makassar Strait. *Global and Planetary Change*, *169*(August), 214–223. https://doi.org/10.1016/j.gloplacha.2018.08.003

Zhang, X., & Prange, M. (2020). Stability of the Atlantic overturning circulation under intermediate (MIS3) and full glacial (LGM) conditions and its relationship with Dansgaard-Oeschger climate variability. *Quaternary Science Reviews*, *242*, 106443. https://doi.org/10.1016/j.quascirev.2020.106443

Zhang, Y., Fan, G., Hua, W., Zhang, Y., Wang, B., & Lai, X. (2017). Differences in atmospheric heat source between the Tibetan Plateau–South Asia region and the southern Indian Ocean and their impacts on the Indian summer monsoon outbreak. *Journal of Meteorological Research*, *31*(3), 540–554. https://doi.org/10.1007/s13351-017-6042-5

Appendices

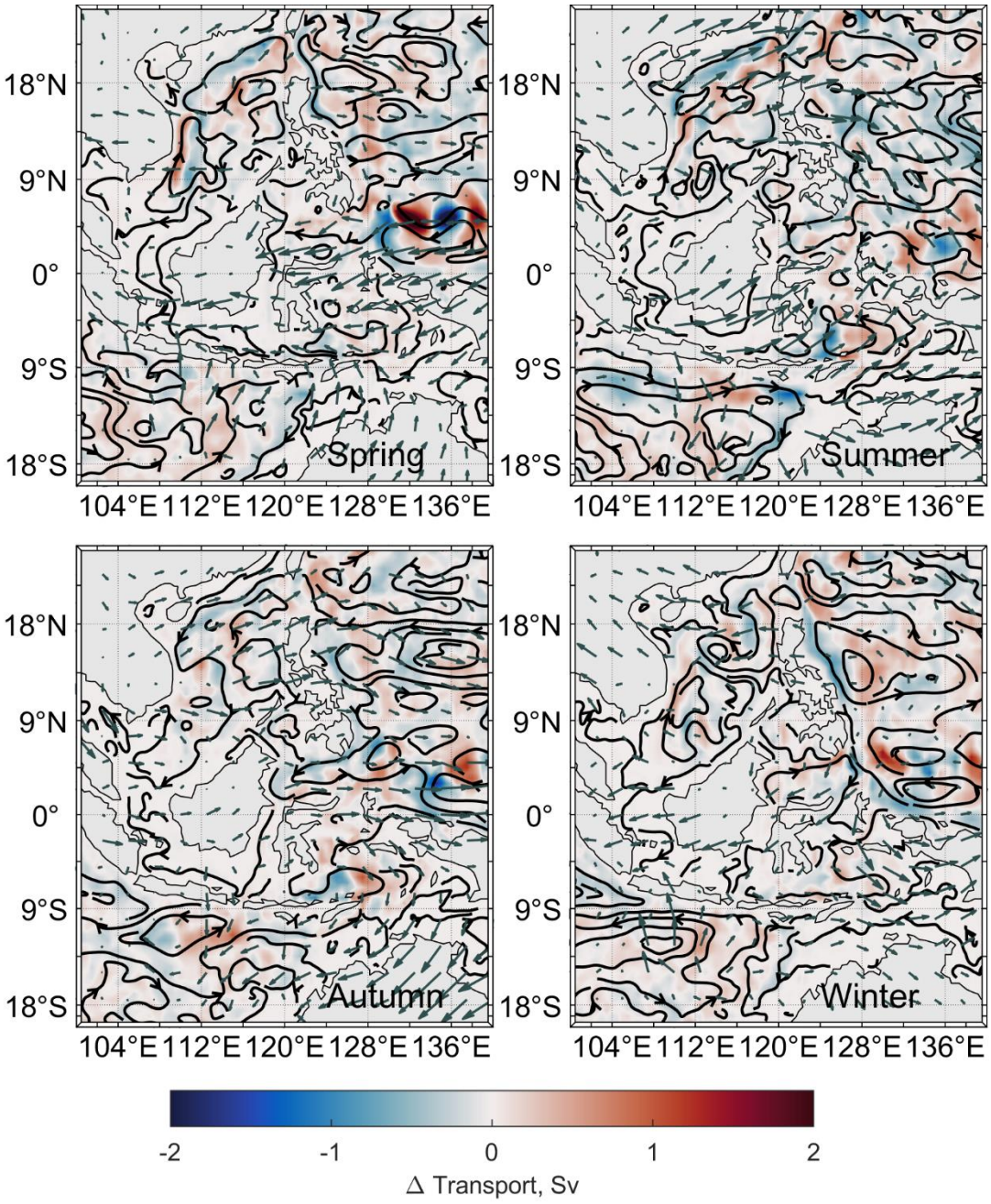

Figure S1 The seasonal distribution of the transport anomaly during 1980 to 1992 over depth layer 1, unit: Sv. The red quiver indicates the perturbed wind field, unit: m s^{-1}.

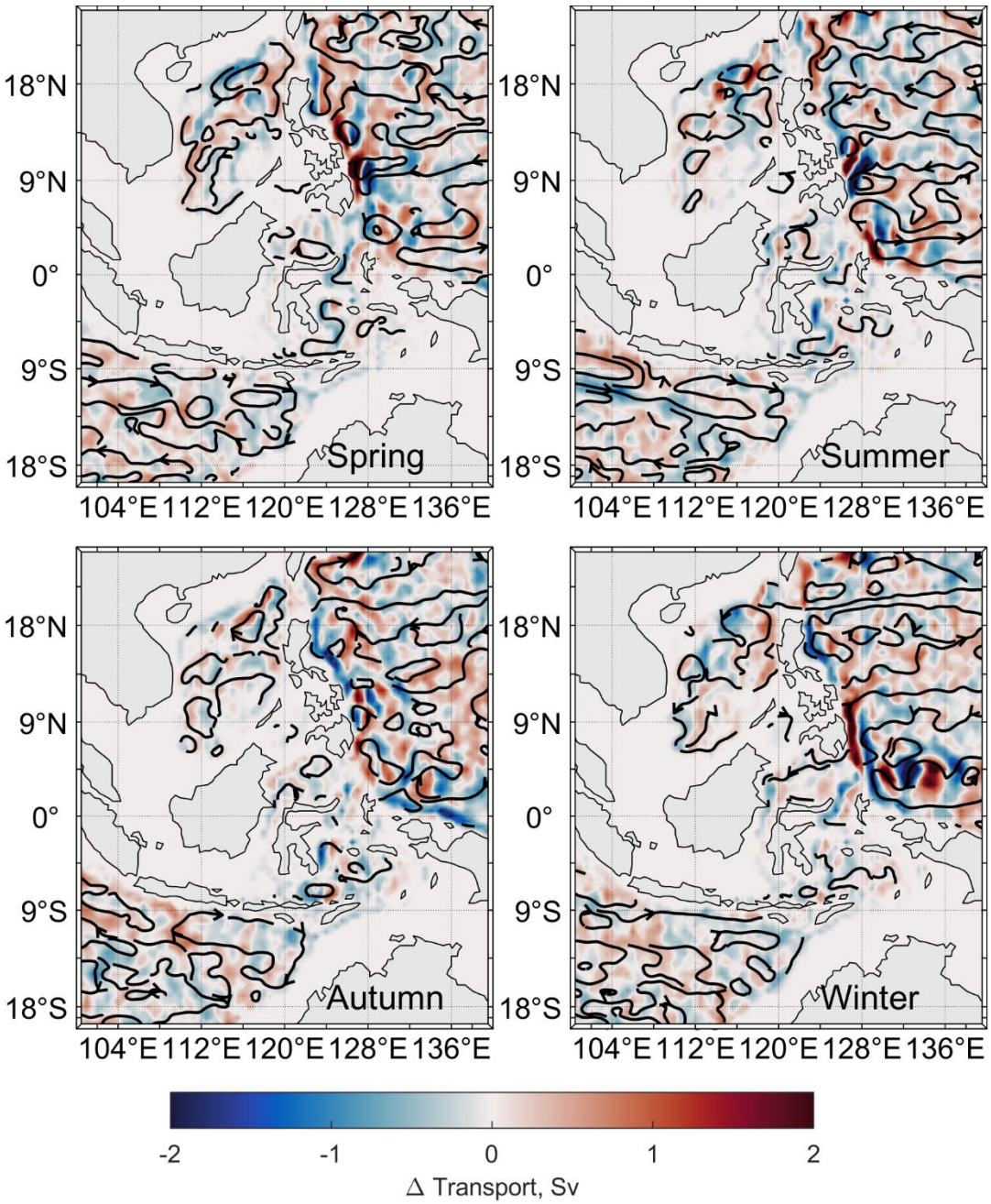

Figure S2 The seasonal distribution of the transport anomaly during 1980 to 1992 over depth layer 2, unit: Sv.

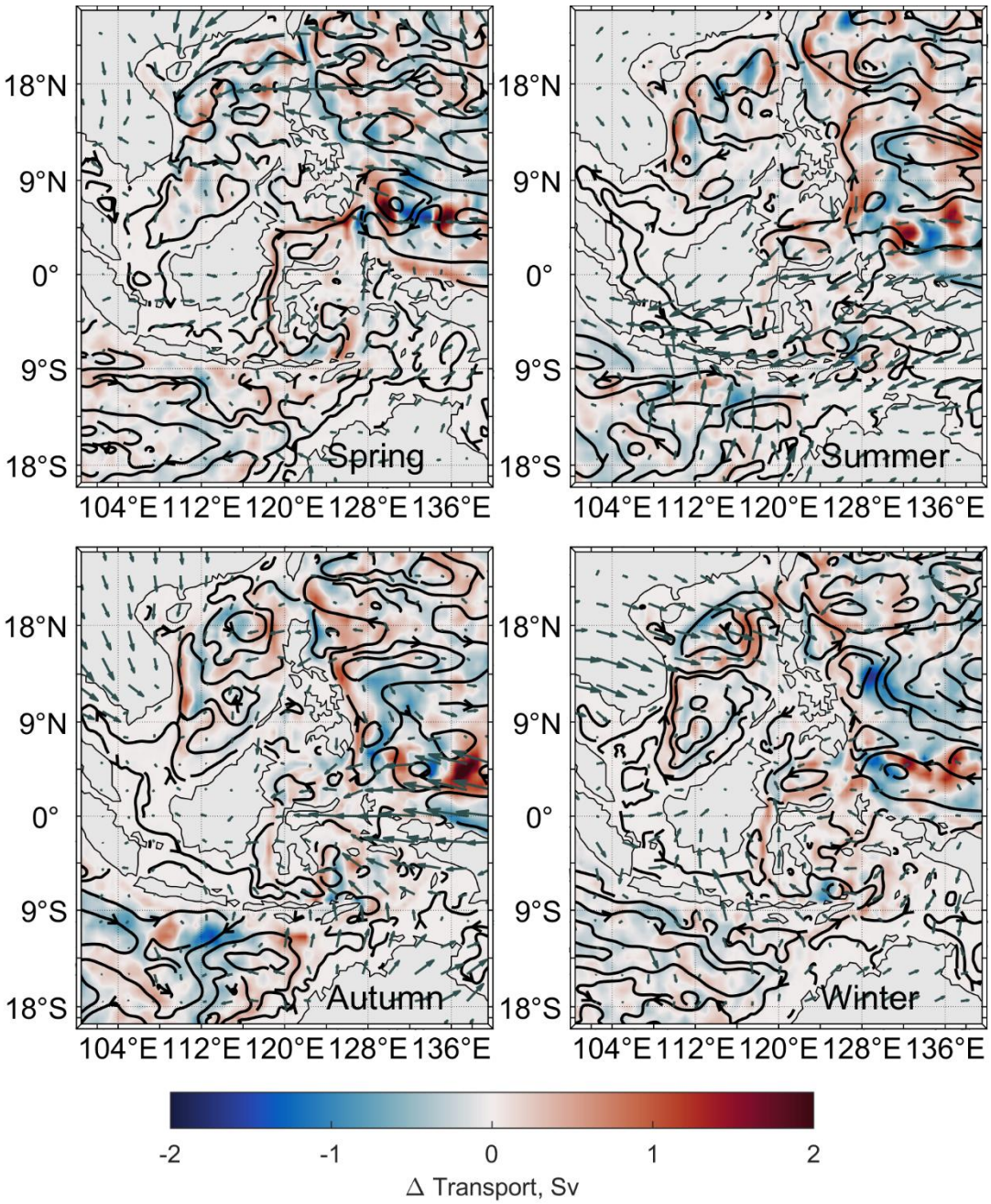

Figure S3 The seasonal distribution of the transport anomaly during 1993 to 2000 over depth layer 1, unit: Sv. The grey quiver indicates the perturbed wind field, unit: m s^{-1}.

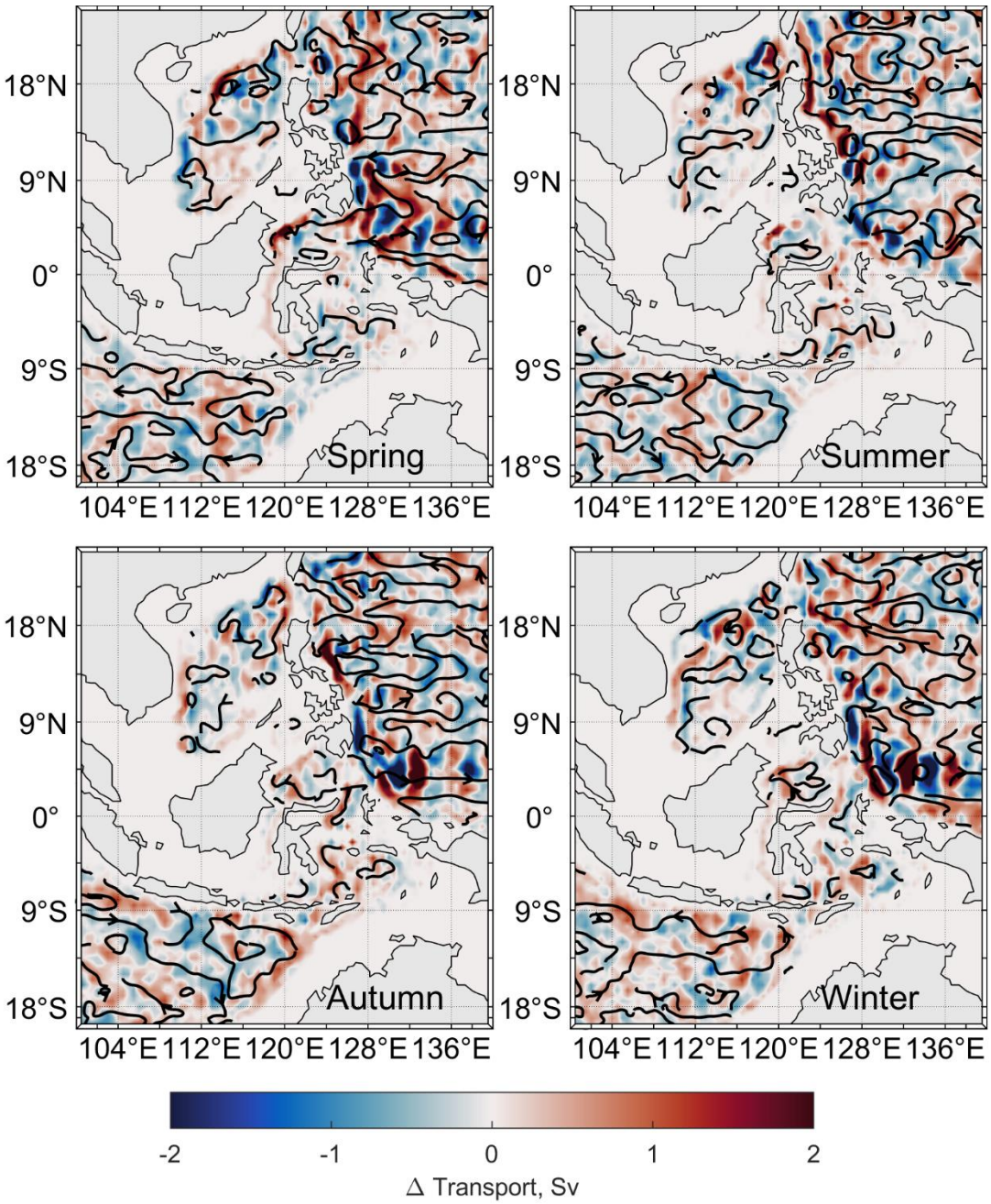

Figure S4 The seasonal distribution of the transport anomaly during 1993 to 2000 over depth layer 2, unit: Sv.

.

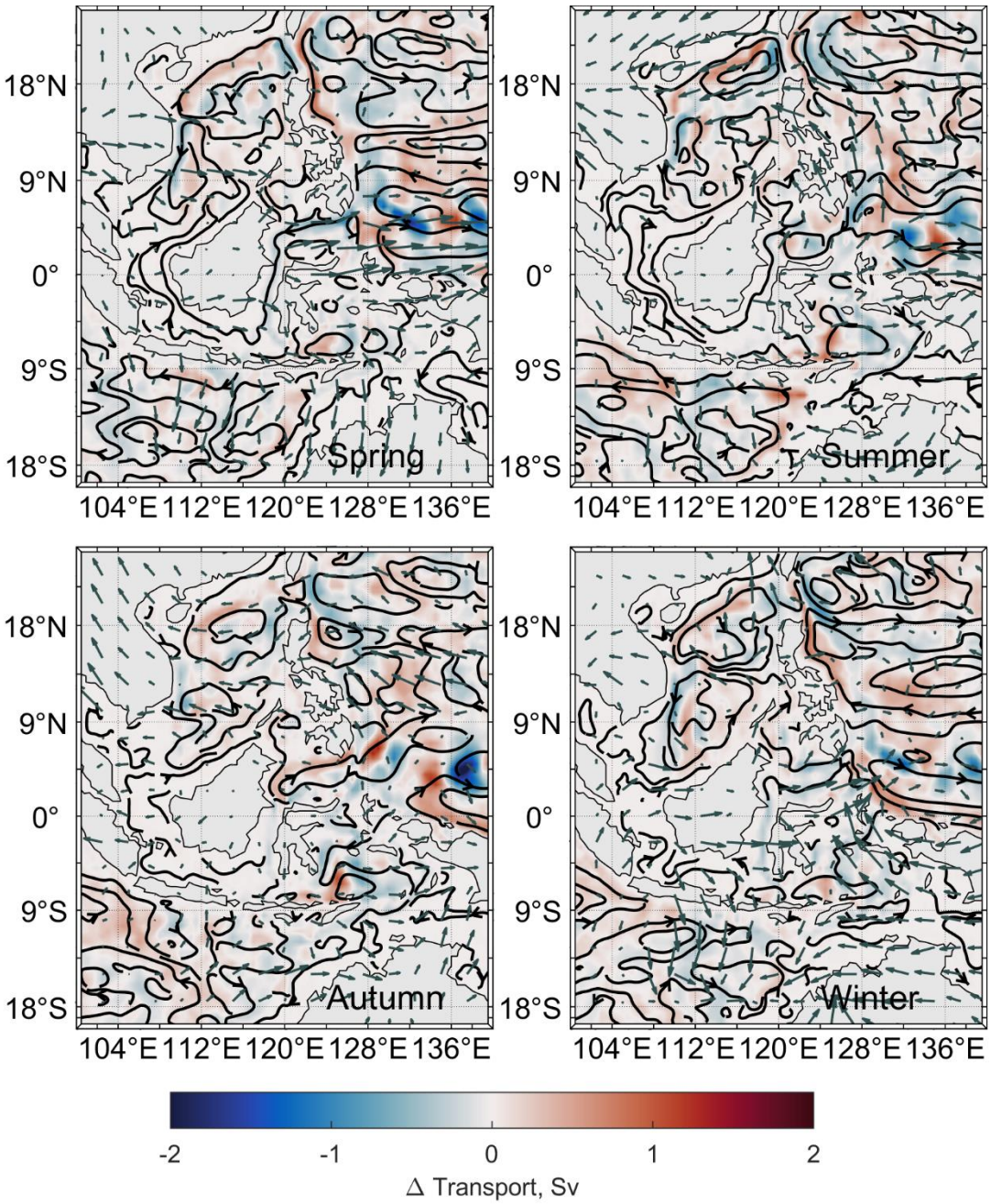

Figure S5 The seasonal distribution of the transport anomaly during 2001 to 2016 over depth layer 1, unit: Sv. The grey quiver indicates the perturbed wind field, unit: m s^{-1}.

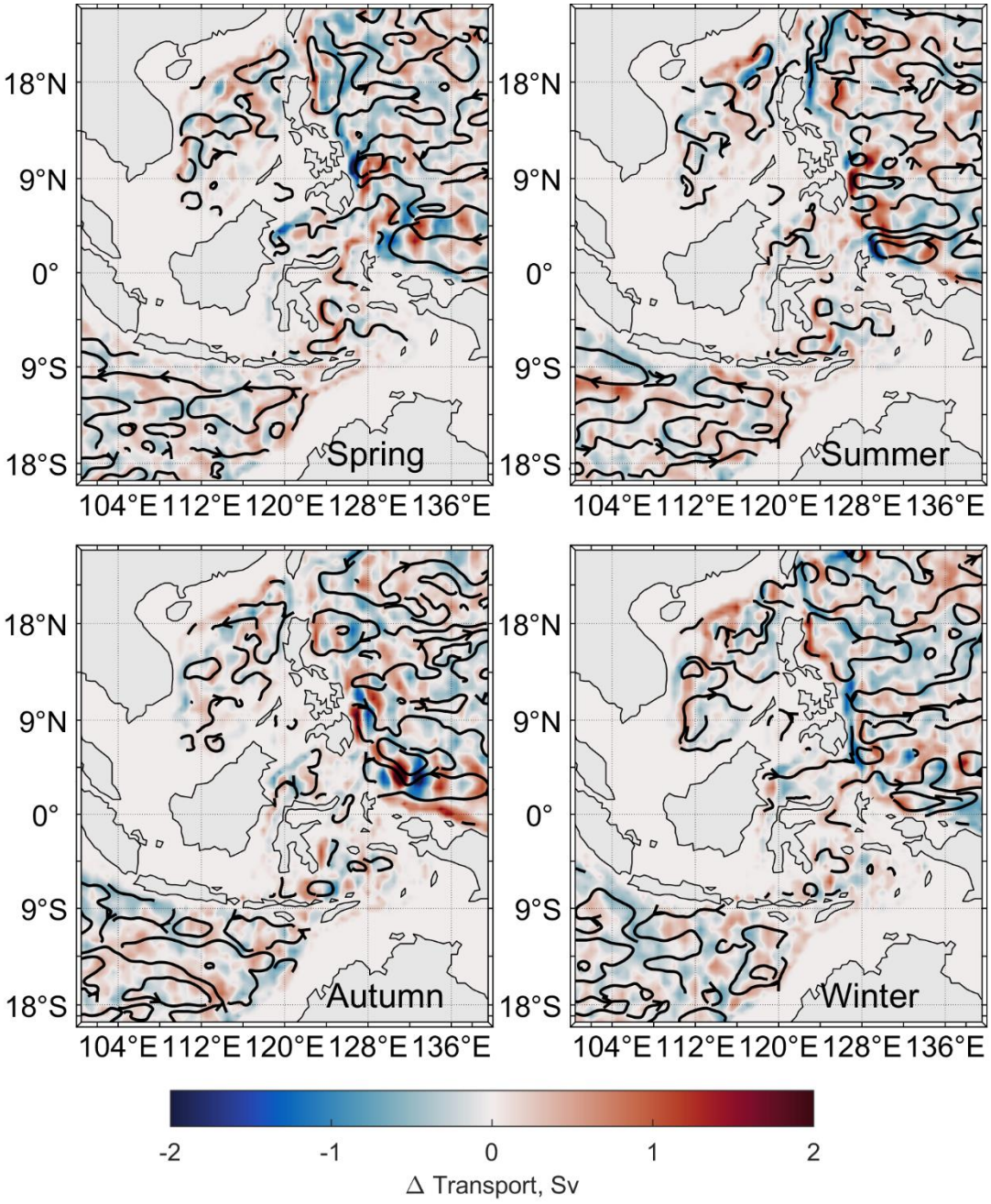

Figure S6 The seasonal distribution of the transport anomaly during 2001 to 2016 over depth layer 2, unit: Sv.

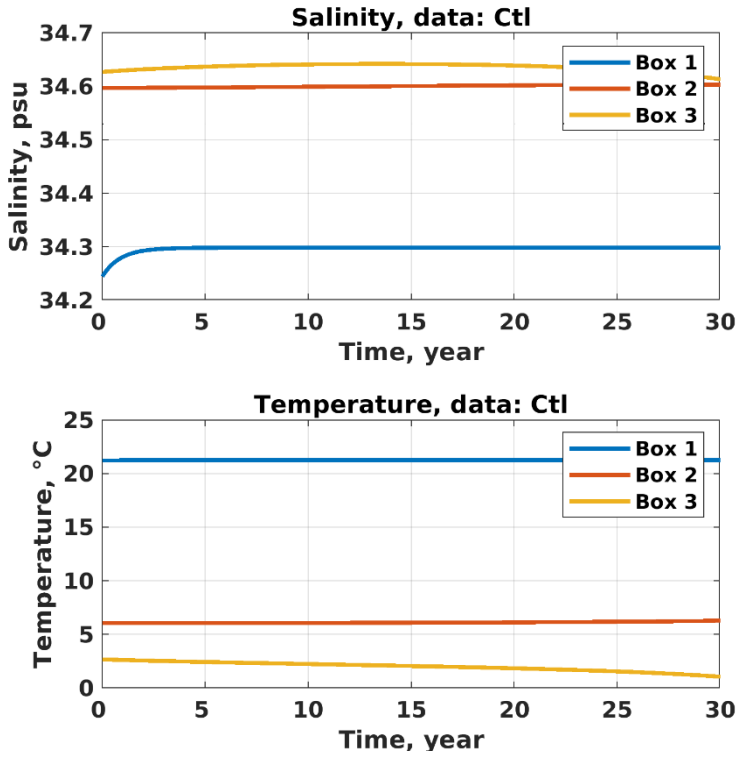

Figure S7 The modelled temperature and salinity of the Ctl run by k_t.

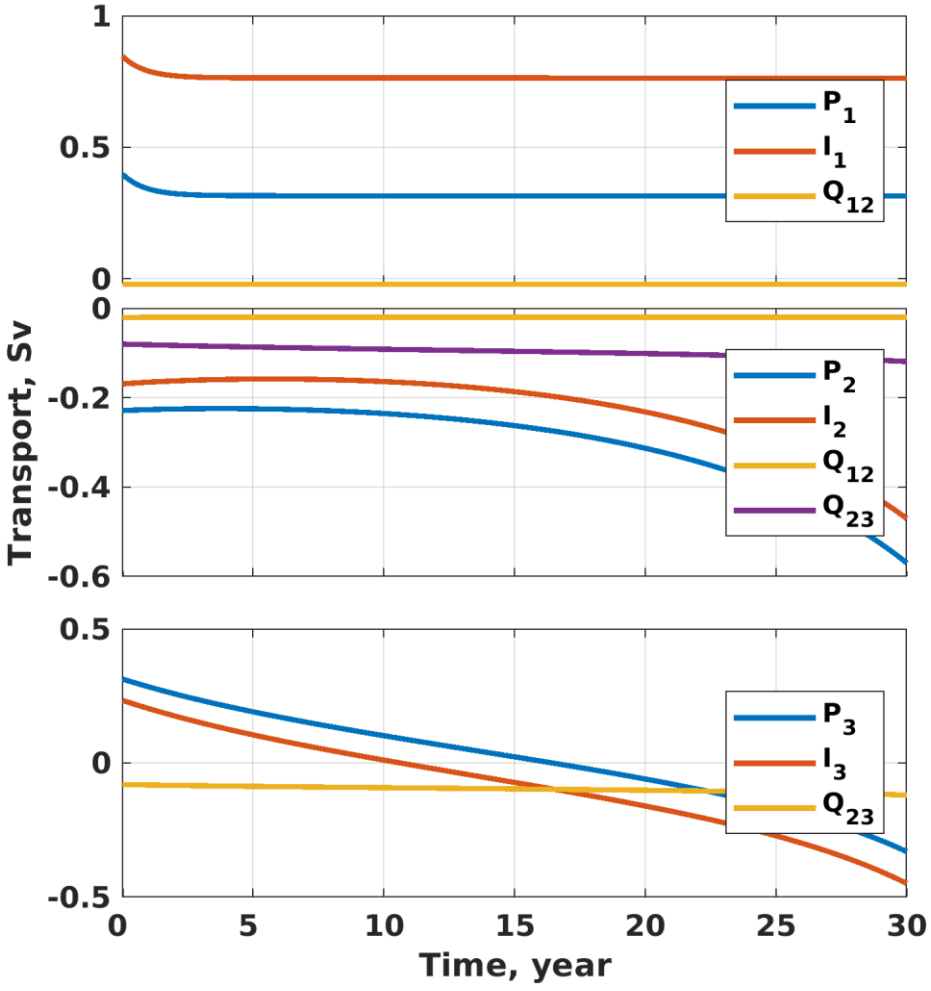

Figure S8 The modelled transport of the CTL run by k_t. The sign of the transport value representatives the same direction in this chapter.